Modeling the Dissolution of Immiscible Contaminants in Groundwater for Decision Support

Andres Eduardo Prieto Estrada

Dissertation submitted to the faculty of the Virginia Polytechnic Institute and State University in partial fulfillment of the requirements for the degree of

Doctor of Philosophy
In
Civil Engineering

Mark A. Widdowson, Chair
Lloyd D. Stewart
Thomas J. Burbey
Stanley B. Grant

May 02, 2023
Blacksburg, VA

Keywords: non-aqueous phase liquids, mass transfer processes, upscaled and numerical modeling, parameter estimation, uncertainty analysis

Modeling the Dissolution of Immiscible Contaminants in Groundwater for Decision Support

Andres Eduardo Prieto Estrada

ABSTRACT

Predicting the dissolution rates of immiscible contaminants in groundwater is crucial for developing environmental remediation strategies, but quantitative modeling efforts are inherently subject to multiple uncertainties. These include unknown residual amounts of non-aqueous phase liquids (NAPL) and source zone dimensions, inconsistent historical monitoring of contaminant mass discharge, and the mathematical simulation of field-scale mass transfer processes. Effective methods for simulating NAPL dissolution must therefore be able to assimilate a variety of data through physical and scalable mass transfer parameters to quantify and reduce site-specific uncertainties. This investigation coupled upscaled and numerical mass transfer modeling with uncertainty analyses to understand and develop data-assimilation and parameter-scaling methods for characterizing NAPL source zones and predicting depletion timeframes.

Parameters of key interest regulating kinetic NAPL persistence and contaminant fluxes are residual mass and saturation, but neither can be measured directly at field sites. However, monitoring and characterization measurements can constrain source zone dimensions, where NAPL mass is distributed. This work evaluated the worth of source zone delineation and dissolution monitoring for estimating NAPL mass and mass transfer coefficients at multiple scales of spatial resolution. Mass transfer processes in controlled laboratory and field experiments were analyzed by simulating monitored dissolved-phase concentrations through the parameterization of explicit and lumped system properties in volume-averaged (VA) and numerical models of NAPL dissolution, respectively. Both methods were coupled with uncertainty analysis tools to investigate the relationship between data availability and model design for accurately constraining system parameters and predictions. The modeling approaches were also combined for reproducing

experimental bulk effluent rates in discretized domains, explicitly parameterizing mass transfer coefficients at multiple grid scales.

Research findings linked dissolved-phase monitoring signatures to model estimates of NAPL persistence, supported by source zone delineation data. The accurate characterization of source zone properties and kinetic dissolution rates, governing NAPL longevity, was achieved by adjusting model parameterization complexity to data availability. While multistage effluent rates accurately constrained explicit-process parameters in VA models, spatially-varying lumped-process parameters estimated from late dissolution stages also constrained unbiased predictions of NAPL depletion. Advantages of the numerical method included the simultaneous assimilation of bulk and high-resolution monitoring data for characterizing the distribution of residual NAPL mass and dissolution rates, whereas the VA method predicted source dissipation timeframes from delineation data alone. Additionally, comparative modeling analyses resulted in a methodology for scaling VA mass transfer coefficients to simulate NAPL dissolution and longevity at multiple grid resolutions. This research suggests feasibility in empirical constraining of lumped-process parameters by applying VA concepts to numerical mass transfer and transport models, enabling the assimilation of monitoring and source delineation data to reduce site-specific uncertainties.

Modeling the Dissolution of Immiscible Contaminants in Groundwater for Decision Support

Andres Eduardo Prieto Estrada

GENERAL AUDIENCE ABSTRACT

Predicting the dissolution rates of immiscible contaminants in groundwater is crucial for developing environmental restoration strategies, but quantitative modeling efforts are inherently subject to multiple uncertainties. These include unknown mass and dimensions of contaminant source zones, inconsistent groundwater monitoring, and the mathematical simulation of physical processes controlling dissolution rates at field scales. Effective simulation methods must therefore be able to leverage a variety of data through rate-limiting parameters suitable for quantifying and reducing uncertainties at contaminated sites. This investigation integrated mathematical modeling with uncertainty analyses to understand and develop data-driven approaches for characterizing contaminant source zones and predicting dissolution rates at multiple measurement scales.

Parameters of key interest regulating the lifespan of source zones are the distribution and amount of residual contaminant mass, which cannot be measured directly at field sites. However, monitoring and site characterization measurements can constrain source zone dimensions, where contaminant mass is distributed. This work evaluated the worth of source zone delineation and groundwater monitoring for estimating contaminant mass and dissolution rates at multiple measurement scales. Rate-limiting processes in controlled laboratory and field experiments were analyzed by simulating monitored groundwater concentrations through the explicit and lumped representation of system properties in volume-averaged (VA) and numerical models of contaminant dissolution, respectively. Both methods were coupled with uncertainty analysis tools to investigate the relationship between data availability and model design for accurately constraining system parameters and predictions. The approaches were also combined for predicting average contaminant concentrations at multiple scales of spatial resolution.

Research findings linked groundwater monitoring profiles to model estimates of contaminant persistence, supported by source zone delineation data. The accurate characterization of source zone properties and contaminant dissolution rates was achieved by adjusting model complexity to data availability. While monitoring profiles indicating multi-rate contaminant dissolution accurately constrained explicit-process parameters in VA models, spatially-varying lumped parameters estimated from late dissolution stages also constrained unbiased predictions of source mass depletion. Advantages of the numerical method included the simultaneous utilization of average and spatially-detailed monitoring data for characterizing the distribution of contaminant mass and dissolution rates, whereas the VA method predicted source longevity timeframes from delineation data alone. Additionally, comparative modeling analyses resulted in a methodology for scaling estimable VA parameters to predict contaminant dissolution rates at multiple scales of spatial resolution. This research suggests feasibility in empirical constraining of lumped parameters by applying VA concepts to numerical models, enabling a comprehensive data-driven methodology to quantify environmental risk and support groundwater cleanup designs.

Acknowledgements

I am profoundly grateful to Dr. Mark Widdowson, my doctoral advisor and professional mentor. Thank you for providing me with a unique opportunity for contributing to the field of groundwater modeling and remediation, meticulously guiding me throughout this challenging and rewarding endeavor. My deepest gratitude also goes to Dr. Lloyd "Bo" Stewart, my doctoral co-advisor and mentor as well. I have been extremely privileged by collaborating and learning closely from such creative and talented professionals.

Many thanks to Dr. Stanley Grant and to Dr. Thomas Burbey, members of my doctoral committee. Their valuable insights helped guide my research direction. I very much enjoyed taking their quantitative modeling classes, which were central to my doctoral program.

I would like to recognize Dr. John Doherty and Dr. Jeremy White, authors of PEST and PEST++ software. These tools were instrumental in answering many of my research questions. Thank you for consistently responding to my conceptual and implementation inquiries.

Thank you to Dr. Eduardo Mendez III for your assistance with model output settings, and Dr. Michael Mobile for helping me get started on model calibration. Likewise, thank you to Milko Maykowskyj and Alec Flint for helping me set up remote desktop access and for troubleshooting parallel computing issues. Thanks to your help I was able to accomplish modeling tasks critical to my research work.

I would like to thank the Environmental Security Technology Certification Program (ESTCP), hosted by the U.S. Department of Defense (DoD). The ESTCP provided the majority of the funding that supported my dissertation work, which included participating at scientific conferences.

Thank you to my parents Ramon Prieto and Norka Estrada, your encouragement and unconditional support have been vital during these difficult years. You have motivated me to persevere in my professional endeavors despite not seeing each other for many years while dealing with complicated economic, political, and health circumstances. Also, many thanks to my friends for your support from within and outside the U.S. Despite the physical distance, having close family and friends have made this doctoral journey even more worth it and enjoyable.

Thank you all!

Table of Contents

List of Figures

List of Tables

Chapter 1. Introduction and Attribution

Groundwater contamination by dense non-aqueous phase liquids (DNAPLs) is a ubiquitous environmental problem worldwide, particularly throughout industrialized nations with decades of chemical manufacturing and inadequate disposal of hazardous wastes (NRC, 2005; Kueper et al., 2013). Spills of industrial solvents and by-products, pesticides, dry cleaning fluids and degreasers, such as chlorinated solvents, have generated source zones of persistent and extensive subsurface contamination (NRC, 2005; Kueper et al., 2013). Slow dissolution rates of DNAPLs in groundwater are primarily driven by their low aqueous solubilities and limited hydraulic accessibility, contributing to source zone persistence without active remedial efforts (Mayer & Hassanizadeh, 2005; Brusseau et al., 2013). Although active remediation of DNAPL source zones can help mitigate long-term groundwater impacts, unavailability of detailed site- historical and/or characterization data, in addition to a lack of practical quantitative modeling methods, oftentimes leads to costly and ineffective management strategies (Rivett et al., 2014; Horst et al., 2018). Thus, developing modeling approaches capable of quantifying and reducing site-specific uncertainties, through the assimilation of all available data, is necessary to optimize remedial designs and reduce toxicological risks at sites impacted by DNAPL source zones (Abriola, 2005; Koch & Nowak, 2015; Kang et al., 2021; 2022).

A typical metric for reducing toxicological risk and achieving remedial objectives at contaminated sites is defined by maximum contaminant levels (MCLs) for drinking water standards (Hadley & Newell, 2012). Reaching MCLs at specific locations within reasonable timeframes in groundwater systems is largely dependent on source zone management strategies for reducing mass discharge (MD) and flux (J) rates (ITRC, 2010; Lebron et al., 2012). As shown in Figure 1-1, source MD and J can be monitored at multiple downgradient transects and scales of spatial resolution to estimate timeframes of source mass depletion and to evaluate remedial technology performance (Stroo et al., 2012; Brusseau et al., 2013). However, designing effective strategies for long-term management of source zones requires knowledge of DNAPL mass distribution in the subsurface, referred to as the source zone "architecture." Although the source zone architecture plays a primary role in regulating field-scale MD rates (Illangasekare et al., 2006; Rivett et al., 2014; Annable et

al., 2017), characterizing DNAPL mass and distribution by direct field observation methods is not possible (Eniarson et al., 2018; Engelmann et al., 2019).

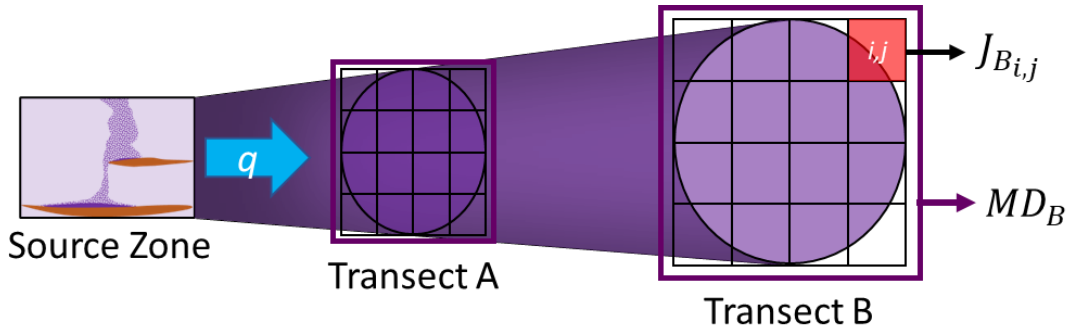

Figure 1-1. Illustration of mass discharge (MD) and mass flux (J) measurement concepts. The sum of J [M T^{-1} L^{-2}] measurements over a given area perpendicular to the downgradient Darcy flux q [L T^{-1}] direction is equivalent to the MD rate [M T^{-1}] at a monitoring transect.

Source zone architectures are formed through DNAPL trapping by capillary and viscous forces during downward and lateral migration in saturated aquifers (Dekker & Abriola, 2000). As shown in Figure 1-2, a typical source zone architecture is comprised of residual ganglia, high-saturation pools, sorbed and dissolved constituents, and constituents diffused into fine-grained media (Kueper et al., 2013). Ganglia zones consist of disconnected blobs occupying approximately less than 20% of the pore space, while pool zones consist of continuous DNAPL accumulations with residual saturations approximately greater than 20% (Christ et al., 2006, 2010). The greater interfacial area of residual ganglia often yields a high contaminant mass flux, whereas pooled DNAPL sustains a lower mass flux for longer time periods, resulting in a combined "multi-stage" dissolution behavior typically observed in monitoring systems (Lemke & Abriola, 2004, 2006). Predicting and explaining field-scale DNAPL dissolution trends through quantitative modeling methods are of key interest for effective site management support (Parker & Park, 2004; Park & Parker, 2005; Kokkinaki et al., 2014).

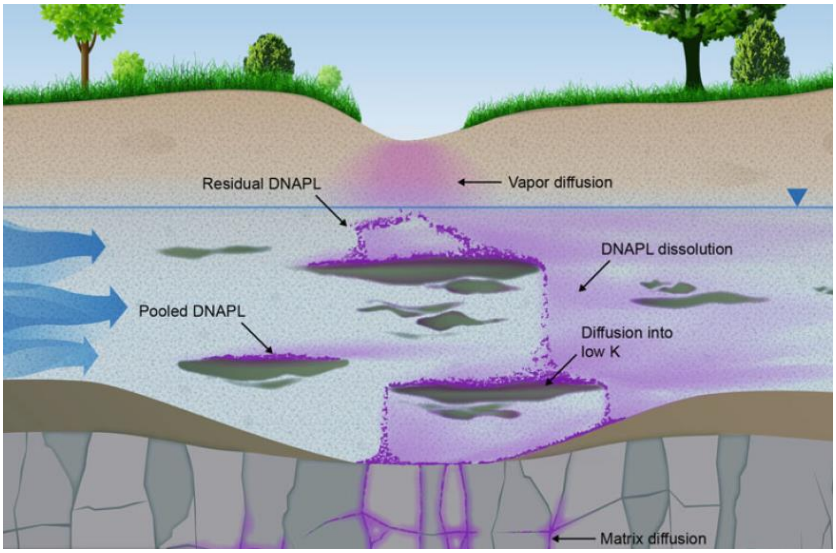

Figure 1-2. Schematic of DNAPL source zone (adapted from Kueper et al. 2013)

Approaches for simulating DNAPL dissolution range from screening models lacking a physical basis to complex multiphase and pore-scale numerical models with impractical data requirements (Agaoglu et al., 2015; Stewart et al., 2022). Similarly, although computationally efficient, predictive upscaled models have input requirements on overly specific source zone metrics, limiting their general practical applicability (Stewart et al., 2022). Examples include a dual-domain ganglia-to-pool mass ratio model (Christ et al., 2010), the equilibrium streamtube model (Jawitz et al., 2003; Basu et al., 2008), an upscaled Gilland-Sherwood correlation (Saenton & Illangasekare, 2007), and a thermodynamic interfacial area model (Kokkinaki et al., 2013); all requiring detailed information on residual saturation distributions which cannot be measured directly at sites (Eniarson et al., 2018). Moreover, inverse modeling approaches have proved useful for estimating field-scale mass transfer parameters (Park & Parker, 2005; Mobile et al., 2012; 2016), but predictions on future system behavior may be limited to the historical observation period leaving significant unquantified uncertainties (Marble et el., 2008; Parker et al., 2010). These shortcomings have incentivized the need to develop practical and scientifically-based modeling approaches to readily estimate mass fluxes and depletion timeframes of DNAPL source zones by assimilating all types of available site data (Kueper et al., 2013). Such a modeling framework could be used to evaluate and refine site conceptual assumptions while quantifying and reducing predictive uncertainties, including the downgradient plume response.

In this research, a volume-averaged (VA) modeling system (Stewart et al., 2022) and the SEAM3D numerical modeling program (Waddill & Widdowson, 2000) were used to quantify DNAPL mass transfer parameters and predictive uncertainties derived from a variety of source zone characterization and monitoring datasets at multiple measurement scales. The primary objective was to elucidate the advantages and limitations of these modeling tools, including an examination of a combined modeling approach for improving decision-support capabilities. Specifically, because the VA model possesses a physical basis for simulating DNAPL mass transfer processes explicitly, both site characterization and monitoring data can be leveraged for predicting source mass discharge rates and depletion timeframes (Stewart et al., 2022). However, its main advantage is also its primary limitation; i.e., volume averaging trades off spatial specificity for computational efficiency. Fast model runtimes facilitate the quantification of predictive source-zone uncertainties, but the evolution of downgradient contaminant plumes cannot be jointly evaluated with the current approach. Conversely, the SEAM3D NAPL dissolution model does not include an explicit representation of mass transfer coefficients, but numerical modeling allows for estimating system parameters from monitoring data at multiple measurement scales to jointly evaluate the downgradient contaminant plume evolution, including complex, spatially-varying attenuation (biodegradation) processes. Therefore, combining both approaches has potential for evaluating the outcome of management scenarios at field sites in a computationally efficient manner, which is necessary for parameter estimation and uncertainty quantification (Doherty & Moore, 2020). The following chapters were developed to elucidate upon modeling techniques useful for characterizing and predicting source zone depletion at DNAPL-impacted sites:

Chapter 2:

Although the VA model can reproduce complex DNAPL dissolution profiles by parameterizing source zone dimensions and flow-field heterogeneities measured in controlled experiments, such level of site characterization detail is likely unavailable at contaminated sites. In turn, history matching of monitoring profiles to estimate mass transfer parameters may bias model predictions through inadequate source zone conceptual assumptions. This chapter investigated the level of parameterization complexity required to produce unbiased predictions of source zone depletion, assuming data availability on source delineation and discharge concentrations with various spatial

and temporal resolutions. Datasets of highly characterized bench-scale experiments of DNAPL dissolution were leveraged with the VA model coupled to uncertainty quantification tools to evaluate how conceptual assumptions drive predictive uncertainties.

The manuscript for this work was submitted to *Water Resources Research*. Co-authors include Dr. Mark Widdowson (Conceptualization, Funding Acquisition, Methodology, Review and Editing) and Dr. Lloyd Stewart (Conceptualization, Funding Acquisition, Methodology, Review and Editing, Software)

Chapter 3:

Previous research efforts have shown how spatially-varying mass transfer coefficients can be estimated through inverse SEAM3D modeling to characterize source zone depletion. This chapter expanded on previous work by investigating how to leverage a high-resolution multilevel monitoring transect to simultaneously characterize the architecture and mass transfer coefficients of a multicomponent DNAPL source zone, which cannot be measured directly at contaminated sites. Data-worth and nonlinear uncertainty analysis tools were coupled to a 3D numerical model to evaluate and quantify the link between parameter uncertainties and high-resolution monitoring of a controlled field experiment.

The manuscript for this work was accepted for publication in *Water Resources Research*. Co-authors include Dr. Mark Widdowson (Funding Acquisition, Conceptualization, Methodology, Review and Editing, Software) and Dr. Lloyd Stewart (Funding Acquisition, Review and Editing)

Chapter 4:

This chapter explored the application of VA mass transfer concepts in discretized SEAM3D models of DNAPL dissolution and aqueous-phase transport. The variability of mass transfer coefficients, mass discharge rates, and DNAPL longevity with numerical grid resolution was examined by a combination of inverse and forward numerical modeling analyses, using VA models and experimental effluent data as reference metrics. Datasets included highly characterized

flow-cell experiments focusing on the dissolution of chlorinated-solvent pools. Physical VA model predictions of DNAPL pool depletion were leveraged to find empirical relationships between source architectural dimensions and numerical grid resolution, which included vertical hydrodynamic dispersion in both mass transfer and transport simulations. Comparative SEAM3D-VA modeling analyses were focused on investigating methods for scaling VA mass transfer coefficients to constrain lumped-process parameters in discretized domains.

The manuscript for this work will be submitted to *Water Resources Research*. Co-authors include Dr. Mark Widdowson (Funding Acquisition, Methodology, Review and Editing, Software) and Dr. Lloyd Stewart (Conceptualization, Funding Acquisition, Methodology, Review and Editing, Software)

References

Abriola, L. M. (2005). Guest Editorial: Contaminant Source Zones: Remediation or Perpetual Stewardship? *Environmental Health Perspectives, 113*(7), A438-A439. https://doi.org/10.1289/ehp.113-a438

Agaoglu, B., Copty, N. K., Scheytt, T., & Hinkelmann, R. (2015). Interphase mass transfer between fluids in subsurface formations: A review. *Advances in Water Resources, 79*, 162-194. https://doi.org/10.1016/j.advwatres.2015.02.009

Annable, M. D., Hatfield, K., Jawitz, J. W., Brooks, M. C., Wood, A. L., & Rao, P. S. (2017). *Predicting DNAPL Source Zone and Plume Response Using Site-Measured Characteristics.* Gainsville, FL: Strategic Environmental Research and Development Program, Final Report ER-1613.

Basu, N. B., Fure, A. D., & Jawitz, J. W. (2008). Predicting dense nonaqueous phase liquid dissolution using a simplified source depletion model parameterized with partitioning tracers. *Water Resources Research, 44*(7). https://doi.org/:10.1029/2007WR006008

Brusseau, M. L., Matthieu III, D. E., Carroll, K. C., Mainhagu, J., Morrison, C., McMillan, A., . . . Plaschke, M. (2013). Characterizing Long-term Contaminant Mass Discharge and the Relationship Between Reductions in Discharge and Reductions in Mass for DNAPL Source Areas. *Journal of Contaminant Hydrology*, 1-12. https://doi.org/10.1016/j.jconhyd.2013.02.011

Christ, J. A., Ramsburg, A. C., Pennell, K. D., & Abriola, L. M. (2006). Estimating mass discharge from dense nonaqueous phase liquid source zones using upscaled mass transfer coefficients: An evaluation using multiphase numerical simulations. *Water Resources Research, 42*(11). https://doi.org/10.1029/2006WR004886

Christ, J. A., Ramsburg, C. A., Pennell, K. D., & Abriola, L. M. (2010). Predicting DNAPL mass discharge from pool-dominated source zones. *Journal of Contaminant Hydrology, 114*(1-4), 18 - 34. https://doi.org/10.1016/j.jconhyd.2010.02.005

Dekker, T. J., & Abriola, L. M. (2000). The influence of field-scale heterogeneity on the infiltration and entrapment of dense nonaqueous phase liquids in saturated formations. *Journal of Contaminant Hydrology, 42*(2-4), 187-218. https://doi.org/10.1016/S0169-7722(99)00092-3

Doherty, J., & Moore, C. (2020). Decision Support Modeling: Data Assimilation, Uncertainty Quantification, and Strategic Abstraction. *Groundwater, 58*(3), 327-337. https://doi.org/10.1111/gwat.12969

Engelmann, C., Handel, F., Binder, M., Yadav, P. K., Dietrich, P., Liedl, R., & Walther, M. (2019). The fate of DNAPL contaminants in non-consolidated subsurface systems – Discussion on the relevance of effective source zone geometries for plume propagation. *Journal of Hazardous Materials, 375*, 233-240. https://doi.org/doi.org/10.1016/j.jhazmat.2019.04.083

Eniarson, M., Fure, A., St. Germain, R., Chapman, S., & Parker, B. (2018). DyeLIF™: A New Direct-Push Laser-Induced Fluorescence Sensor System for Chlorinated Solvent DNAPL and Other Non-Naturally Fluorescing NAPLs. *Groundwater Monitoring & Remediation*, 28-42. https://doi.org/10.1111/gwmr.12296

Hadley, P. W., & Newell, C. J. (2012). Groundwater Remediation: The Next 30 Years. *Groundwater, 50*(5), 669-678. https://doi.org/10.1111/j.1745-6584.2012.00942.x

Horst, J., Welty, N., Stuetzle, R., Wenzel, R., & Germain, R. (2018). Fluorescent dyes: A new weapon for conquering DNAPL characterization. *Groundwater Monitoring & Remediation, 38*(1), 19-25. https://doi.org/10.1111/gwmr.12261

Illangasekare, T. H., Marr, J. M., Siegrist, R. L., & Soga, K. (2006). *Mass Transfer from Entrapped DNAPL Sources Undergoing Remediation: Characterization Methods and Prediction Tools.* SERDP Project No. CU-1294.

ITRC (Interstate Technology & Regulatory Council). (2010). *Use and Measurement of Mass Flux and Mass Discharge.* Washington, D.C.: Interstate Technology & Regulatory Council, Integrated DNAPL Site Strategy Team. Retrieved from www.itrcweb.org

Jawitz, J. W., Annable, M. D., Demmy, G. G., & Rao, P. S. (2003). Estimating nonaqueous phase liquid spatial variability using partitioning tracer higher temporal moments. *Water Resources Research, 39*(7).

Kang, X., Kokkinaki, A., Kitandis, P. K., Shi, X., Lee, J., Mo, S., & Wu, J. (2021). Hydrogeophysical Characterization of Nonstationary DNAPL Source Zones by Integrating a Convolutional Variational Autoencoder and Ensemble Smoother. *Water Resources Research, 57*(1). https://doi.org/10.1029/2020WR028538

Kang, X., Kokkinaki, A., Shi, X., Yoon, H., Lee, J., Kitandis, P. K., & Wu, J. (2022). Integration of Deep Learning-Based Inversion and Upscaled Mass-Transfer Model for DNAPL Mass-Discharge Estimation and Uncertainty Assessment. *Water Resources Research, 58*(10). https://doi.org/10.1029/2022WR033277

Koch, J., & Nowak, W. (2015). Predicting DNAPL mass discharge and contaminated site longevity probabilities: Conceptual model and high-resolution stochastic simulation. *Water Resources Research, 51*(2), 806 - 831. https://doi.org/10.1002/2014WR015478.

Kokkinaki, A., O'Carroll, M., Werth, C. J., & Sleep, B. E. (2013). Coupled simulation of DNAPL infiltration and dissolution in three-dimensional heterogeneous domains: Process model validation. *Water Resources Research, 49*, 7023-7036. https://doi.org/10.1002/wrcr.20503, 2013

Kokkinaki, A., Werth, C. J., & Sleep, B. E. (2014). Comparison of upscaled models for multistage mass discharge from DNAPL source zones. *Water Resources Research*, 3187 - 3205. https://doi.org/10.1002/2013WR014663

Kueper, B. H., Stroo, H. F., Vogel, C. M., & Ward, C. H. (2014). *Chlorinated Solvent Source Zone Remediation.* Springer New York. https://doi.org/10.1007/978-1-4614-6922-3

Lebron, C. A., Major, D., Konzuk, J., Kueper, B. H., & Gerhard, J. (2012). *Development of a Protocol and a Screening Tool for the Selection of DNAPL Source Area Remediation.* ESTCP Project ER0424. Port Hueneme, CA: NAVFAC Engineering Service Center.

Lemke, L. D., & Abriola, L. M. (2004). DNAPL source zone characterization: Influence of hydraulic property correlation on predictions. *Water Resources Research, 10*(12). https://doi.org/10.1029/2003WR001980

Lemke, L. D., & Abriola, L. M. (2006). Modeling dense nonaqueous phase liquid mass removal in nonuniform formations: Linking source-zone architecture and system response. *Geosphere, 2*(2), 74-82. https://doi.org/10.1130/GES00025.1

Marble, J. C., DiFilippo, E. L., Zhang, Z., Tick, G. R., & Brusseau, M. L. (2008). Application of a lumped-process mathematical model to dissolution of non-uniformly distributed immiscible liquid in heterogeneous porous media. *Journal of Contaminant Hydrology, 100*, 1-10. https://doi.org/10.1016/j.jconhyd.2008.04.003

Mayer, A. S., & Hassanizadeh, M. S. (2005). *Soil and Groundwater Contamination: Nonaqueous Phase Liquids–Principles and Observations.* Washington, D.C.: American Geophysical Union.

Mobile, M. A., Widdowson, M. A., & Gallagher, D. L. (2012). Multicomponent NAPL Source Dissolution: Evaluation of Mass-Transfer Coefficients. *Environmental Science & Technology, 46*(18), 10047-10054. https://doi.org/10.1021/es301076p

Mobile, M., Widdowson, M., Stewart, L., Nyman, J., Deeb, R., Kavanaugh, M., . . . Gallagher, D. (2016). In-situ determination of field-scale NAPL mass transfer coefficients: Performance, simulation and analysis. *Journal of Contaminant Hydrology, 187*, 31-46. https://doi.org/10.1016/j.jconhyd.2016.01.010

National Research Council. (2005). *Contaminants in the subsurface: Source zone assessment and remediation.* Washington, D.C.: The National Academic Press.

Park, E., & Parker, J. C. (2005). Evaluation of an upscaled model for DNAPL dissolution kinetics in heterogeneous aquifers. *Advances in Water Resources*, 1280-1291. https://doi.org/10.1016/j.advwatres.2005.04.002

Parker, J. C., & Park, E. (2004). Modeling field-scale dense nonaqueous phase liquid dissolution kinetics in heterogeneous aquifers. *Water Resources Research, 2004*. https://doi.org/10.1029/2003WR002807

Parker, J. C., Kim, U., Widdowson, M., Kitandis, P., & Gentry, R. (2010). Effects of model formulation and calibration data on uncertainty in dense nonaqueous phase liquids source dissolution predictions. *Water Resources Research, 46*, W12517. https://doi.org/10.1029/2010WR009361

Rivett, M. O., Dearden, R. A., & Wealthall, G. P. (2014). Architecture, persistence and dissolution of a 20 to 45 year old trichloroethene DNAPL source zone. *Journal of Contaminant Hydrology, 170*, 95-115. https://doi.org/10.1016/j.jconhyd.2014.09.008

Saenton, S., & Illangasekare, T. H. (2007). Upscaling of mass transfer rate coefficient for the numerical simulation of dense nonaqueous phase liquid dissolution in heterogeneous aquifers. *Water Resources Research, 43*(2). https://doi.org/10.1029/2005WR004274

Stewart, L. D., Chambon, J. C., Widdowson, M. A., & Kavanaugh, M. C. (2022). Upscaled modeling of complex DNAPL dissolution. *Journal of Contaminant Hydrology, 244*, 103920. https://doi.org/10.1016/j.jconhyd.2021.103920

Stroo, H. F., Leeson, A., Marqusee, J. A., Johnson, P. C., Ward, C. H., Kavanaugh, M. C., . . . Unger, M. (2012). Chlorinated Ethene Source Remediation: Lessons Learned. *Environmental Science & Technology, 46*, 6438−6447. https://doi.org/10.1021/es204714w

Waddill, D. W., & Widdowson, M. A. (2000). *SEAM3D: A numerical model for three-dimensional solute transport and sequential electron acceptor-based bioremediation in groundwater*. ERDC/EL TR- 00-18. U.S. Army Engineer Research and Development Center, Vicksburg, MS.

Chapter 2. Quantifying DNAPL source zone longevity with upscaled modeling: practical insights from flow-cell experiments and uncertainty analyses

This chapter was submitted to *Water Resources Research* on December 17, 2022.

2.1. Authors

Andres E. Prieto-Estrada[1], Mark A. Widdowson[1], and Lloyd D. Stewart[2]

[1] The Charles E. Via, Jr. Department of Civil and Environmental Engineering, Virginia Tech, Blacksburg, Virginia 24061-0105, United States

[2] Praxis Environmental Technologies, Inc., 1440 Rollins Road, Burlingame, California 94010, United States

2.2. Key Points

- Upscaled modeling and uncertainty analyses of flow-cell experiments elucidated upon data assimilation strategies at DNAPL sites
- Parameterization of source zone heterogeneities for history-matching was necessary to predict unbiased DNAPL dissolution timeframes
- Coarse DNAPL delineation sufficed to quantify unbiased uncertainty limits of source zone lifespans a priori

2.3. Abstract

Estimating dissipation timeframes and contaminant mass discharge rates of dense non-aqueous phase liquids (DNAPLs) source zones is of key interest for environmental-management support. Upscaled mathematical modeling of DNAPL dissolution provides a practical approach for assimilating site characterization and downgradient monitoring data to constrain future system behavior. Yet significant uncertainties on predictions of source zone dissipation rates may arise from inadequate or inaccurate conceptual assumptions in parameterization designs. These implications were investigated through upscaled modeling, sensitivity, and uncertainty analyses of

high-resolution flow-cell experiments. Sensitivity results emphasized the role of local groundwater velocity and source dimensions in mass transfer scaling by strongly influencing error with respect to DNAPL persistence and dissolution rates. Linear uncertainty analyses, facilitated by PEST ancillary software, demonstrated the worth of monitoring profiles for constraining DNAPL saturations and dispersive mass transfer rates, responsible for source zone longevity. Nonlinear analyses performed with the iterative ensemble smoother PESTPP-iES, facilitated the quantification of unbiased source dissipation uncertainties from DNAPL delineation data. Conversely, monitoring data assimilation without consideration of flow-field heterogeneity and saturation distribution along the flow path biased model predictions. Our analyses provided practical recommendations on upscaled model design to assimilate available site data and support remedial designs.

2.4. Plain Language Summary

Currently, environmental restoration managers makers rarely benefit from physically-based modeling methods and uncertainty analyses to manage sites impacted by DNAPL source zones. Difficulties in estimating DNAPL dissolution rates stem from source zone heterogeneities, which are difficult to characterize in detail, compounded by a lack of scalable methodologies connecting source zone characterization with discharge monitoring. In addition, monitoring and site characterization efforts supporting performance-based remedial objectives are typically uninformed by uncertainty evaluations predicated on DNAPL mass transfer processes. To bridge that gap, we investigated the impact of data-driven conceptual assumptions on predictions of source zone behavior by coupling a practical DNAPL dissolution model with uncertainty quantification methods. Simulations of flow-cell experiments demonstrated the worth of DNAPL delineation for constraining source zone dissipation uncertainties, estimated a priori through parameterization of DNAPL distributions. In turn, parameterizing system heterogeneities in greater detail was necessary to estimate unbiased source zone characteristics and lifespans, derived from the assimilation of complex DNAPL dissolution trends observed in monitoring profiles. Our results demonstrated how available site data can be integrated into a decision-support modeling framework to inform data collection strategies and remedial designs.

2.5. Keywords

Source zone persistence, source zone heterogeneity, DNAPL dissolution rates, conceptual assumptions, data assimilation, model parameterization, remedial-decision making, practical recommendations

2.6. Introduction

Mathematical modeling can provide valuable insights for decision support at hazardous waste sites with groundwater impacted by dense non-aqueous phase liquids (DNAPLs). However, a gap between simplistic analytical screening models and overly complex numerical simulators has limited their applicability for estimating DNAPL longevity and dissolution rates. Researchers have focused on estimating distributions of DNAPL saturation, referred to as the source zone architecture, or DNAPL dissolution rates from synthetically-generated datasets using several mathematical approaches to simulating mass transfer. Several studies considered either a local equilibrium assumption (LEA) or Gilland-Sherwood models of interphase mass transfer (Kang et al. 2021a; Powers et al., 1992, 1994; Saenton & Illangasekare, 2004).

Decision-support modeling incorporating LEA is questionable because heterogeneity of aquifer hydraulic properties and source architecture can induce flow bypassing and mass transfer rate limitations, resulting in nonequilibrium concentrations typically observed at field sites (Falta, 2003; Kokkinaki et al., 2013). Similarly, Gilland-Sherwood models rely on correlations between empirical coefficients and soil particle sizes that were determined under specific bench-scale conditions, which may not be applicable to field-scale problems with different hydraulic properties (Powers et al., 1992; Saenton & Illangasekare, 2007). Moreover, the computational cost of pore-scale numerical models incorporating LEA and Gilland-Sherwood correlations limits their practicality for data assimilation and uncertainty quantification (Falta, 2003; Kokkinaki et al., 2013; Powers et al., 1994). An alternative method is predicated on a lumped-process, scale-dependent mass transfer coefficient estimated from monitoring data (Guo et al., 2020; Mobile et al., 2012; Park & Parker, 2005). However, estimating mass transfer rates exclusively from

historical monitoring may bias predictions of source longevity because of architectural changes. For example, early in the life cycle of a DNAPL source zone, the contributions of slowly dissolving pools governing complete depletion may not be discernible in discharge data (Abriola et al., 2013).

Multistage DNAPL dissolution, typically observed at contaminated sites and in dissolution experiments, arises from heterogeneity of source zone architecture (Figure 2-1) primarily comprised by residual ganglia and high-saturation DNAPL pools (Christ et al., 2010; Dekker & Abriola, 2000; DiFilippo & Brusseau, 2008; Lemke & Abriola, 2006; Parker & Park, 2004). Consequently, a number of high-resolution site characterization (HRSC) technologies have been developed (Einarson et al., 2018; Horst et al., 2018; Kueper et al., 2014). Delineation of DNAPLs comprised by chlorinated ethenes is possible with dye-enhanced laser induced fluorescence (DyeLIF) and confirmatory sampling, and with indirect observation methods, such as multilevel monitoring and groundwater extraction systems, passive flux meters, push-pull tracer tests, etc. (Horst et al. 2018; Huang et al. 2010; ITRC, 2010; Kueper et al., 2014). Although HRSC may help constrain DNAPL distribution, quantifying residual mass and saturation directly is not possible (Einarson et al., 2018). Thus, inverse modeling techniques have been applied to quantify lumped-process mass transfer coefficients from monitoring data Marble et al., 2008; Mobile et al., 2012; Saenton & Illangasekare, 2004), or to estimate source zone architectures from borehole and geophysical measurements using physically-based parameterization mechanisms (Kang et al. 2021a, 2021b). Kang et al. (2022) demonstrated a novel Bayesian inversion framework to reconstruct complex permeability and DNAPL saturation fields, subsequently parameterizing an upscaled model of DNAPL dissolution to reproduce experimental source depletion trends.

Upscaled (domain-averaged) models lacking a physical mass transfer basis cannot assimilate HRSC data and have proved ineffective at explaining and predicting DNAPL dissolution behavior (Christ et al., 2006; Kokkinaki et al., 2014; Marble et al., 2008). However, upscaled models incorporating metrics describing the source zone architecture, such as the ganglia-to-pool (GTP) mass ratio, have shown improved success (Abriola et al. 2013; Christ et al., 2010; DiFilippo & Brusseau, 2011). Stewart et al. (2021) developed a volume-averaged (VA) model of DNAPL dissolution predicated on characteristic length scales of DNAPL accumulations and their relative location along groundwater flow paths, explicitly accounting for mass transfer processes at the

source zone scale (Figure 2-1). The model accurately reproduced complex DNAPL dissolution observed in laboratory, numerical, and field experiments by parameterizing initial, and estimable system characteristics without undertaking history-matching. The VA model is therefore able to assimilate HRSC and/or monitoring data to estimate source dissipation timeframes with computational efficiency in a scalable and physically-based manner. Such capabilities make the VA model suitable for evaluating site conceptual assumptions and quantifying uncertainties, which is necessary for effective remedial-decision support (Abriola, 2005).

The primary objectives in this work were to (i) identify the relative contribution of VA mass transfer parameters to source zone dissipation uncertainties, and (ii) investigate how model parameterization influences predictive bias through monitoring data assimilation. The VA DNAPL dissolution model developed by Stewart et al. (2021) was coupled with sensitivity and uncertainty analysis methods to evaluate the worth of direct and indirect source zone measurements for constraining system parameters and model uncertainty. High-resolution datasets of two DNAPL dissolution experiments were leveraged to evaluate data-driven conceptual assumptions on modeling outcomes. Our findings clarify the level of model complexity necessary to quantify unbiased DNAPL persistence uncertainties, yielding recommendations on HRSC and monitoring data assimilation for constraining future source zone behavior.

2.7. Upscaled and Volume-Averaged Model of DNAPL Dissolution

Volume-averaging relaxes the need to specify precise locations of DNAPL accumulations within a finely discretized domain. The approach facilitates the incorporation of physically-based mass transfer relationships for complex field-scale dissolution behavior with computational efficiency. As presented by Stewart et al. (2021), dissolution of a single DNAPL accumulation, defined as a volume of relative uniformity in saturation, can be simulated by a generalized upscaled mass transfer function:

$$k_a = \frac{U_0}{V_S}\left[A_{a,yz}k_r(m_a) + A_{a,xy}\sqrt{\frac{4\alpha_T}{\pi X_a}}\right]\left(\frac{m_a}{m_{a,0}}\right)^{\gamma} \tag{2-1}$$

where interphase mass transfer (k_a^N) [T^{-1}] from an individual DNAPL accumulation *"a"* is driven by the local Darcy groundwater velocity (U_0) [$L\ T^{-1}$] upscaled by a source zone reference volume (V_S) [L^3] encompassing the DNAPL masses. The term on the left inside the brackets represents dissolution attributable to through flow (Figure 2-1c), which is proportional to the projected area facing flow ($A_{a,yz} = Y_a Z_a$ [L^2]) of *a*. Flow through *a* is regulated by the soil relative permeability (k_r) which gradually increases the DNAPL dissolution rate as the DNAPL volume is reduced. The term on the right represents dissolution attributable to dispersion into bypassing flow (Figure 2-1d), which is proportional to the hydrodynamic transverse dispersivity (α_T) [L] around *a* and the horizontal area of the accumulation ($A_{a,xy} = X_a Y_a$ [L^2]). Mass dissolution from low DNAPL saturations, i.e., ganglia, are dominated by flow through, while high saturation zones, i.e., pools, can be dominated by dispersion. The normalized mass (m/m_0) term reflects a transient reduction of DNAPL interfacial area. Theoretically, the dimensionless exponent $\gamma = 2/3$ for ganglia-dominated accumulations, and $\gamma = ½$ for pool-dominated accumulations. The γ exponent may be adjusted during model history-matching to allow for deviations from conceptual mass transfer assumptions but is expected to fall within this relatively narrow range (Stewart et al., 2021)**Error! Reference source not found.**.

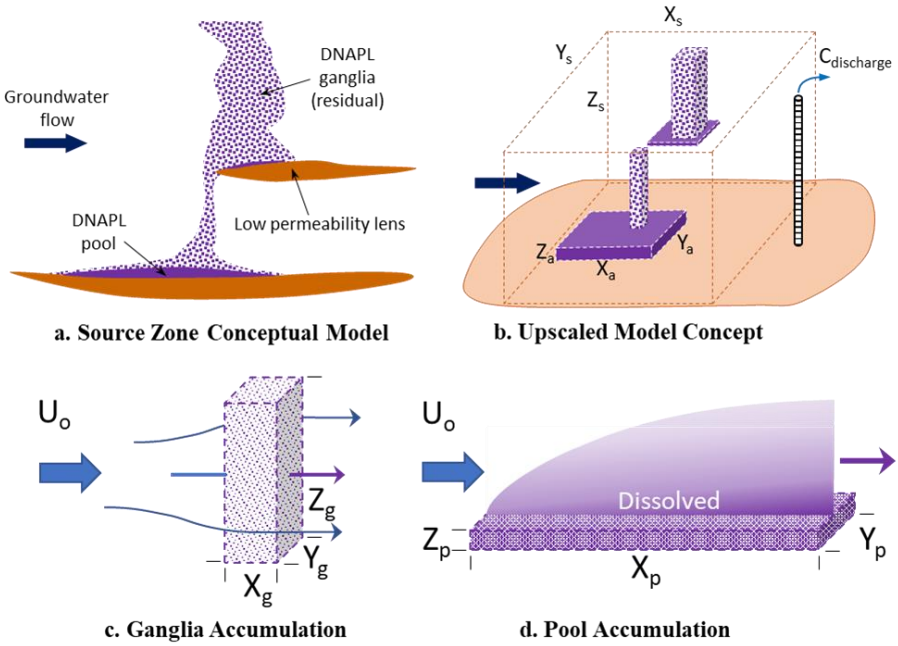

Figure 2-1. Conceptual and volume-averaged model representations (a and b, respectively) of a DNAPL source zone comprised by characteristic accumulations of (c) residual ganglia and (d) pools. Adapted from Stewart et al. (2021).

2.7.1. Simulation of DNAPL Dissolution Experiments

Flow-cell experiments presented by DiFilippo et al. (2010) and analyzed by Guo et al. (2020) with a simplified inverse modeling method were utilized in this study. Stewart et al. (2021) simulated these experiments with the VA approach by explicitly accounting for DNAPL saturation distributions, flow field characteristics, and soil properties. The dissolution experiments consisted of two source zone scenarios: a "mixed" DNAPL architecture comprised by a ganglia-dominated accumulation and a pool-dominated accumulation in homogeneous sand, and multiple DNAPL accumulations in a "heterogeneous" soil. Details of model conceptualization and simulation results were presented in Stewart et al. (2021).

2.7.1.1. Mixed DNAPL Architecture

The "mixed" source zone experiment conducted by DiFilippo et al. (2010) consisted of a uniform pack of sand (40/50 mesh) with a 2-cm thick capillary barrier located along the bottom of the test cell (Figure 2-2a). An injection of ~12 milliliters of trichloroethene (TCE) at the top of the test cell followed by 48-hour period prior to flow initiation generated a stable source zone architecture consisting of a vertical ganglia zone underlain by a pool. The DNAPL saturation distribution was characterized using a light reflection visualization (LRV) method and TCE effluent concentrations were monitored until source zone depletion.

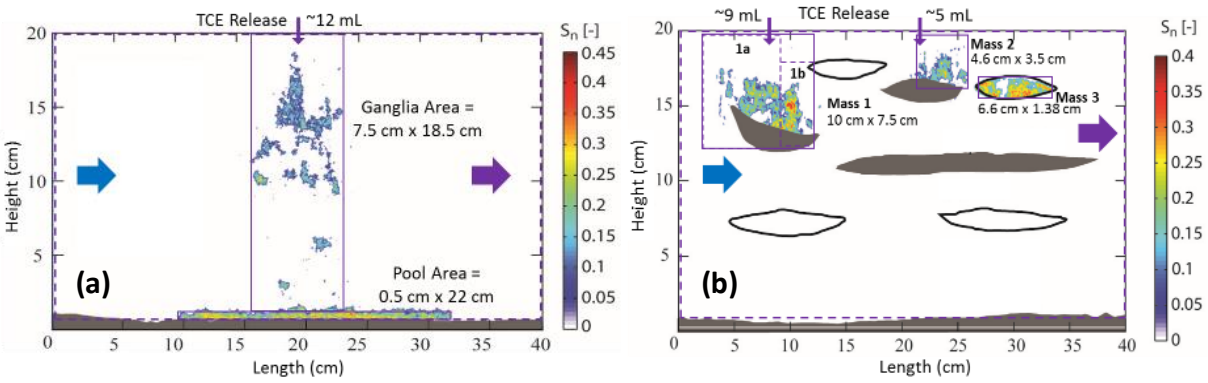

Figure 2-2. Model conceptualizations of the flow-cell experiments: (a) mixed source zone architecture and (b) heterogeneous source zone. Sub-volumes (purple rectangles) correspond to DNAPL accumulations with distinct saturations encompassed by the source volume (purple dashed line). Adapted from Stewart et al. (2021).

2.7.1.2. Multiple DNAPL accumulations in Heterogeneous Soil

The test cell of the heterogeneous source experiment (Figure 2-2b) consisted of a matrix of homogeneous sand (40/50 mesh) with coarser (20/30 mesh) and finer (70/100 mesh) lenticular zones (DeFilippo et al., 2010; Guo et al., 2020). An injection of ~15 milliliters of TCE at the top of the cell was distributed between two ports with 66% in the far left (upgradient) port and 33% in the center (downgradient) port (DeFilippo et al. 2010). The central release generated two distinct accumulations: one above a fine-grained lens and one within a coarse-grained lens. The coarse lens had an intrinsic permeability approximately 3.5 times higher than the surrounding bulk sands (DeFilippo et al., 2010), resulting in a higher velocity through this material than in the surrounding matrix. As shown in Figure 2-2b, Stewart et al. (2021) subdivided the upgradient accumulation into two accumulations on the basis of characteristic saturations to accurately capture the measured TCE effluent breakthrough. Sequential dissolution inhibition was also implemented by Stewart et al. (2021) for the two downgradient accumulations on the basis of their relative locations along the flow path. Nomenclature for variables in the model are presented in Table 2-1.

Table 2-1. Nomenclature of input parameters used in the VA model of the flow-cell experiments.

Parameter	**Mixed Source**		**Heterogeneous Source**				**Unit**
Mass	*Mass G.*	*Mass P.*	*Mass 1A*	*Mass 1B*	*Mass 2*	*Mass 3*	g
Length	X_g	X_p	X_{1A}	X_{1B}	X_2	X_3	m
Width	Y_g	Y_p	Y_{1A}	Y_{1B}	Y_2	Y_3	m
Height	Z_g	Z_p	Z_{1A}	Z_{1B}	Z_2	Z_3	m
NAPL Saturation	S_g^N	S_p^N	S_{1A}^N	S_{1B}^N	S_2^N	S_3^N	%
Area Facing Flow	YZ_g	YZ_p	YZ_{1A}	YZ_{1B}	YZ_2	YZ_3	m^2
Dispersive Area	XY_g	XY_p	XY_{1A}	XY_{1B}	XY_2	XY_3	m^2
Dispersivity	$\alpha_{T,g}$	$\alpha_{T,p}$	$\alpha_{T,1A}$	$\alpha_{T,1B}$	$\alpha_{T,2}$	$\alpha_{T,3}$	m
γ	γ^g	γ^p	γ^{1A}	γ^{1B}	γ^2	γ^3	-

2.7.2. Sensitivity Analysis

Model output variability was evaluated with local sensitivity analysis by systematically perturbing input parameters around reference values conceptualized in Stewart et al. (2021). The goal was to compare relative sensitivities with respect to measured discharge concentrations and with respect to the time required to reach cleanup concentrations, defined here as time of remediation (TOR). Both metrics were evaluated using the same model input variability around base parameter sets. Because the plausible variability range of some parameters and their corresponding outputs differs by orders of magnitude compared to those of other parameters, sensitivity coefficients were scaled by maximum values to provide a relative comparison metric of simulation error. All sensitivity analyses were automated coupling SENSAN and PEST software (Watermark Numerical Computing, 2018) for calculation fidelity.

2.7.2.1. Sensitivities with respect to TCE discharge concentrations

Normalized sensitivity coefficients (X_{TCE}) were calculated on the basis of root mean squared errors (RMSE) between simulated (sim_i) and measured (obs_i) discharge concentrations as:

$$X_{TCE} = \left(\frac{|\partial RMSE| \,/\, RMSE(a)}{|\Delta\theta \,/\, \theta|} \right) / X_{TCE}^{max} \quad (2\text{-}2)$$

where:

$$RMSE = \left[\frac{1}{N} \sum_{i=1}^{N} (sim_i - obs_i)^2 \right]^{1/2} \quad (2\text{-}3)$$

$$\partial RMSE = RMSE(\Delta\theta) - RMSE(\theta) \quad (2\text{-}4)$$

θ = base parameter; $\Delta\theta$ = perturbed parameter – θ; N = number of TCE effluent measurements. All sensitivity coefficients were normalized by maximum values (X_{TCE}^{max}) to provide a relative comparison metric of model sensitivities.

2.7.2.2. Sensitivities with respect to TOR

Provided with a cleanup concentration input, the VA model calculates the time required to reach the target value (e.g., contaminant MCL). Using the base parameter sets, which reflect detailed experimental conditions and initial source zone properties, TOR was calculated for both experiments by arbitrarily defining a target level for source discharge concentrations at C = 0.005 mg/L. Sensitivity coefficients normalized by maximum values (X_{TOR}^{max}) were calculated as:

$$X_{TOR} = \left(\frac{RMSE(\Delta\theta)}{|\Delta\theta \,/\, \theta|} \right) / X_{TOR}^{max} \quad (2\text{-}5)$$

2.7.3. Uncertainty Analysis

Source zone metrics controlling field-scale dissolution include DNAPL mass and distribution (Abriola et al., 2013). Uncertainties associated to both metrics can therefore propagate to model predictive uncertainties (Abriola, 2005; Tang, 2019). Prior (pre-history matching) parameter and predictive uncertainties can be informed by expert knowledge and/or by site characterization (e.g., DNAPL delineation, projected flow through area), whereas posterior (post-history matching)

uncertainties may be reduced and quantified through history-matching of monitoring data. Because volume-averaging eliminates spatial parameter correlations, the prior uncertainty of mass transfer parameters was expressed through statistically uncorrelated uncertainty bounds (archived data file). All initial (mean) parameter values were inherited from Stewart et al. (2021).

Uncertainty bounds of characteristic dimensions (V_a) and mass (m_a) of DNAPL accumulations were designed so that $1\% < S_a^N < 60\%$ and $\sum V_a < V_S$ in both experiments; where DNAPL saturation (S_a^N) of the pore space (ϕ) is also a function of DNAPL density (ρ_n) as indicated by Equation 2-6. Per sensitivity results, upscaling parameters (V_S, U_0, and ϕ) were assumed well constrained by the monitoring scale and removed from predictive uncertainty evaluations. Uncertainty analyses were focused on m_a, V_a, α_T, and γ pertaining to each DNAPL accumulation. Linear and nonlinear uncertainty quantification methods were implemented to understand drivers of model uncertainties and bias emerging from data-driven conceptual assumptions.

$$S_a^N = \frac{m_a}{V_a \phi \rho_n} \tag{2-6}$$

2.7.3.1. Linear Analysis Methods

Model linearization expressed in Equation 2-7 is the primary assumption in first-order second-moment (FOSM) analysis (Doherty, 2015). Equation 2-7 indicates that a vector of measurements of system state **h** equals the action of the model **Z** on a vector of parameters **k** plus a vector of measurement noise **ε**. Prior model uncertainty was expressed by Equation 2-8 assuming a multi-gaussian probability density function (PDF), defined by mean parameter values $\underline{\mathbf{k}}$ and a diagonal covariance matrix C(**k**). Likewise, FOSM analysis assumes a multi-gaussian PDF of **ε** (Equation 2-9), defined by mean values of zero and a diagonal covariance matrix C(**ε**). Jacobian matrices **Z** were weighted by the inverse of the standard deviation (σ) of **ε**. The misfit between simulated (Stewart et al., 2021) and measured TCE concentrations was used to define **ε**, where σ_ε^{-1} values were calculated with the PEST-based utility PWTADJ2 (Watermark Numerical Computing, 2018) as observations weights for FOSM analyses.

$$\mathbf{h} = \mathbf{Zk} + \boldsymbol{\varepsilon} \quad (2\text{-}7)$$

$$\mathbf{k} \sim \mathrm{N}[\mathbf{k}, \mathrm{C}(\mathbf{k})] \quad (2\text{-}8)$$

$$\boldsymbol{\varepsilon} \sim \mathrm{N}[\mathbf{0}, \mathrm{C}(\boldsymbol{\varepsilon})] \quad (2\text{-}9)$$

$$s = \mathbf{y}^{\mathrm{t}}\mathbf{k} \quad (2\text{-}10)$$

$$\sigma_s^2 = \mathbf{y}^{\mathrm{t}}\mathrm{C}(\mathbf{k})\mathbf{y} \quad (2\text{-}11)$$

$$\mathrm{C}'(\mathbf{k}) = \mathrm{C}(\mathbf{k}) - \mathrm{C}(\mathbf{k})\boldsymbol{Z}^{\mathrm{t}}[\mathbf{Z}\mathrm{C}(\mathbf{k})\boldsymbol{Z}^{\mathrm{t}} + \mathrm{C}(\boldsymbol{\varepsilon})]^{-1}\mathbf{Z}\mathrm{C}(\mathbf{k}) \quad (2\text{-}12)$$

$$\sigma_s'^2 = \mathbf{y}^{\mathrm{t}}\mathrm{C}'(\mathbf{k})\mathbf{y} \quad (2\text{-}13)$$

Linearization of a model prediction *s* (Equation 2-10) depends on a vector of sensitivities of *s* (TOR) with respect to **k**, where the prior variance of *s* (Equation 2-11) is obtained through covariance propagation (Doherty, 2015). The posterior parameter covariance matrix (Equation 2-12), obtained by history-matching conditioning, was used to estimate posterior TOR uncertainty variance (Equation 2-13). All parameters were log-transformed to reduce their nonlinearity with respect to model outputs. Linear analyses were performed with the utility programs GENLINPRED and PREDUNC (Watermark Numerical Computing, 2018) to understand how TCE monitoring profiles constrain source zone properties, and thereby, TOR uncertainties.

2.7.3.1.1. Relative parameter uncertainty variance (RUVR) reduction

This statistical metric was used to evaluate the ability of dissolved TCE concentrations to reduce the prior uncertainty variance (σ_i^2) of each parameter (*i*) encapsulated in C(**k**). Equation 2-14 defines this metric upon extracting posterior parameter uncertainty variances (σ'^2_i) from C'(**k**) as:

$$RUVR_i = 1 - \frac{\sigma_i'^2}{\sigma_i^2} \quad (2\text{-}14)$$

2.7.3.1.2. Prior and posterior parameter contributions to predictive uncertainty

The contribution of an individual parameter to the uncertainty of a prediction is defined as the fall of predictive uncertainty resulting from acquiring perfect knowledge of the parameter (Doherty, 2015). Hence, individual parameters were systematically removed from FOSM calculations to investigate their relative contributions to TOR uncertainty. Because history-matching information may be shared between several model parameters, the posterior contribution of a parameter could increase in relation to its prior contribution, indicating a correlation with another parameter (Doherty, 2015). While sensitivity analyses were useful to examine relative model error incurred by perturbing individual parameters, considering parameter correlations for TOR uncertainty estimation allowed assessing the worth of HRSC over history-matching for constraining the models.

2.7.3.1.3. Data-Worth Analysis

The ability of spatial or temporal data to reduce the uncertainty of model predictions defines its worth (Doherty & Moore, 2020; Finsterle, 2005). The worth of individual measurements of TCE concentrations was quantified to understand how monitoring profiles reduce TOR uncertainty. Data-worth analyses were also tied to parameter RUVR, further elucidating upon the additional benefit of HRSC for constraining remaining model uncertainties.

2.7.3.2. Nonlinear Analysis Methods

Posterior TOR uncertainties were quantified using the iterative ensemble smoother PESTPP-iES (White et al., 2020). Multi-gaussian prior parameter PDFs were defined by uncertainty bounds spanning $\pm 2\sigma$ from initial (mean = μ) values, representing 95% confidence intervals. PESTPP-iES undertakes Monte-Carlo sampling of parameter uncertainty bounds generating model realizations (ensembles) which are upgraded with the Gauss-Levenberg-Marquardt (GLM) optimization algorithm. Rather than simply fitting simulation results to data, PESTPP-iES can generate observation ensembles considering multi-gaussian PDFs of $\boldsymbol{\varepsilon}$ (White, 2018). Here, all experimental TCE concentrations were assigned an observation weight value of 1 with $\sigma_{\varepsilon} = 10$

mg/L, to simultaneously estimate model parameters and quantify the nonlinear uncertainty of TOR in a stochastic manner. This approach was implemented to evaluate TOR uncertainties and bias arising from source zone conceptual assumptions driven by data availability.

In practice, HRSC data may help constrain source zone architecture, and thereby model conceptualizations. However, high predictive uncertainties may remain because of the inability to directly measure DNAPL mass and S_a^N. The benefit of data assimilation for constraining model uncertainties was investigated by estimating m_a, V_a, $\alpha_{T,a}$, and γ^a parameters in both experiments from partial and complete monitoring profiles. The resulting source dissipation timeframes were referred to as Posterior A (~13 days of monitoring), Posterior B (20 days) and Posterior All (26 days). Additionally, the heterogeneous experiment was conceptualized with 2 (2M), 3 (3M) and 4 (4M) DNAPL accumulations to examine TOR uncertainty and bias induced by history-matching of the entire TCE monitoring profile. The 2M model included "mass 1" and lumped "mass 2" and "mass 3" into a single accumulation (2M-3) based on the two release points, while the 3M model included those 3 distinct DNAPL accumulations. The 4M model subdivided "mass 1" into 1A and 1B (Figure 2-2b). Except for the 2M Model, the 3M and 4M models included an enhanced dissolution parameter to represent flow channelization through the coarse lens in which "mass 3" was embedded. Following a variability range reported in the literature (Klenk & Grathwohl, 2002), the prior uncertainty bounds of α_T parameters were defined as $5e^{-4} < \alpha_T$ (m) $< 2e^{-3}$ in both experiments, except for 0 ($1e^{-15}$) $< \alpha_{T,3}$ (m) < 0.002 in the coarse sand lens of the heterogeneous experiment, where $\alpha_{T,3} = 0$ m provided the best match to measured TCE concentrations (Stewart et al., 2021).

2.8. Results and Discussion

2.8.1. Sensitivity Analysis

As shown in Figures 2-3 and 2-4, the greatest model sensitivities with respect to matching TCE concentrations (X_{TCE}) corresponded to the source zone area (Z_S and Y_S) orthogonal to the flow direction and groundwater velocity (U_0). The former accounts for any dilution in the monitoring scale, while the latter had a prominent impact on TOR in both experiments. The role of V_S and U_0

on scaling mass transfer processes emphasized the need to constrain them by the monitoring scale to avoid model errors induced by data assimilation. Figure 2-3 also indicated that the projected area facing flow (YZ_g) of the ganglia-dominated accumulation, rather than γ^g or ganglia mass, was responsible for peak aqueous-phase concentrations. Similarly, Figure 2-4 shows the projected area YZ_{1A} of the most upgradient, low-saturation accumulation 1A in a high-ranked position. These X_{TCE} results suggested that S_a^N parameters (V_a and *Mass*) of ganglia-dominated accumulations responsible for peak concentrations do not impact TOR when a pool-dominated accumulation is also present; yet their estimation via history-matching may be valuable for remedial designs. Conversely, sensitivity with respect to TOR (X_{TOR}) was dominated by DNAPL pool saturation (S_p^N) parameters, transverse dispersivity ($\alpha_{T,p}$), and depletion exponent (γ^p). The negligible X_{TCE} values of pool parameters suggested difficulty in estimating them from monitoring data alone and value in HRSC for refining characteristic parameters of the pool.

In contrast to negligible X_{TCE} values by pool parameters in the mixed experiment (Figure 2-3), X_{TCE} rankings of S_3^N parameters in the heterogeneous experiment (Figure 2-4) suggested that high-saturation DNAPL accumulations may not exclusively reflect pool fractions of source zones. Typically, the small cross-sectional areas available for dissolution by groundwater flow through DNAPL pools reduces their relative contribution to mass flux, compared to ganglia-dominated accumulations. However, as indicated in Figure 2-4, the morphology of DNAPL accumulation 3, controlled by flow-field heterogeneity, influenced both X_{TCE} and X_{TOR} rankings in the heterogeneous experiment. The predictive advantage of generalizing mass transfer processes irrespective of S_a^N (Equation 2-1) over upscaled models predicated on the GTP mass ratio, was further evidenced by a similar effect on X_{TCE} and X_{TOR} incurred by perturbing $\alpha_{T,3}$ (Figure 2-4). Conversely, the variability of other α_T parameters in both experiments only influenced X_{TOR}.

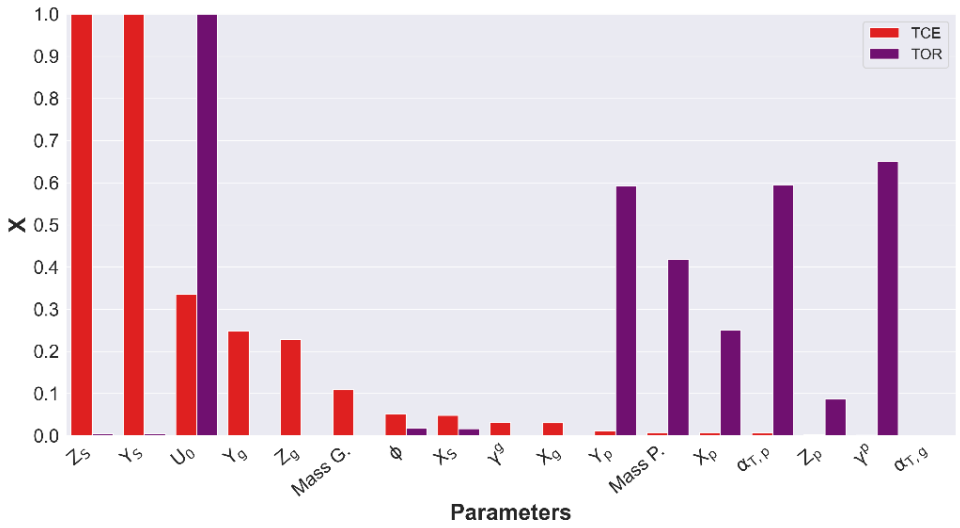

Figure 2-3. Sensitivity coefficients with respect to source discharge concentrations measured in the "mixed architecture" experiment and with respect to the simulated TOR.

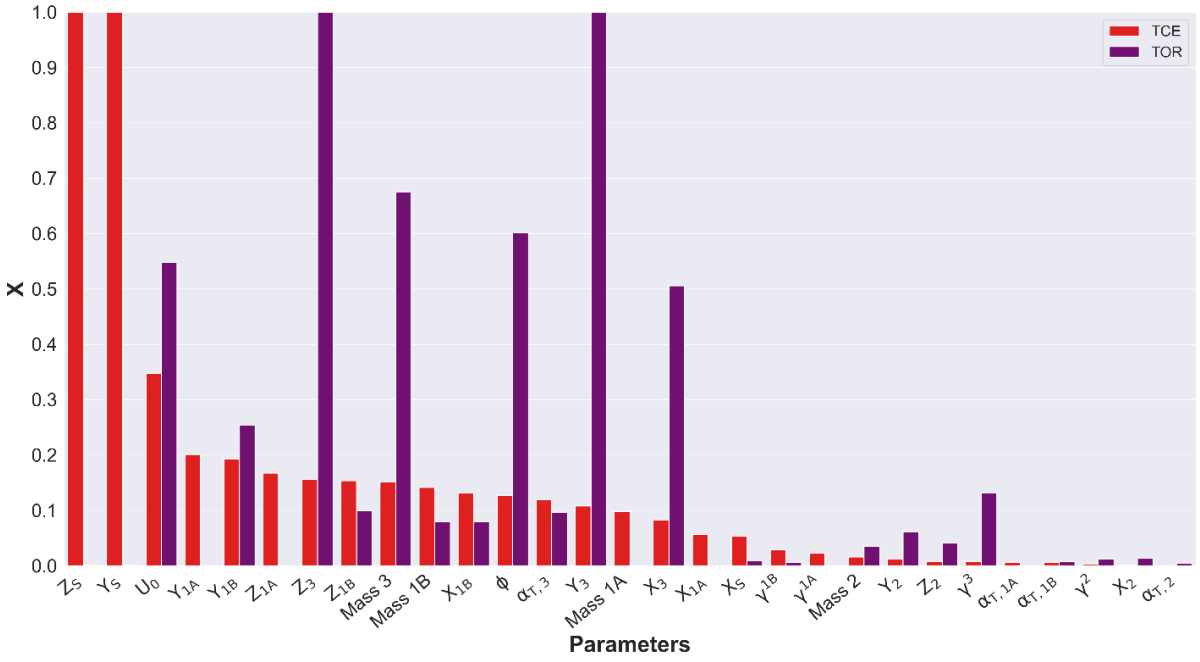

Figure 2-4. Sensitivity coefficients with respect to source discharge concentrations measured in the "heterogeneous architecture" experiment and with respect to the simulated TOR.

2.8.2. Linear Analysis

Prior (σ_{TOR}) and posterior (σ'_{TOR}) standard deviations of TOR uncertainty estimated with FOSM analysis and mean (μ_{TOR}) values for both experiments are presented in Table 2-2. Results shown were calculated using the complete TCE monitoring profiles. As indicated, history-matching significantly constrained prior TOR uncertainties despite low X_{TCE} values of TOR-sensitive parameters pertaining to high-S_a^N accumulations.

Table 2-2. Predictive uncertainty of mixed and heterogeneous experiments.

Experiment	μ_{TOR} (days)	σ_{TOR} (days)	σ'_{TOR} (days)
Mixed	27.9	19.8	8.6
Heterogeneous	28.6	20.5	1.7

2.8.2.1. Relative Parameter Uncertainty Variance Reduction

Figures 2-5 and 2-6 show the benefit of history-matching for reducing prior parameter uncertainties. Despite negligible X_{TCE} values corresponding to the pool mass and $\alpha_{T,p}$ of the mixed experiment (Figure 2-3), history-matching reduced the prior uncertainty of these parameters by ~70% and ~60%, respectively (Figure 2-5). The low uncertainty reduction of γ^p (Figure 2-5), to which TOR was sensitive (Figure 2-3), demonstrated the benefit of coupling upscaled modeling with stochastic analysis tools for predicting DNAPL longevity timeframes when mass transfer parameters remain unconstrained. In turn, sensitivity and FOSM analyses of the mixed experiment coincided in a low-ranked $\alpha_{T,g}$, suggesting that its prior (default) value of 0.001 m is reasonable for simulating dissolution of ganglia-dominated accumulations.

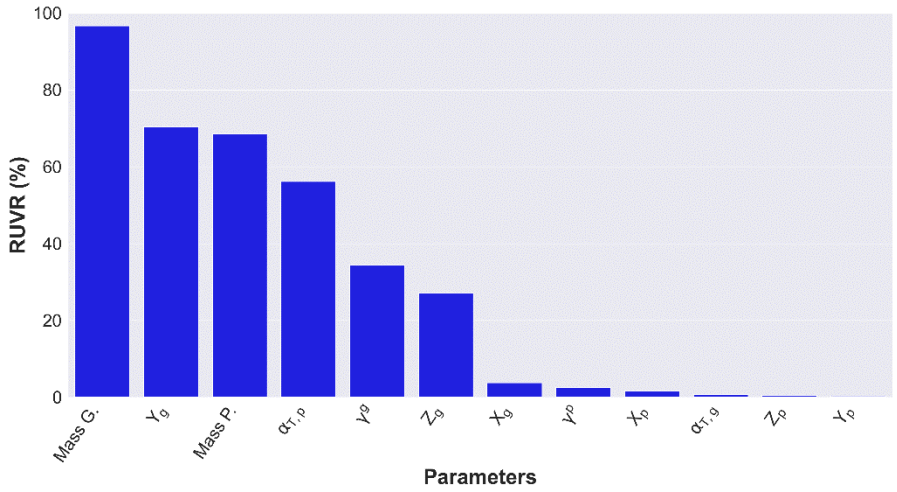

Figure 2-5. Relative uncertainty variance reduction of VA model parameters of mixed experiment.

Difficulties in reducing prior uncertainty of the γ parameters in the heterogeneous experiment are reflected in Figure 2-6. Yet the prior uncertainty of $S_a{}^N$ parameters of DNAPL accumulations 1A ($S_{1A}{}^N$), 1B ($S_{1B}{}^N$), and 3 ($S_3{}^N$) was reduced by approximately more than 50%. The higher RUVR of $S_3{}^N$ with respect to other $S_a{}^N$ parameters was attributed to the sequential dissolution of upgradient DNAPL masses, allowing the tailing segment of the TCE monitoring profile to constrain the remaining source architecture ($S_3{}^N$). These results implied that modeling efforts supporting the characterization of sites with aged, pool-dominated source zones, may benefit from history-matching of monitoring profiles. However, situations with scarce monitoring data and significant uncertainties on $S_a{}^N$ distributions along groundwater flow paths may warrant HRSC efforts. In turn, source characterization data such as DyeLIF and Hydraulic Profiling Tool (HPT) (Horst et al., 2018) can be leveraged for VA model parameterization, while FOSM analyses can help guide additional data collection efforts to constrain DNAPL dissolution trends.

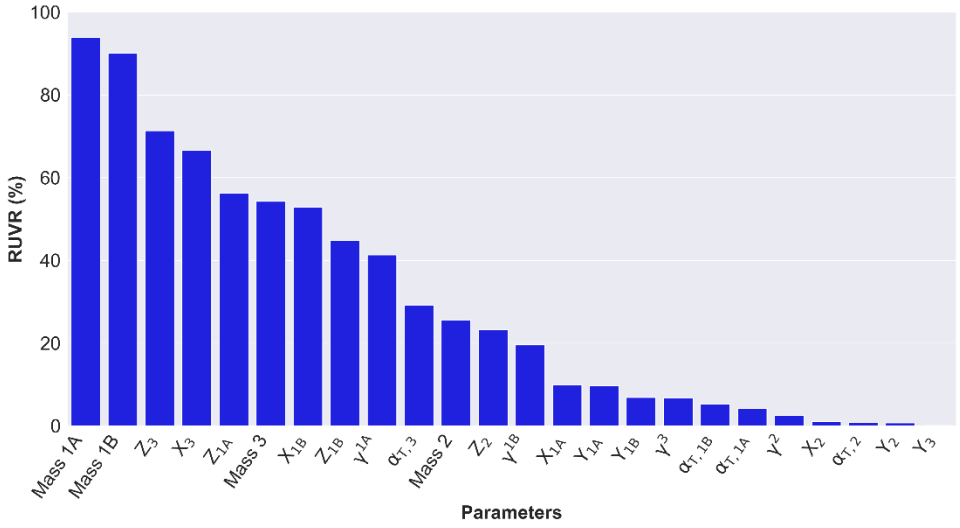

Figure 2-6. Relative uncertainty variance reduction of VA model parameters of heterogeneous experiment.

2.8.2.2. Prior and posterior parameter contributions to predictive uncertainty

As shown in Figure 2-7, FOSM analyses validated negligible X_{TOR} values caused by the ganglia parameters in the mixed experiment. Although the pool dispersive area (YX_p) and γ^p influenced X_{TOR} results (Figure 2-3), prior and posterior TOR uncertainties of the mixed experiment were clearly driven by the pool mass and $\alpha_{T,p}$ (Figure 2-7). Likewise, Figure 2-8 indicated that the primary drivers of prior TOR uncertainty in the heterogenous experiment were S_3^N, $\alpha_{T,3}$, and γ^3. Repeating FOSM calculations with uncertainty bounds defined as $0 < \alpha_T$ (m) < 0.01 for all DNAPL accumulations in the heterogeneous experiment did not alter the uncertainty rankings shown in Figure 2-8. Results of both experiments supported the significance of dispersive mass transfer (α_T) from high-saturation DNAPL accumulations in regulating TOR. However, the accurate replication of the heterogenous source dissolution trend with $\alpha_{T,3} = 0$ m was attributed to the contrast in grain sizes, limiting dispersion from the coarse-grained lenticular zone into the finer surrounding sands despite high $S_{3,0}^N$ values.

Unlike the empirical mass depletion exponent γ^3, α_T may be directly measured at contaminated sites to directly constrain mass transfer uncertainties. Examples of field methods include push-pull tracer tests, borehole and HPT logging, and discrete groundwater sampling with direct push technology (DPT). These data may be interpreted with 2D analytical modeling (Huang et al., 2010), grain-size correlations with soil hydraulic conductivity and α_T (Carey et al., 2018), and

spatial moment analysis (Rockhold et al., 2016), respectively. Nonetheless, the α_T component of DNAPL dissolution expressed in Equation 2-1 should not be confused with plume-scale macrodispersion. While dispersivity at the source-zone and plume scales is driven by mechanical or hydrodynamic mixing along tortuous flow paths (Molz, 2015), coupling a VA model of DNAPL dissolution with a downgradient contaminant plume model may require two different α_T values based upon site-specific conditions. Several studies have demonstrated the relationship between soil grain size and α_T (Carey et al., 2018), concurring with its role on DNAPL mass transfer (Figures 2-7 and 2-8). This is in contrast to Gilland-Sherwood mass transfer correlations which rely upon aqueous-phase transport models for the contribution of α_T to DNAPL dissolution (Yang et al., 2019).

As indicated in Figure 2-8, the primary driver of posterior TOR uncertainty, γ^3, reflected its role in regulating source discharge concentrations over several orders of magnitude. While a lack of extensive groundwater monitoring at contaminated sites could limit γ constraining via history-matching, $S_a{}^N$ and flow-field heterogeneities may also pose additional uncertainties on mass transfer assumptions. In this case, TCE dissolution tailing, primarily regulated by $S_3{}^N$, was also modulated by flow channelization in the coarse sand lens (Figure 2-2b). Transient reductions in DNAPL interfacial areas, which limit mass transfer rates through the γ parameter, were obfuscated by a local increase in U_0 and k_r in the heterogeneous experiment (Stewart et al., 2021). Although the level of characterization detail available for the flow-cell experiment would not be available at field sites, VA modeling provides an efficient means to evaluate conceptual assumptions of system heterogeneities and quantify mass transfer uncertainties. The prior uncertainty rankings of $S_{1B}{}^N$ and $S_3{}^N$ parameters (Figure 2-8) emphasized the level of effort for DNAPL delineation required for adequate model parameterization.

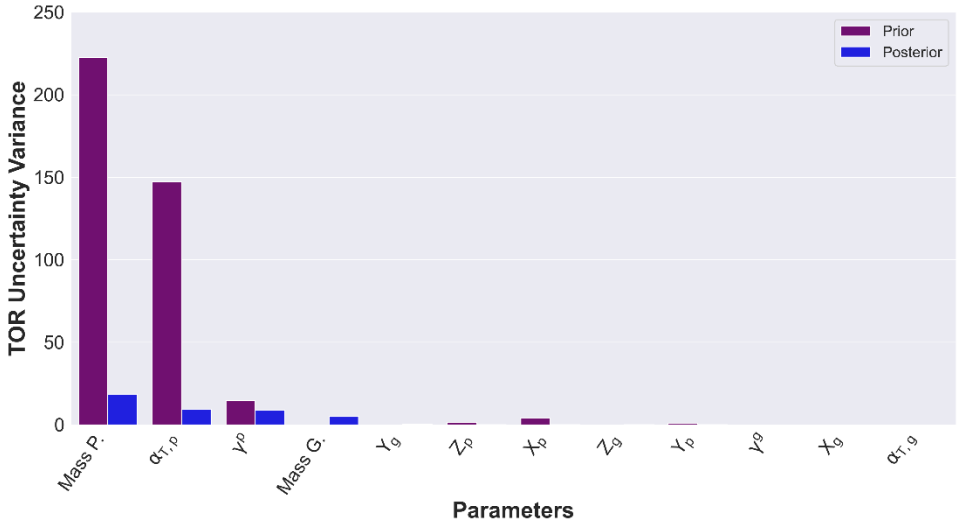

Figure 2-7. Prior and posterior parameter contributions to TOR uncertainty in the mixed experiment.

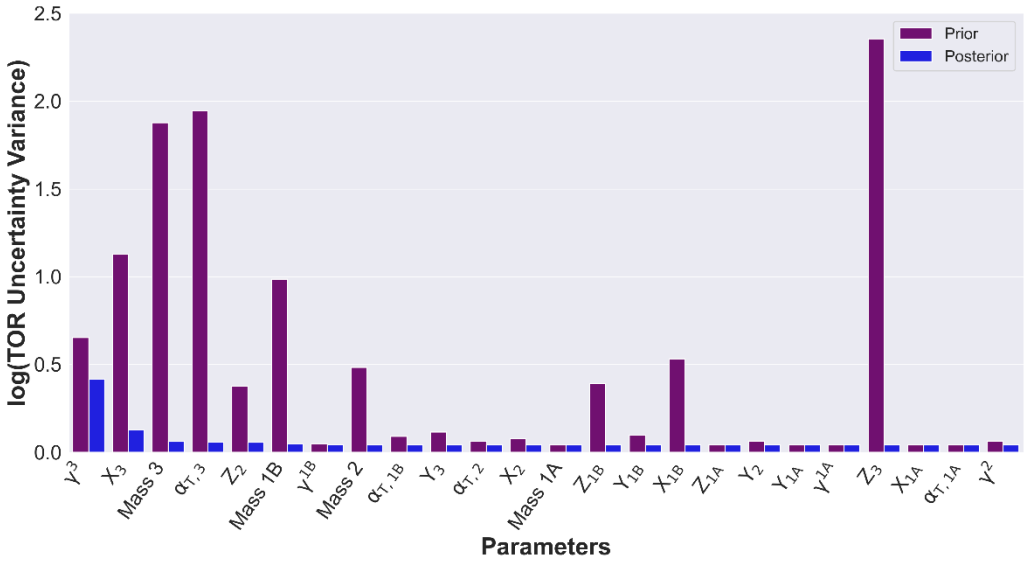

Figure 2-8. Prior and posterior parameter contributions to TOR uncertainty of heterogeneous experiment.

2.8.2.3. Data-Worth Analysis

The worth of TCE monitoring profiles of the mixed and heterogeneous experiments is shown in Figures 2-9 and 2-10, respectively. Both figures express data worth on the Y-axis as a percent reduction and increase of σ_{TOR} and σ'_{TOR} (see Table 2-2), respectively, by individual monitoring measurements. Figures 2-9a and 2-10a indicate the worth of individual measurements for constraining prior TOR uncertainty (σ_{TOR}), whereas Figures 2-9b and 2-10b depict increases in

posterior (constrained) TOR uncertainty (σ'_{TOR}) caused by data removal. As shown in Figure 2-10, a tendency of increasing data worth in the mixed experiment started at point C, when the pool mass transfer area ($A_{p,xy}$) was sufficiently reduced to onset dissolution tailing. Similar prior and posterior data-worth trends in the mixed experiment suggested that peak concentrations emanating from ganglia-dominated accumulations do not constrain TOR. In turn, the RUVR of pool mass (~70%) and $\alpha_{T,p}$ (~60%) controlling TOR uncertainty was attributed to TCE monitoring after point C (Figure 2-9), highlighting the benefit of history-matching for characterizing sites with aged source zones and simple architectures. In these experiments, point C represents a rough mid-point for the DNAPL TOR despite an 80% reduction in the total DNAPL mass.

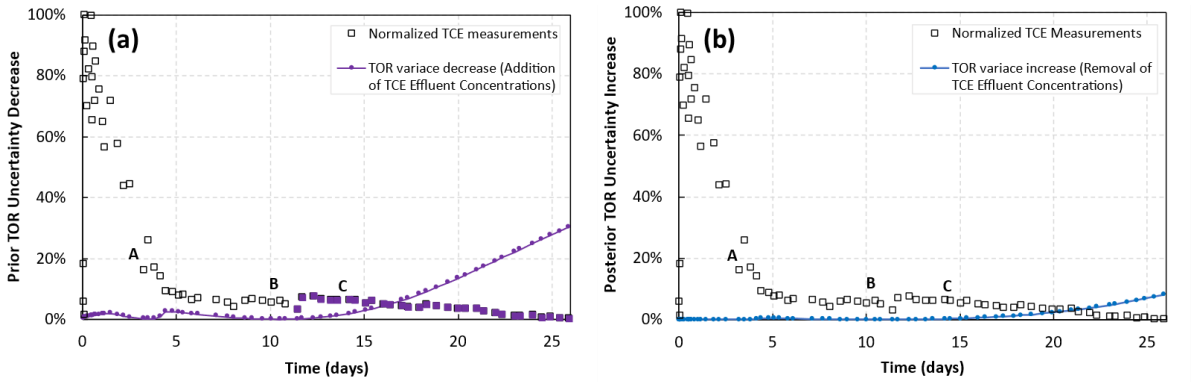

Figure 2-9. Worth of monitoring data for constraining TOR uncertainty of the mixed experiment shown in Figure 2-2a: a) Decrease in prior uncertainty with addition of individual TCE concentrations. The filled data points highlight the greatest information content for reducing prior TOR uncertainty. b) Increases in posterior uncertainty with data removal. Points A, B, C show DNAPL depletion images measured by DiFilippo et al. (2010).

Figure 2-10a shows the worth of breakthrough inflection points along the TCE monitoring curve of the heterogeneous experiment for constraining σ_{TOR}. The first peak in the σ_{TOR} decrease curve coincided with point A, indicating the onset of rapid dissolution of DNAPL mass accumulation 1b after mass 1a was completely dissolved. The second peak of σ_{TOR} reduction occurred during a slight increase in TCE concentrations, reflecting an increased k_r through mass 2 after mass 1B was dissolved. The final peaks of σ_{TOR} reduction (Figure 2-10a) and σ'_{TOR} increase (Figure 2-10b) coincided with the final stage of DNAPL dissolution associated to mass 3. These results highlighted disadvantages of predicting future system behavior from limited monitoring profiles, corresponding to situations where remaining source architectures and heterogeneities have not yet been reflected in historical dissolution trends.

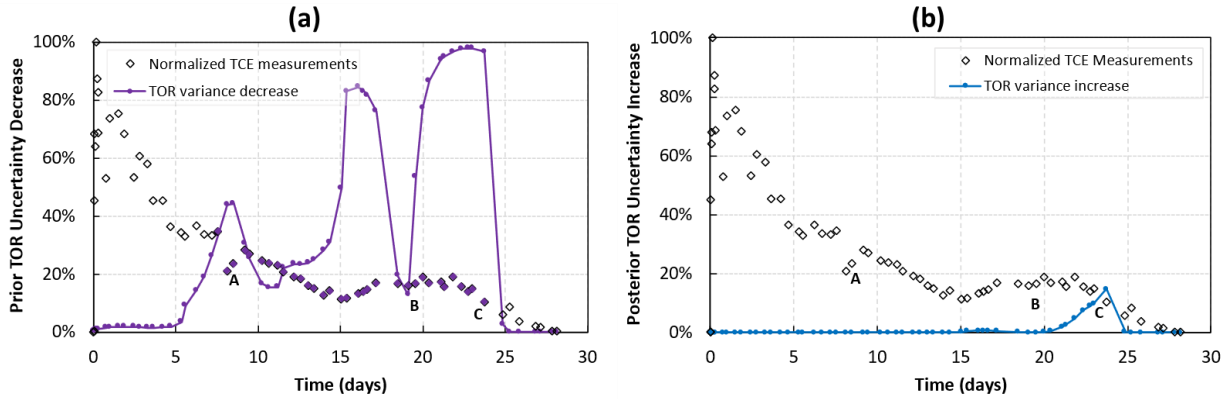

Figure 2-10. Worth of TCE dissolution measurements for reducing TOR uncertainty of the heterogeneous experiment shown in Figure 2-2b: a) Decrease in prior uncertainty with addition of individual history-matching constraints. The filled data points highlight the greatest information content for reducing prior TOR uncertainty. b) Increases in posterior uncertainty with data loss. Points A, B, C show the DNAPL depletion measured by DiFilippo et al. (2010).

2.8.3. Nonlinear Uncertainty Analysis

Figure 2-11 indicates that all prior and posterior source dissipation timeframes of the mixed experiment included the "true TOR" (μ_{TOR} = 27.9 days). All posterior analyses underestimated the initial DNAPL mass in the mixed experiment by ~11%, yet the known value of 17.2 g was included within 95% confidence limits (results not shown). The average estimated S_g^N and S_p^N values were 4% and 40%, respectively, consistent with initial experimental conditions (Figure 2-2a). Prior and posterior TOR uncertainties in Figure 2-11 demonstrated the utility of VA modeling for estimating unbiased depletion timeframes a priori, by leveraging DNAPL-delineation or limited monitoring data pertaining to source zones with relatively simple architectures and flow conditions.

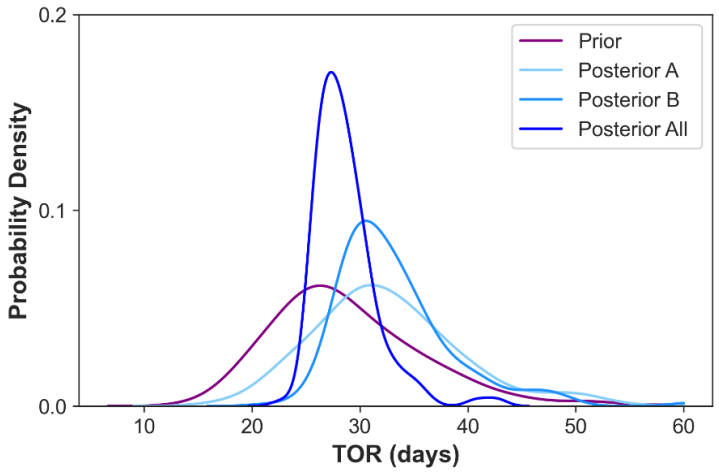

Figure 2-11. Prior and posterior TOR PDFs of mixed experiment. Posterior A and B were estimated by history-matching TCE concentrations through day 11.7 and 20 (Figure 2-10), respectively.

The stochastic optimization of the heterogeneous experiment models underestimated initial DNAPL mass by ~7%, with 95% confidence limits encompassing the injected amount of 20.4 g (results not shown). As illustrated in Figure 2-12, posterior S_a^N uncertainties reflected the averaging by model resolutions required to history-match the complete TCE dissolution profile and quantify TOR uncertainty (Figure 2-13). Figure 2-13 shows all posterior TOR PDFs encompassing the "true" TOR of 28.6 days, emphasizing the worth of final DNAPL dissolution stages for constraining TOR with various model resolutions. However, the 2M and 3M models required removing peak TCE concentrations from day 0 through day 9 (Figure 2-14). Not doing so did not impact the accuracy of estimated DNAPL mass, but resulted in an artificially low initial S_1^N of lumped mass 1 from inadequate parameterization complexity (results not shown). Sufficient source architecture parameters are thereby necessary to assimilate complex dissolution profiles to avoid misleading injection-based remedial designs.

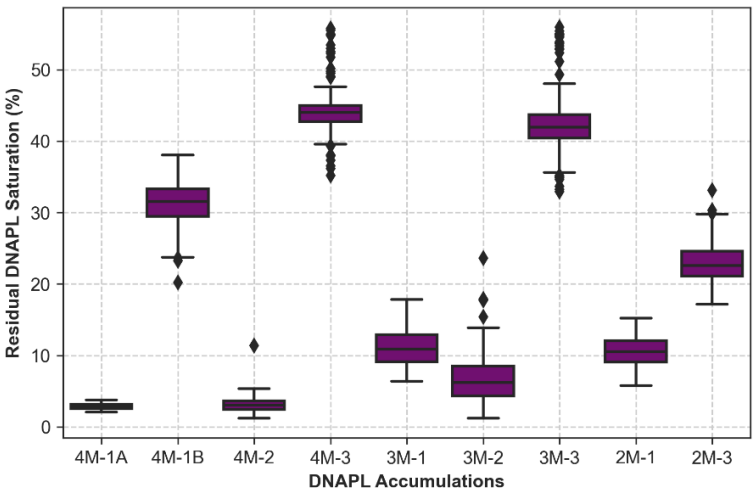

Figure 2-12. Posterior DNAPL saturation distributions of each DNAPL accumulation in the 4M, 3M, and 2M VA models of the heterogeneous experiment.

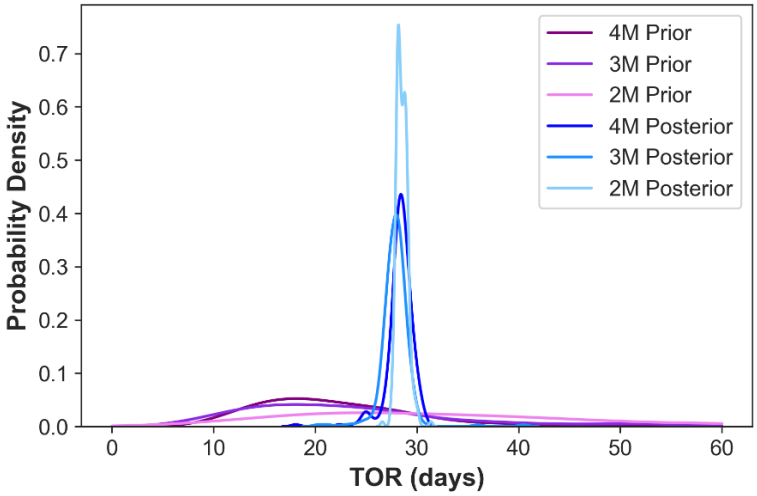

Figure 2-13. Prior and posterior TOR PDFs of the heterogeneous experiment conceptualized by 2, 3, and 4 DNAPL accumulations.

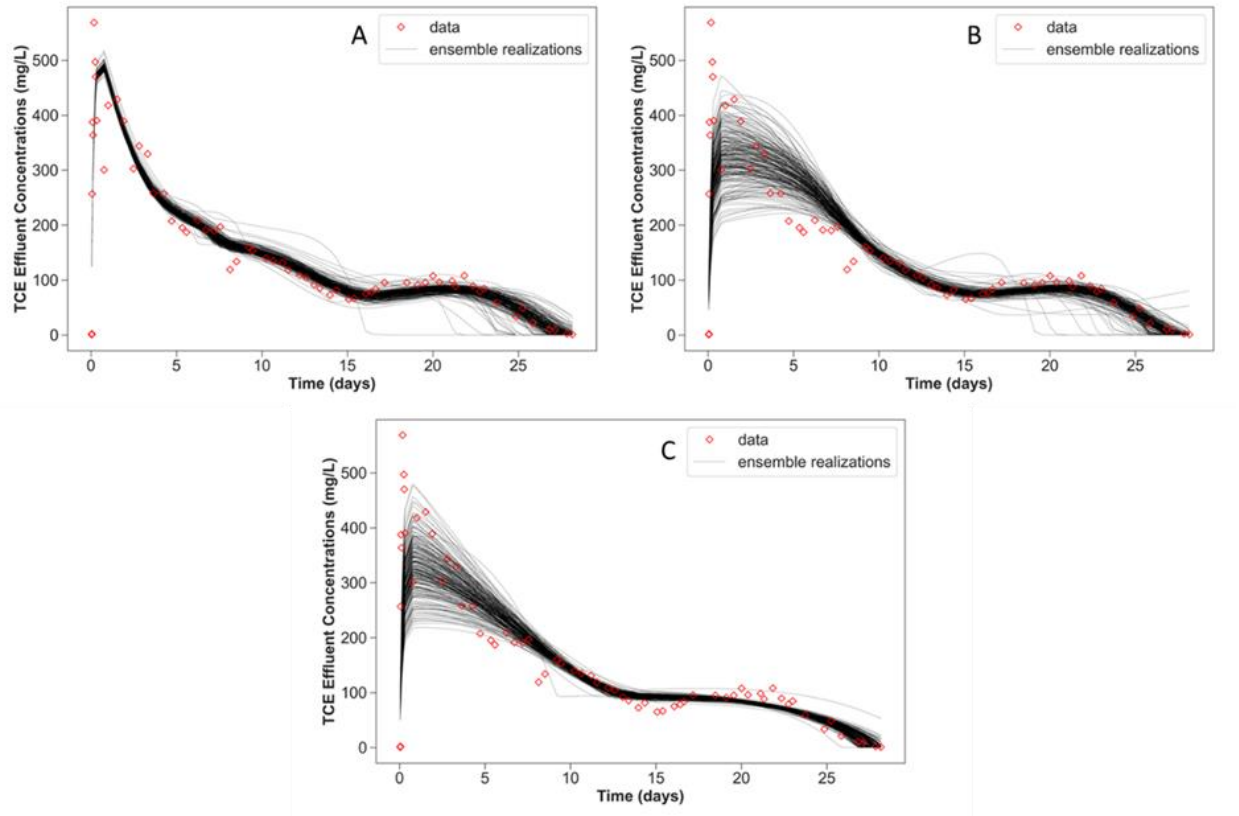

Figure 2-14. Posterior model ensembles of the heterogeneous experiment corresponding to (A) 4, (B) 3, and (C) 2 DNAPL accumulations.

Figure 2-15 shows prior predictive PDFs approximated with S_a^N constraints assuming availability of HRSC data to inform model parameters. The prior S_a^N constraints for this analysis correspond Figure 2-12. Despite low probability densities, all prior PDFs encompassed the μ_{TOR} = 28.6 days, suggesting that even a low-resolution model (2M) accounting for S_a^N distributions along the flow path can predict unbiased source dissipation timeframes. However, Figure 2-15 depicts biased posterior 2M PDFs tending to exclude μ_{TOR} resulting from monitoring data assimilation with inadequate parameterization complexity. Unlike 2M, 3M included an adjustable "dissolution enhancement factor" representing increased velocity through the coarse lens. Omitting that parameter from the 3M model (fixing it at a value of 1) did not impact σ'_{TOR} estimated from the entire TCE profile (Figures 2-14 and 2-15). However, σ_{TOR} and σ'_{TOR} estimated from partial TCE profiles were also overestimated (excluding μ_{TOR}) and the nonmonotonic increase in TCE concentrations from day 15 through day 20 could not be reproduced (results not shown). Hence, the unbiased Posterior A and B results of the 3M model, shown in Figure 2-15, suggested that in

addition to adequate representation of DNAPL distribution along the local flow path, parameterization of flow field heterogeneity is also necessary to avoid biasing model estimates through history-matching of multistage and nonmonotonic dissolution profiles.

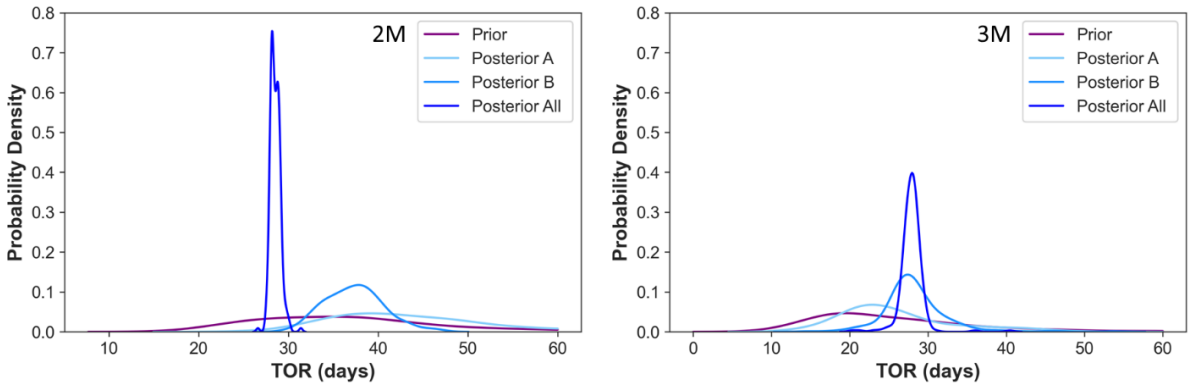

Figure 2-15. Probability density functions of TOR approximated with 2M and 3M models of heterogeneous experiment. Posterior A and B PDFs were estimated from partial TCE monitoring profiles through day 14 and 20, respectively.

2.9. Conclusions

This work demonstrated a practical approach for estimating DNAPL dissolution timeframes coupling upscaled modeling with uncertainty analysis methods. Assimilation of monitoring data may induce model predictive bias without sufficient parameterization complexity representing the DNAPL source, including sequential dissolution of DNAPL accumulations distributed along the flow path. In both experiments, saturation parameters and transverse dispersion of pool-dominated DNAPL accumulations controlled the source zone longevity, and were constrained by tailing of final dissolution stages despite their negligible sensitivity with respect to measured effluent concentrations. Because the VA model provides TOR as a direct output, FOSM analyses can be used to guide site characterization efforts to constrain prior, or remaining posterior parameter uncertainties responsible for predictive TOR and mass discharge/flux uncertainties. As demonstrated with the heterogeneous source zone experiment, field mapping of aquifer hydraulics, and/or estimation of source zone architecture using physically-based inversion methods can be leveraged to refine site conceptual assumptions encapsulated in VA model parameters. This includes direct constraining of transverse vertical dispersivity at the source zone scale, regardless

of DNAPL saturation, differentiating its contribution to DNAPL dissolution from macrodispersion at the contaminant plume scale.

Local groundwater velocity and source zone dimensions had a prominent impact on mass discharge and DNAPL persistence because of their scaling role on mass transfer processes. Hence, these parameters require constraining by monitoring and site characterization scales, promoting adequate dilution and flow bypassing effects on DNAPL dissolution. Conversely, saturation parameters of ganglia-dominated DNAPL accumulations, which may not be directly measured at field sites, did not impact source longevity timeframes when pools were present. Yet their influence on peak discharge concentrations justifies their parameterization to avoid erroneous estimates of DNAPL saturation distributions and mass discharge rates. Although accurately simulating mass discharge was possible with increased resolution of source zone architecture, exclusive designations of ganglia and pool fractions of DNAPL may be inadequate for mass transfer modeling. The high-saturation DNAPL accumulation embedded in the coarse sand lens of the heterogeneous experiment, controlled the source zone longevity without dispersive mass transfer. Moreover, lumping the downgradient saturations and ignoring flow field heterogeneity, biased lifespan estimates of the heterogenous source zone and degraded the replication of nonmonotonic DNAPL dissolution tailing. While this level of characterization detail may not be available for contaminated sites, upscaled modeling and stochastic uncertainty analyses of site conceptual assumptions can support risk-based decision making through data assimilation and predictive hypothesis testing with a physical mass transfer basis.

2.10. Acknowledgements

This study was supported by the Environmental Security Technology Certification Program (ESTCP) under Project ER19-5223. The content of this manuscript has not been subject to agency review and does not necessarily represent the view of the sponsoring agency.

2.11. Data Availability Statement

A copy of the VA model executable and input instructions can be requested from Praxis Environmental Tech., Inc. at https://www.praxis-enviro.com/contact. The SENSAN, PWTADJ2, PREDUNC, GENLINPRED, and PEST software utilities used for sensitivity and linear uncertainty analyses are available at https://pesthomepage.org/programs. The PESTPP-iES software used for ensemble-based parameter estimation and nonlinear uncertainty analyses is available at https://www.usgs.gov/software/pest-software-suite-parameter-estimation-uncertainty-analysis-management-optimization-and (version 5.1.6 was used and the source code is available on https://github.com/usgs/pestpp/releases/tag/5.1.6). Except for the data-worth results figures, figures in the results and discussion section were produced with the Matplotlib (https://matplotlib.org/) version 3.5.1 and Seaborn (https://seaborn.pydata.org/) version 0.11.2 libraries using the Python programming language. Data is supplied in an excel file for peer review purposes and will be archived in an online repository maintained by Virginia Tech with a unique DOI number.

References

Abriola, L. M. (2005). Guest Editorial: Contaminant Source Zones: Remediation or Perpetual Stewardship? Environmental Health Perspectives, 113(7), A438-A439. https://doi.org/10.1289/ehp.113-a438

Abriola, L. M., Miller, E. L., Pennell, K. D., Ramsburg, A., & Christ, J. A. (2013). Metric identification and protocol development for characterizing DNAPL source zone architecture and associated plume response. Alexandria, VA: SERDP Project ER-1612.

Agaoglu, B., Copty, N. K., Scheytt, T., & Hinkelmann, R. (2015). Interphase mass transfer between fluids in subsurface formations: A review. Advances in Water Resources, 79, 162-194. https://doi.org/10.1016/j.advwatres.2015.02.009

Arshadi, M., De Paolis Kaluza, M. C., Miller, E. L., & Abriola, L. M. (2020). Subsurface Source Zone Characterization and Uncertainty Quantification Using Discriminative Random Fields. Water Resources Research. https://doi.org/10.1029/2019WR026481

Carey, G. R., McBean, E. A., & Feenstra, S. (2018). Estimating transverse dispersivity based on hydraulic conductivity. Environmental Technology & Innovation, 10, 36-45. https://doi.org/10.1016/j.eti.2018.01.008

Christ, J. A., Ramsburg, A. C., Pennell, K. D., & Abriola, L. M. (2006). Estimating mass discharge from dense nonaqueous phase liquid source zones using upscaled mass transfer coefficients: An evaluation using multiphase numerical simulations. Water Resources Research, 42(11). https://doi.org/10.1029/2006WR004886

Christ, J. A., Ramsburg, C. A., Pennell, K. D., & Abriola, L. M. (2010). Predicting DNAPL mass discharge from pool-dominated source zones. Journal of Contaminant Hydrology, 114(1-4), 18 - 34. https://doi.org/10.1016/j.jconhyd.2010.02.005

Dekker, T. J., & Abriola, L. M. (2000). The influence of field-scale heterogeneity on the infiltration and entrapment of dense nonaqueous phase liquids in saturated formations. Journal of Contaminant Hydrology, 42(2-4), 187-218. https://doi.org/10.1016/S0169-7722(99)00092-3

DiFilippo, E. L., & Brusseau, M. L. (2008). Relationship Between Mass Flux Reduction and Source-Zone Mass Removal: Analysis of Field Data. Journal of Contaminant Hydrology, 98(1-2), 22-35. https://doi.org/10.1016/j.jconhyd.2008.02.004

DiFilippo, E. L., & Brusseau, M. L. (2011). Assessment of a Simple Function to Evaluate the Relationship Between Mass Flux Reduction and Mass Removal for Organic-Liquid Contaminated Source Zones. Journal of Contaminant Hydrology, 123(3-4), 104-113. https://doi.org/10.1016/j.jconhyd.2010.12.011

DiFilippo, E. L., Carroll, K. C., & Brusseau, M. (2010). Impact of organic-liquid distribution and flow heterogeneity on reductions in mass flux. Journal of Contaminant Hydrology, 115(1-4), 14-25. https://doi.org/10.1016/j.jconhyd.2010.03.002

Doherty, J. (2015). Calibration and Uncertainty Analysis for Complex Environmental Models. Brisbane, Australia: Watermark Numerical Computing.

Doherty, J., & Moore, C. (2020). Decision Support Modeling: Data Assimilation, Uncertainty Quantification, and Strategic Abstraction. Groundwater, 58(3), 327-337. https://doi.org/10.1111/gwat.12969

Eniarson, M., Fure, A., St. Germain, R., Chapman, S., & Parker, B. (2018). DyeLIF™: A New Direct-Push Laser-Induced Fluorescence Sensor System for Chlorinated Solvent DNAPL and Other Non-Naturally Fluorescing NAPLs. Groundwater Monitoring & Remediation, 28-42. https://doi.org/10.1111/gwmr.12296

Falta, R. (2003). Modeling sub-grid-block-scale dense nonaqueous phase liquid (DNAPL) pool dissolution using a dual-domain approach. Water Resources Research, 39(12). https://doi.org/10.1029/2003WR002351

Finsterle, S. (2015). Practical notes on local data-worth analysis. Water Resources Research. https://doi.org/10.1002/2015WR017445

Frind, E. O., Molson, J. W., & Schirmer, M. (1999). Dissolution and mass transfer of multiple organics under field conditions: The Borden emplaced source. Water Resources Research, 35(3), 683-694. https://doi.org/10.1029/1998WR900064

Guo, Z., Russo, A. E., DiFilippo, E. L., Zhang, Z., Zheng, C., & Brusseau, M. L. (2020). Mathematical modeling of organic liquid dissolution in heterogeneous source zones. Journal of Contaminant Hydrology, 235. https://doi.org/10.1016/j.jconhyd.2020.103716

Horst, J., Welty, N., Stuetzle, R., Wenzel, R., & Germain, R. (2018). Fluorescent dyes: A new weapon for conquering DNAPL characterization. Groundwater Monitoring & Remediation, 38(1), 19-25. https://doi.org/10.1111/gwmr.12261

Huang, J., Christ, J. A., & Goltz, M. N. (2010). Analytical solutions for efficient interpretation of single-well push-pull tracer tests. Water Resources Research. https://doi.org/10.1029/2008WR007647

ITRC (Interstate Technology & Regulatory Council). (2010). Use and Measurement of Mass Flux and Mass Discharge. Washington, D.C.: Interstate Technology & Regulatory Council, Integrated DNAPL Site Strategy Team. Retrieved from www.itrcweb.org

Kang, X., Kokkinaki, A., Kitandis, P. K., Shi, X., Lee, J., Mo, S., & Wu, J. (2021a). Hydrogeophysical Characterization of Nonstationary DNAPL Source Zones by Integrating a Convolutional Variational Autoencoder and Ensemble Smoother. Water Resources Research, 57(1). https://doi.org/10.1029/2020WR028538

Kang, X., Kokkinaki, A., Power, C., Kitandis, P. K., Shi, X., Duan, L., . . . Wu, J. (2021b). Integrating deep learning-based data assimilation and hydrogeophysical data for improved monitoring of DNAPL source zones during remediation. Journal of Hydrology, 601, 126655. https://doi.org/10.1016/j.jhydrol.2021.126655

Kang, X., Kokkinaki, A., Shi, X., Yoon, H., Lee, J., Kitandis, P. K., & Wu, J. (2022). Integration of Deep Learning-Based Inversion and Upscaled Mass-Transfer Model for DNAPL Mass-Discharge Estimation and Uncertainty Assessment. Water Resources Research, 58(10). https://doi.org/10.1029/2022WR033277

Klenk, I. D., & Grathwohl, P. (2002). Transverse vertical dispersion in groundwater and the capillary fringe. Journal of Contaminant Hydrology, 58(1–2), 111-128. https://doi.org/10.1016/S0169-7722(02)00011-6

Koch, J., & Nowak, W. (2015). Predicting DNAPL mass discharge and contaminated site longevity probabilities: Conceptual model and high-resolution stochastic simulation. Water Resources Research, 806 - 831. https://doi.org/10.1002/2014WR015478.

Koch, J., & Nowak, W. (2016). Identification of contaminant source architectures—A statistical inversion that emulates multiphase physics in a computationally practicable manner. Water Resources Research, 52, 1009–1025. https://doi.org/10.1002/2015WR017894

Kokkinaki, A., O'Carroll, M., Werth, C. J., & Sleep, B. E. (2013). Coupled simulation of DNAPL infiltration and dissolution in three-dimensional heterogeneous domains: Process model validation. Water Resources Research, 49, 7023-7036. https://doi.org/10.1002/wrcr.20503, 2013

Kokkinaki, A., Werth, C. J., & Sleep, B. E. (2014). Comparison of upscaled models for multistage mass discharge from DNAPL source zones. Water Resources Research, 3187 - 3205. https://doi.org/10.1002/2013WR014663

Kueper, B. H., Stroo, H. F., Vogel, C. M., & Ward, C. H. (2014). Chlorinated Solvent Source Zone Remediation. Springer New York. https://doi.org/10.1007/978-1-4614-6922-3

Lemke, L. D., & Abriola, L. M. (2006). Modeling dense nonaqueous phase liquid mass removal in nonuniform formations: Linking source-zone architecture and system response. Geosphere, 2(2), 74-82. https://doi.org/10.1130/GES00025.1

Marble, J. C., DiFilippo, E. L., Zhang, Z., Tick, G. R., & Brusseau, M. L. (2008). Application of a lumped-process mathematical model to dissolution of non-uniformly distributed immiscible liquid in heterogeneous porous media. Journal of Contaminant Hydrology, 100, 1-10. https://doi.org/10.1016/j.jconhyd.2008.04.003

Miller, C. T., Christakos, G., Imhoff, P. T., McBride, J. F., & Pedit, J. A. (1998). Multiphase flow and transport modeling in heterogeneous porous media: challenges and approaches. Advances in Water Resources, 21(2), 77-120. https://doi.org/10.1016/S0309-1708(96)00036-X

Mobile, M. A., Widdowson, M. A., & Gallagher, D. L. (2012). Multicomponent NAPL Source Dissolution: Evaluation of Mass-Transfer Coefficients. Environmental Science & Technology, 46(18), 10047-10054. https://doi.org/10.1021/es301076p

Molz, F. (2015). Advection, Dispersion, and Confusion. Ground Water, 53(3), 348-353. https://doi.org/10.1111/gwat.12338

Moore, C., & Doherty, J. (2005). Role of the calibration process in reducing model predictive error. Water Resources Research. https://doi.org/10.1029/2004WR003501

Parker, J. C., & Park, E. (2004). Modeling field-scale dense nonaqueous phase liquid dissolution kinetics in heterogeneous aquifers. Water Resources Research, 2004. https://doi.org/10.1029/2003WR002807

Powers, S. E., Abriola, L. M., & Weber Jr, W. J. (1992). An Experimental Investigation of Nonaqueous Phase Liquid Dissolution in Saturated Subsurface Systems: Steady State Mass Transfer Rates. Water Resources Research, 28(10), 2691-2705. https://doi.org/10.1029/92WR00984

Powers, S. E., Abriola, L. M., & Weber, W. J. (1994). An experimental investigation of nonaqueous phase liquid dissolution in saturated systems: Transient mass transfer rates. Water Resources Research, 30(2), 321-332. https://doi.org/10.1029/93WR02923

Rockhold, M., Zhang, Z., & Bott, Y.-J. (2016). Scale-Dependent Solute Dispersion in Variably Saturated Porous Media. Richland, WA: Pacific Northwest National Laboratory.

Saenton, S., & Illangasekare, T. H. (2004). Determination of DNAPL entrapment architecture using experimentally validated numerical codes and inverse modeling. Developments in Water Science, 55, 767-778. https://doi.org/10.1016/S0167-5648(04)80098-4

Saenton, S., & Illangasekare, T. H. (2007). Upscaling of mass transfer rate coefficient for the numerical simulation of dense nonaqueous phase liquid dissolution in heterogeneous aquifers. Water Resources Research, 43(2). https://doi.org/10.1029/2005WR004274

Stewart, L. D., Chambon, J. C., Widdowson, M. A., & Kavanaugh, M. C. (2022). Upscaled modeling of complex DNAPL dissolution. Journal of Contaminant Hydrology, 244. https://doi.org/10.1016/j.jconhyd.2021.103920

Tang, T. (2019). An Adjoint-Sensitivity-Analysis Based Mathematical Framework: DNAPL Source Zone Characterization, Uncertainty Quantification, and Sampling Strategy Design (Doctoral dissertation). Civil and Environmental Engineering. Ann Arbor, MI: Tufts University. Retrieved from ProQuest (Access provided by University Libraries through Virginia Tech)

Watermark Numerical Computing. (2018). Model-Independent Parameter Estimation. User Manual Part II: PEST Utility Suport Software.

White, J. T. (2018). A model-independent iterative ensemble smoother for efficient history-matching and uncertainty quantification in very high dimensions. Environmental Modelling & Software, 109, 191-201. https://doi.org/doi.org/10.1016/j.envsoft.2018.06.009

White, J., Hunt, R., Fienen, M., & Doherty, J. (2020). Approaches to Highly Parameterized Inversion: PEST++ Version 5, a Software Suite for Parameter Estimation, Uncertainty Analysis, Management Optimization and Sensitivity Analysis. Reston, VA: U.S. Geological Survey. https://doi.org/10.3133/tm7C26

Yang, L., Wang, X., Mendoza-Sanchez, I., & Abriola, L. M. (2018). Modeling the influence of coupled mass transfer processes on mass flux downgradient of heterogeneous DNAPL source zones. Journal of Contaminant Hydrology, 211, 1-14. https://doi.org/10.1016/j.jconhyd.2018.02.003

Chapter 3. Numerical modeling and data-worth analysis for characterizing the architecture and dissolution rates of a multicomponent DNAPL source

This chapter was accepted for publication in *Water Resources Research* on May 03, 2023.

3.1. Authors

Andres E. Prieto-Estrada[1], Mark A. Widdowson[1], and Lloyd D. Stewart[2]

[1] The Charles E. Via, Jr. Department of Civil and Environmental Engineering, Virginia Tech, Blacksburg, Virginia 24061-0105, United States

[2] Praxis Environmental Technologies, Inc., 1440 Rollins Road, Burlingame, California 94010, United States

Corresponding author, e-mail address: mwiddows@vt.edu (M.A. Widdowson)

3.2. Key Points

- Aqueous-phase concentrations monitored in a field experiment were simulated to quantify NAPL distribution and dissolution rates
- Depletion profiles of the most soluble DNAPL component accurately constrained the source zone architecture
- Multiscale heterogeneity of source zone architecture controlled the uncertainty of estimated mass transfer coefficients

3.3. Abstract

A numerical solute transport model was calibrated to a high-resolution monitoring dataset to characterize a multicomponent source of nonaqueous phase liquids (NAPLs) and evaluate the uncertainty of estimated parameters. The dissolution of NAPL mass was simulated using SEAM3D with parameter zones including adjustable NAPL saturations and mass transfer coefficients, representing the heterogenous architecture of the source zone. Source zone

parameters were simultaneously estimated using PEST from aqueous-phase concentrations measured in a multilevel monitoring transect and from mass recovery rates measured at extraction wells during a controlled field experiment. Data-worth analyses, facilitated by PEST ancillary software, linked maximum aqueous-phase concentrations of all compounds to reductions in the pre-calibration uncertainty of mass transfer coefficients. In turn, decreasing concentrations of the most soluble NAPL fraction constrained the source mass estimation. The accurate estimation of model parameters was possible by removing concentrations measured during early NAPL dissolution stages, identified as drivers of model bias using the iterative ensemble smoother PESTPP-iES. Although uncertainty analyses highlighted model limitations for representing sub-grid-scale heterogeneity of NAPL distribution and mass transfer rates, final stages of NAPL dissolution measured at multilevel ports eliminated parameter bias and produced long-term projections of multi-stage source zone depletion . Including mass discharge rates for model calibration further improved the accuracy of estimated residual source mass, complementing multilevel monitoring constraints on the saturation distribution and mass transfer coefficients.

3.4. Plain Language Summary

Predicting the persistence of groundwater contamination by dense non-aqueous phase liquids (DNAPLs), such as chlorinated solvents, is crucial for effective environmental stewardship. The dissolution behavior of DNAPL source zones depends on the contaminant mass distribution within hydrogeologic systems, referred to as the source zone architecture, which cannot be measured directly at contaminated sites. We investigated the worth of high-resolution monitoring of aqueous concentrations during a controlled field experiment for indirectly characterizing a multicomponent DNAPL source zone, including its architecture and dissolution behavior. Our methods coupled numerical modeling of groundwater flow and contaminant transport with parameter estimation and uncertainty analysis techniques. Parameter uncertainties were linked to the variability of DNAPL dissolution rates observed at multiple scales of monitoring resolution, including a multilevel transect and groundwater recovery wells. While early aqueous concentration peaks were identified as drivers of model bias, the depletion profile of the most soluble DNAPL component accurately constrained the estimated source architecture and dissolution behavior. Hence, our characterization

approach can benefit remedial designs for managing DNAPL source zones undergoing final depletion stages at sites with monitoring histories.

3.5. Keywords

DNAPL source zone, numerical modeling, uncertainty quantification, DNAPL mass transfer, source zone architecture, contaminant mass discharge

3.6. Introduction

Remediation and long-term dissipation of contaminant source zones comprised of dense nonaqueous phase liquids (DNAPLs) in the subsurface encompasses technical challenges related to uncertainty of DNAPL spatial distribution and dissolution rates (Kueper et al., 2014; Mayer & Hassanizadeh, 2005; NRC, 2005). Entrapped DNAPL mass and saturation distributions in the porous medium, referred to as the source zone "architecture", are key parameters controlling source-zone longevity and depletion behavior (Dekker and Abriola, 2000; DiFilippo & Brusseau, 2008). Typical multistage and nonmonotonic depletion profiles observed in monitoring data reflect the gradual dissolution of NAPL accumulations with characteristic saturations (Brusseau et al., 2013; Kokkinaki et al., 2014; Stewart et al., 2022). Accumulations of low-saturation ganglia allowing for groundwater flow-through account for peaks of discharge concentrations at early NAPL dissolution stages, whereas high-saturation pools with negligible hydraulic accessibility account for dissolution tailing at the final stages of a source lifespan (Christ et al., 2010; Kueper et al., 2014; Yang et al. 2018). Thus, estimating the depletion behavior and remedial timeframes of a source zone requires knowledge on NAPL architecture, which is difficult to characterize with direct observation methods (Engelmann et al., 2019), but can be estimated from field tests and monitoring data using mathematical models of NAPL dissolution (Falta et al., 2005a, 2005b; Stewart et al., 2022).

Numerical modeling methods coupling groundwater flow and contaminant transport with NAPL dissolution have been used to estimate saturation distributions and mass transfer rate coefficients from monitoring data (Frind et al., 1999; Mobile et al., 2012; Saenton & illangasekare, 2004).

Researchers have focused on estimating NAPL architecture or depletion timeframes from synthetically-generated source zones and aqueous-phase concentrations using several mathematical approaches to simulating mass transfer. Several studies considered either a local equilibrium assumption (LEA) or Gilland-Sherwood models of interphase mass transfer (Kang et al., 2021a, 2021b; Marble et al., 2008; Saenton & Illangasekare, 2004). The applicability of LEA in decision-support models is questionable because heterogeneity of aquifer hydraulic properties and DNAPL architecture can induce flow bypassing and mass transfer rate limitations, resulting in nonequilibrium concentrations typically observed at field sites (Falta, 2003; Kokkinaki et al., 2013; Powers et al., 1992, 1994). Similarly, Gilland-Sherwood models rely on correlations between empirical coefficients and soil particle sizes that were determined under specific bench-scale conditions, which may not be applicable to field-scale problems with different hydraulic conditions (Powers et al., 1994; Saenton & Illangasekare, 2007). Additional uncertainties on LEA and Gilland-Sherwood models include grid discretization requirements, as both approaches have been validated with pore-scale experimental data (Agaoglu et al., 2015; Falta, 2003).

Upscaled models have been developed to simulate NAPL dissolution kinetics over a representative elementary volume (REV) incorporating source zone metrics (Christ et al., 2010; Marble et al., 2008; Parker & Park, 2004; Saenton & Illangasekare, 2007; Stewart et al., 2022; Zhu & Skyes, 2004). These metrics include NAPL mass and descriptions of source zone architecture in the form of areal dimensions of NAPL accumulations or the ganglia-to-pool (GTP) mass ratio metric (Abriola et al., 2013; DiFilippo & Brusseau, 2011). Because these metrics are difficult to measure at contaminated sites, upscaled models incorporating a spatially-varying lumped-process mass transfer coefficient have also been used to interpret monitoring data and predict source depletion timeframes (Guo et al., 2020; Marble et al., 2008; Mobile et al., 2012; Park & Parker, 2005). These models simplify the heterogeneity of porous media, aqueous-phase velocities, NAPL architecture, and dispersivity, into a single lumped-process parameter at the REV scale (Falta, 2003; Imhoff et al., 1993; Luciano et al., 2018). Although scale-dependent mass transfer rate coefficients may simplify grid discretization requirements, the parameterization of NAPL source zones for inverse numerical modeling and uncertainty quantification with spatially-correlated random parameter fields is not straightforward (Arshadi et al., 2020; Kang et al., 2021a, 2021b; Kock & Nowak, 2015, 2016)

Given that NAPL source zones have complex spatial morphologies with sharp saturation transitions at fine scales, traditional interpolation and geostatistical methods used in groundwater flow modeling may be not suitable for parameterizing NAPL source zones (Arshadi et al., 2020; Kang et al., 2021a). Alternative methods proposed for parameterizing NAPL source zones include deep learning algorithms trained with images of saturation distributions generated with multiphase flow simulations on highly-resolved permeability fields (Arshadi et al., 2020; Kang et al., 2021a, 2021b), posing additional data requirements and uncertainties on porous media characteristics and model parameters (Abriola, 1989; Agaoglu et al., 2015; Miller et al., 1998). Moreover, these parameterization methods have been tested with synthetically-generated source zones to estimate categories of NAPL saturations through inverse modeling conditioned by borehole data (Arshadi et al., 2020), or by aqueous-phase concentrations under LEA (Kang et al., 2021a, 2021b). Although these methods can generate physically-based, spatially-correlated categorical parameters, they are computationally expensive and require further validation and verification with field data.

Numerical models with parsimoniously parameterized source zones have proved useful for characterizing NAPL architecture and/or lumped-process mass transfer coefficients (Marble et al., 2008; Mobile et al., 2012; Saenton & Illangasekare, 2004). Moreover, combining multilevel monitoring with recovery rates of contaminant mass (or with conventional monitoring wells) can be valuable for characterizing heterogeneous NAPL architectures, as spatially-varying contaminant fluxes may be mapped to soil horizons harboring NAPL mass within a source zone (McMillan et al., 2018). Several studies have incorporated Gilland-Sherwood or upscaled mass transfer functions in discretized NAPL zones or in dual-domain models to estimate grid-scale parameters from multilevel monitoring data and/or mass discharge/flux measurements (Christ et al., 2006; Falta, 2003; Frind et al., 1999; Guo et al., 2020; Mobile et al., 2012; Park & Parker 2005; Saenton & Illangasekare, 2004). Although previous investigations have demonstrated the utility of parameterization parsimony for characterizing NAPL source architecture and dissolution rates with inverse modeling, the uncertainty of grid-scale parameters arising from the assimilation of high-resolution monitoring data has not been investigated.

A primary objective in this numerical modeling study was to evaluate the worth of aqueous-phase concentrations monitored at a multilevel sampling (MLS) transect in combination with total mass

discharge (MD) rates to quantify and reduce the uncertainty of the mass, architecture, and dissolution rates of a multicomponent DNAPL source. The field experiment considered in this study involved the creation a small-scale source zone with a heterogeneous architecture at the Borden experimental site (Broholm et al., 1999). Broholm et al. (2005) quantified the initial mass of the DNAPL mixture using multicomponent NAPL dissolution theory and mass balance analyses. Mobile et al. (2012) estimated the source architecture and dissolution rates from MD profiles and from a single, incomplete MLS nest, using an inverse modeling technique. They constrained the initial NAPL mass by the known amount and the source zone dimensions by the measured post-experimental footprint (Mobile et al., 2012). Our study expanded on both previous analyses by incorporating the entire MLS transect to infer the source footprint and to quantify initial NAPL mass, saturation distribution, and mass-transfer rate coefficients, while examining causality of parameter uncertainty. A secondary objective was to investigate model limitations for reproducing the observed system behavior, further elucidating upon monitoring data assimilation for source zone characterization with inverse numerical modeling, while minimizing the propensity for biasing timeframes of source zone persistence.

3.7. Materials and Methods

3.7.1. Overview of Field Experiment of Multicomponent DNAPL Dissolution

This study incorporated a dataset documenting the dissolution of a DNAPL mixture in a field experiment (Broholm et al., 1999). At the Borden experimental site in Canada, a 5-liter (7.7 kg) mixture of dyed solvents (10% chloroform [TCM], 40% trichloroethylene [TCE], and 50% tetrachloroethylene [PCE] by volume) was injected at approximately 0.05 m below the water table into a 55 m^3 (5.5 m long x 4.5 m wide x 2.3 m deep) unconfined aquifer test cell (Figure 3-1) underlain by a 3-m thick clay aquitard. The Borden aquifer is comprised of clean, well-sorted, medium- to fine-grained lacustrine sand with occasional beds of coarse sand/gravel and silt (Broholm et al., 1999). Although the aquifer is considered relatively homogeneous, the primary sedimentary structure is characterized by horizontal laminations ranging from several mm to several cm in thickness, with commonly-occurring cross-bedding and convolute-bedding features (Rivett et al., 2001). The median grain sizes range from 0.07 to 0.69 mm with very low clay

fractions, while grain roundness ranges from subangular to well-rounded, with an average and uniform aquifer porosity of ~33% (Mackay et al., 1986). In the test cell, the hydraulic conductivity exhibited minimal spatial variability in the shallow region where the DNAPL was released (Broholm et al., 1999; Mobile et al., 2012), with an average value of ~2 m/d (Table A-1).

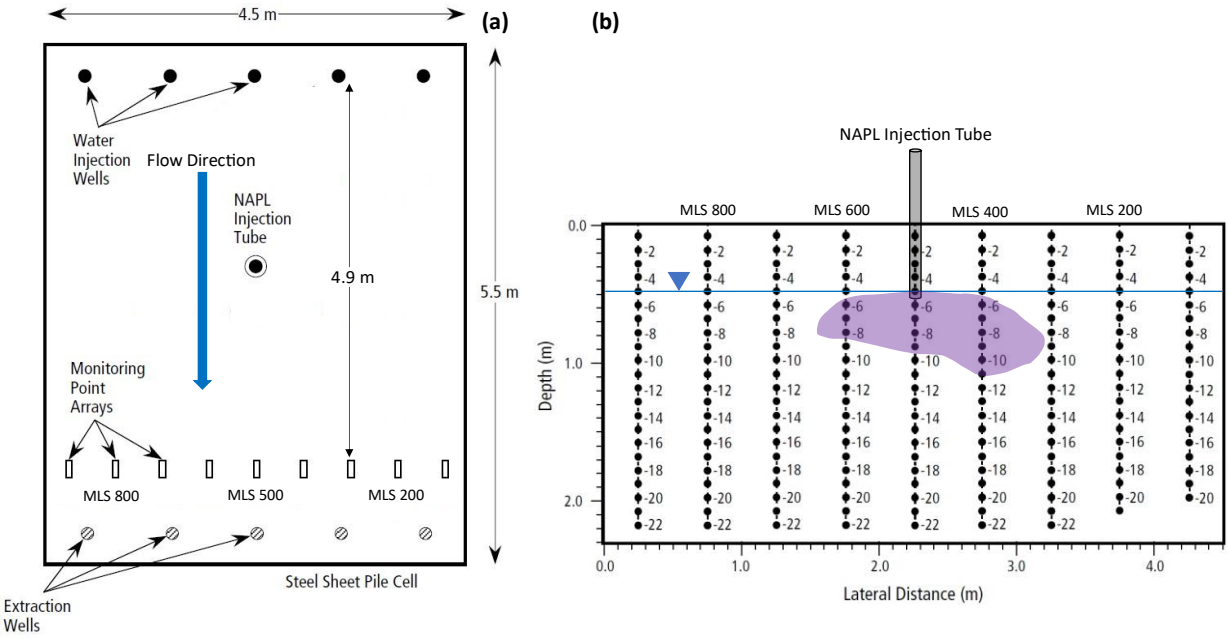

Figure 3-1. Configuration of aquifer test cell. (a) Plan view indicating the location of the groundwater injection/extraction systems, NAPL release point, and MLS nests. (b) Cross-sectional view of the MLS transect indicating the average depth of the water table at ~0.48 m (Broholm et al., 1999) and the approximate source zone extent.

Groundwater flow through the test cell, bounded laterally by sheet piling on four sides, was maintained by a network of five upgradient injection and five downgradient extraction wells. The distance between the injection and extraction networks measured 4.9 m (Figure 3-1). The network was operated at approximately 360 L/d, generating a mean groundwater velocity of 0.13 m/d and horizontal hydraulic gradient of 0.023 ± 0.0024. Flow-weighted concentrations were monitored at the extraction wells with screen lengths spanning the average height (1.82 m) of the saturated zone for 291 days. Aqueous-phase concentrations were also monitored for 220 days in a fence of MLS ports (Figure 3-1) located approximately 2.1 m downgradient from the DNAPL release location. The horizontal spacing of MLS ports was 0.5 m with a vertical spacing of 0.1 m, with screen lengths less than 1 cm. After 220 days of natural dissolution monitoring, a 5.5-day pulse of

methanol was injected in the test cell to evaluate dissolution enhancement processes (Broholm et al., 1999, 2005). The cell was excavated 291 days after the mixture release to map the DNAPL distribution over 5-cm vertical intervals (Broholm et al., 1999).

A previous investigation by Broholm et al. (2005) integrated MLS concentrations and discrete groundwater velocities, estimated from a tracer test, by cross-sectional areas represented by the vertical (10 cm) and horizontal (50 cm) port spacings (Figure 3-2b). They used multicomponent dissolution theory with the MLS-integrated initial concentrations, calculating a source depletion curve to fit the observed trends and thereby estimate the initial DNAPL mass. While the MLS-integrated approach estimated 6.7 Kg, applying the same method to the effluent data resulted in 7.5 Kg. The latter was more accurate because the effluent data was less susceptible to water table fluctuations as compared to discrete measurement uncertainties, capturing the dissolve-phase plume better (Broholm et al., 2005). The authors attributed differences with the initial injected mass of 7.7 Kg to minor volatilization losses, particularly of TCM, at times when the water table was low. Given that all aqueous concentrations were below equilibrium (Broholm et al., 1999, 2005), these studies suggest value in numerical modeling of solute transport and kinetic mass transfer for leveraging all available data within a quantitative uncertainty analysis framework.

3.7.2. Numerical Modeling of Groundwater Flow and Contaminant Transport

A steady-state groundwater flow model was developed with MODFLOW2000 (Harbaugh et al., 2000). The aquifer test cell was discretized in 23 layers with uniform grid blocks measuring 10 cm along all dimensions (Figures 3-2 through 3-4). As shown in Figure 3-2, the extent of the model domain matched the size of the test cell along the vertical dimension (Z-axis) and the horizontal dimension perpendicular to the flow direction (Y-axis). The downgradient dimension (X-axis) of 4.9 m represents the distance between the injection/extraction wells (Figure 3-1). Constant values of hydraulic conductivity, flow boundary conditions, and transport parameters were assigned to match field conditions, which were characterized with tracer tests and soil cores by Broholm et al. (1999) and analyzed with numerical modeling in Mobile et al. (2012). Model layers 1 through 3 were inactivated because the water table fell below the elevation of layer 3 during the monitoring period. Model layer 4 encompassed MLS port 504, which showed evidence of NAPL presence at

0.4 m below the top of the aquifer test cell despite the reported average depth of the water table during the experiment at ~0.48 m (Broholm et al., 1999).

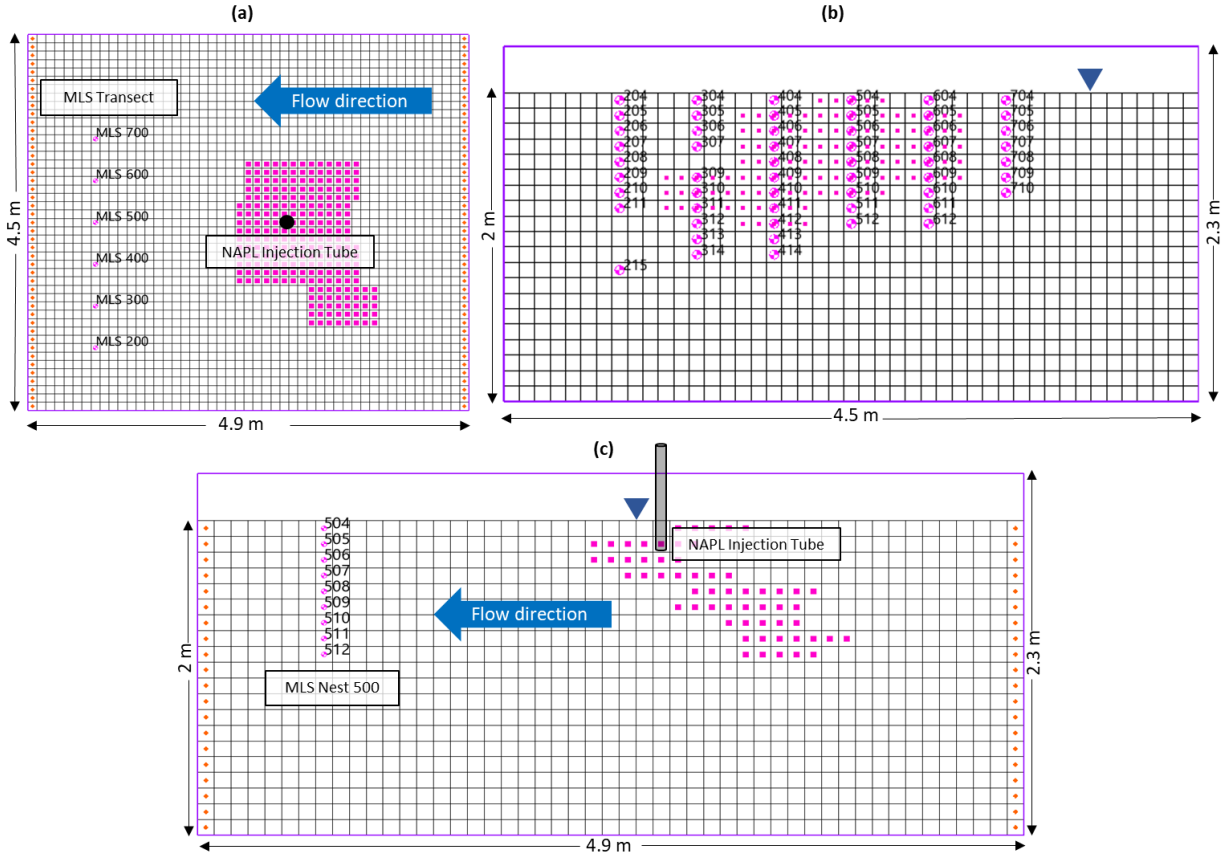

Figure 3-2. Overview of discretized aquifer test cell. (a) Plan view of the source zone and MLS nests, with constant-head boundary conditions representing the steady-state flow conditions maintained by the injection/extraction wells, separated by 4.9 m (Figure 3-1). (b) Cross-sectional view perpendicular to the flow direction. (c) Cross-sectional view parallel to the flow direction. All grid blocks measure 10 cm in every direction. The shown model layers represent the saturated aquifer.

Dissolution of the multicomponent DNAPL source and aqueous-phase contaminant transport were simulated with SEAM3D (Waddill & Widdowson, 2000). Interphase mass transfer [M T^{-1} L^{-3}] was simulated using a linear driving force model:

$$J_i = k_i^N (C_i^{eq} - C_i) \qquad (3\text{-}1)$$

where k_i^N [T^{-1}]is a lumped mass transfer rate coefficient specific to each NAPL phase constituent i, C_i^{eq} [$M\ L^{-3}$] is the equilibrium solubility calculated according to Raoult's Law, and C_i [$M\ L^{-3}$] is the aqueous phase concentration. Equation 3-1 is coupled in SEAM3D to the following relationship representing NAPL dissolution from the soil medium into the aqueous phase:

$$J_i = -\rho_b \frac{dC_i^N}{dt} \tag{3-2}$$

where ρ_b [$M\ L^{-3}$] is the bulk density of the soil and C_i^N [$M\ M^{-1}$] is the NAPL mass of compound i per unit mass of dry soil. A modified version of SEAM3D incorporates the upscaled NAPL dissolution model developed by Parker and Park (2004) to simulate transient mass transfer rates:

$$k_i^N = k_{i,0}^N \left(\frac{\bar{q}}{\overline{K}}\right)^{\alpha} \left(\frac{M_i(t)}{M_{i,0}}\right)^{\beta} \tag{3-3}$$

where $k_{i,0}^N$ = initial mass transfer rate coefficient [T^{-1}], $\bar{q}$ = average Darcy velocity [$L\ T^{-1}$], $\overline{K}$ = average hydraulic conductivity [$L\ T^{-1}$], $M(t)/M_0$ = transient ratio of NAPL mass [$M\ M^{-1}$], α and β are dimensionless empirical parameters. Previous investigations have reported a linear relationship between k_i^N and $\bar{q}$, with α = 1 (Parker & Park, 2004; Park & Parker, 2005). The transient mass ratio raised to the empirical depletion exponent β represents a reduction of NAPL/water interfacial areas over time, regulating tailing of discharge concentrations with reducing mass transfer rates as the source mass is depleted (Parker & Park, 2004; Stewart et al., 2022). A previous modeling study of the same Borden experiment indicated model insensitivity to the β exponent, attributed to a lack of extensive monitoring of decreasing discharge concentrations (Mobile et al., 2012). In this work, both the α and β parameters were set to zero to focus the uncertainty and data-worth analyses on the spatially-variable parameters $k_{i,0}^N$ and C_0^N. Adjusting C_0^N parameters allowed to estimate the initial mass (M_0^N [M]) of the entire NAPL mixture and quantify its uncertainty, as SEAM3D generates an output of remaining NAPL mass in the source zone every time step using Equation 3-4, by adding the mass of all grid blocks where a C_0^N parameter value was assigned:

$$M_0^N = \sum_{Zone\ 1}^{Zone\ 23} V^N \times C_0^N \times \rho_b \qquad (3\text{-}4)$$

where V^N [L^3] = NAPL zone volume. The source zone was represented with 23 NAPL zones (Figures 3-3 and 3-4) positioned upgradient of MLS ports which showed contaminant breakthrough, suggesting the upgradient presence of NAPL mass (Figures 3-5, 3-6, and 3-7). Each NAPL zone was comprised of 25 grid blocks (Figures 3-3 and 3-4) and was assigned one pair of adjustable parameters, k_0^N and C_0^N, representing uniform mass distribution and dissolution within each NAPL zone. The areal dimensions of all NAPL zones were designed as 0.5 m x 0.5 m on the horizontal plane representing the horizontal spacing of MLS ports, whereas vertical layers of 0.1 m represented the vertical spacing between ports. The location of NAPL zones was determined by contaminant travel times analyzed from MLS breakthrough data. Overall, the source distribution in the model encompassed the observed post-excavation footprint (Figures 3-3 and 3-4), which likely developed through vertical and downward NAPL migration throughout the experiment (Broholm et al., 1999, 2005).

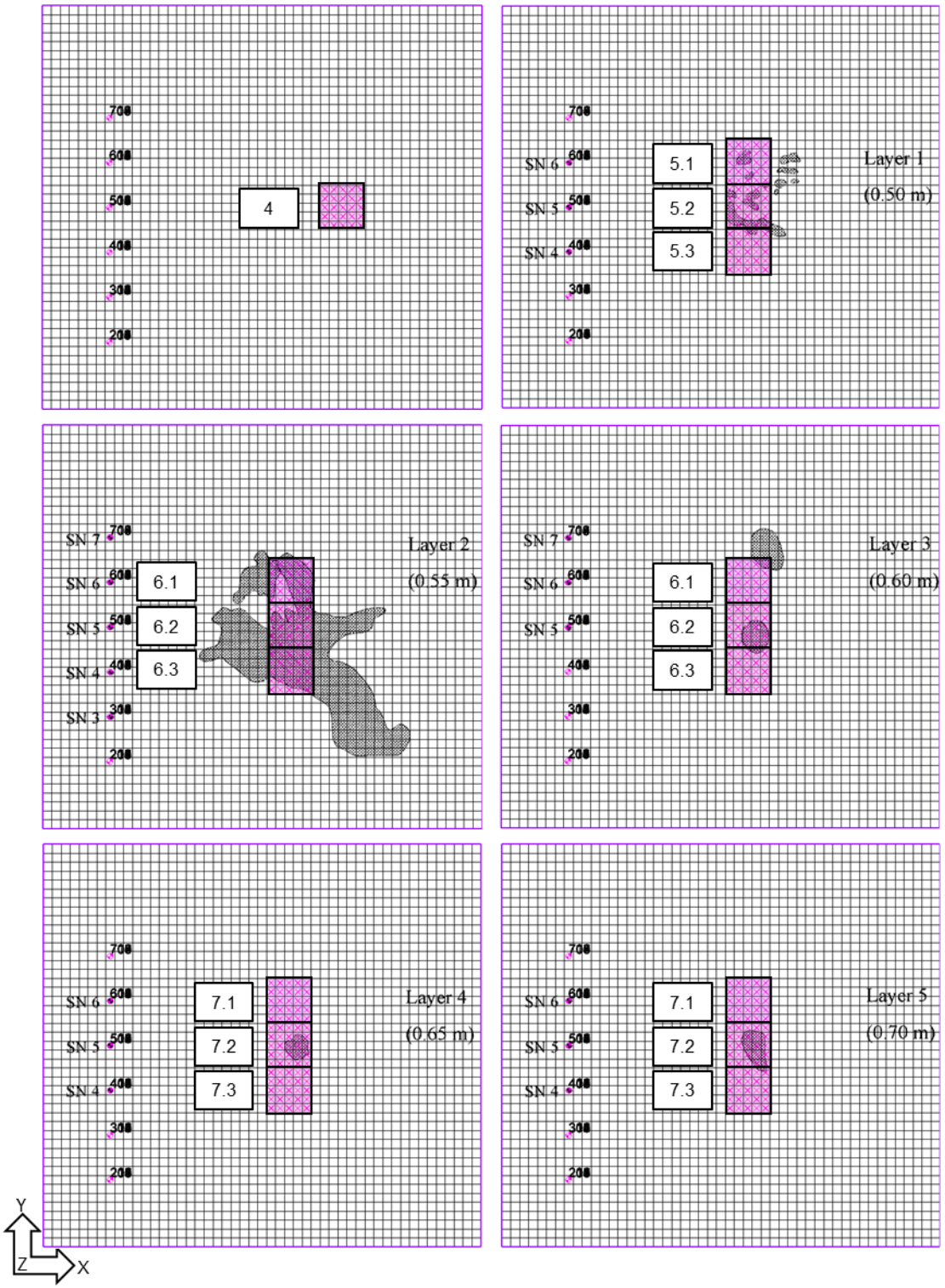

Figure 3-3. Grid-scale NAPL zones in model layers 4 through 7. All NAPL zones measured 0.5 m x 0.5 m on the horizontal plane, encompassing 25 grid blocks. Model layers measure 0.1 m along the Z-axis representing the vertical spacing between MLS ports. The post-experimental NAPL footprint mapped in 0.05-m vertical increments (excavation layers) by Broholm et al. (1999) is included for reference.

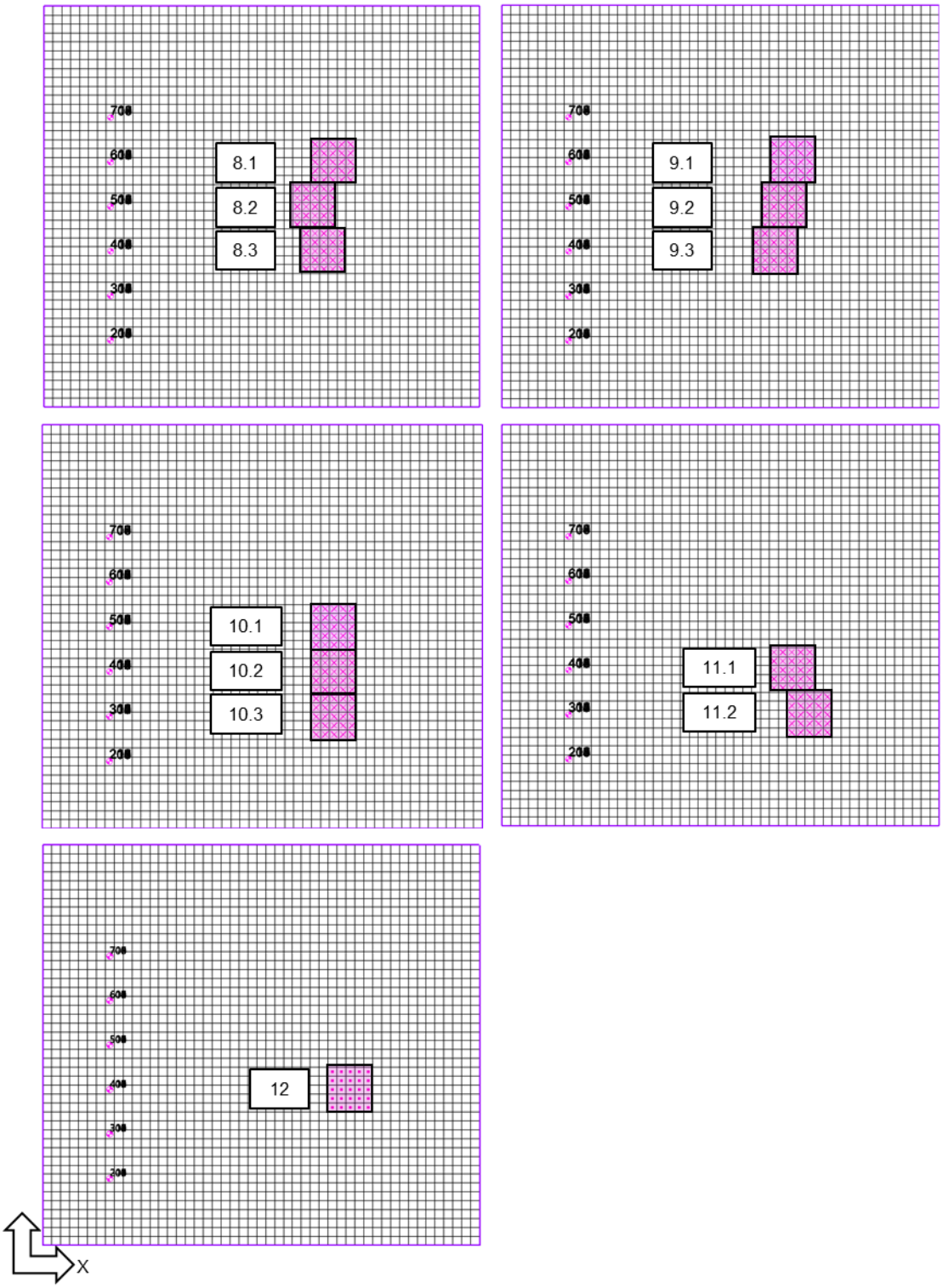

Figure 3-4. Grid-scale NAPL zones in model layers 8 through 12.

3.7.3. Parameter Estimation and Uncertainty Quantification

For each NAPL zone, C_0^N and k_0^N were simultaneously estimated from monitoring data. In addition, two global k_0^N multipliers to identify compound-specific mass transfer coefficients for TCE and PCE ($k_{TCE,0}^N$ and $k_{PCE,0}^N$) were estimated as multipliers of $k_{TCM,0}^N$ for a total of 48 adjustable source zone parameters. History-matching targets included 1,556 measurements of dissolved TCM, TCE, and PCE concentrations monitored at the MLS transect (Figure 3-1), out of 4,770 measurements comprising the entire MLS dataset. The 1,566 MLS targets corresponded to 23 ports including concentration measurements through 130 days (Figures 3-5, 3-6, and 3-7), when extraction well redevelopment abruptly increased the water table by 1 m causing significant data noise through 220 days (Broholm et al., 1999; Mobile et al., 2012). These MLS targets were grouped by sampling port and a weight of 1 was assigned to each aqueous-phase concentration measurement within each port. Additional constraints included 78 measurements of mass discharge rates monitored at extraction wells for 220 days (before methanol remediation was implemented). Mass discharge measurements were grouped by contaminant (i.e., three MD groups) and assigned uniform weights, balancing the initial error contribution of each group to the objective function (Φ). Specifically, individual measurements of MD were assigned a weight of 250 within the TCM and TCE MD groups, whereas individual PCE MD measurements were assigned a weight value of 500. This empirical weighting strategy was designed to balance the visibility of MD groups with MLS ports for Φ minimization, conferring component-specific MD groups equal consideration for parameter estimation given that measured PCE MD rates were lower than TCM and TCE values.

An initial parameter estimation with PEST_HP (Doherty, 2020), which uses a parallelizable gradient-based optimization process, only included the MLS targets. All k_0^N and C_0^N parameters were log-transformed to facilitate the nonlinear optimization process. Bounds for C_0^N parameters were designed as a function of initial NAPL saturation (S_0^N [%]) of the pore space calculated as:

$$S_0^N = \frac{\rho_b C_0^N}{\rho_N \theta} \tag{3-5}$$

where ρ_N [M L^{-3}] is the NAPL density and θ is the soil porosity. Bounds for C_0^N parameters were set as $0.05 < S_0^N$ (%) < 25 for most NAPL zones, and as $0.05 < S_0^N$ (%) < 5 for NAPL zones below layer 10 and in layer 4. The prior (pre-history matching) NAPL mass value was set as ~120 % greater than the known initial mass (7.7 kg). This prior value was established to evaluate whether initial history-matching of MLS data with PEST_HP could result in a total NAPL mass estimate close to the known value. Bounds for all k_0^N ($k_{0,TCM}^N$) parameters were set as $0.01 < k_0^N$ (d^{-1}) < 7.5 following an order-of-magnitude range obtained through a simplified mass transfer correlation defined in Frind et al. (1999), where the dissolution of a large-scale DNAPL mixture in the Borden aquifer was simulated using a similar grid scale. Bounds for k_0^N compound-specific multipliers were kept consistent with ratios determined by Mobile et al. (2012) as $0.95 < k_{0,TCE}^N < 1$ and $0.8 < k_{0,PCE}^N < 0.95$.

The posterior uncertainty of NAPL mass was quantified with the iterative ensemble smoother PESTPP-iES (White et al., 2020). PESTPP-iES undertakes Monte-Carlo sampling of parameter uncertainty bounds generating ensembles which are upgraded with the Gauss-Levenberg-Marquardt (GLM) optimization algorithm. Rather than fitting simulation results to data, PESTPP-iES can generate observation ensembles considering a multi-gaussian distribution of measurement noise ($\boldsymbol{\varepsilon}$) (White, 2018). Here, σ_ε was defined as 5% of measured values. This stochastic approach was used for history-matching of (i) MLS data only, and (ii) both MLS and MD data, quantifying the posterior uncertainty of parameters (C_0^N, k_0^N) and predictions (M_0^N). In the following sections, Model A = optimized with PEST_HP using MLS data only, Model B = optimized with PESTPP-iES using MLS data only, and Model C = optimized with PESTPP-iES combining MLS and MD data.

Parameter bounds were used to define 95% confidence intervals of multi-gaussian prior probability distributions (PDF) of model parameters, assuming statistically-uncorrelated NAPL zones. The upper C_0^N bounds for NAPL zones were reduced from 25% to 15% S_0^N and initial parameter values were set from PEST_HP results. Prior to parameter upgrading, PESTPP-iES undertakes a prior-based Monte Carlo analysis to detect "prior-data conflicts" (PDC). These represent measurements that cannot be simulated by covering measurement realizations, created by PESPP-iES using σ_ε values, with randomized model realizations (White et al., 2020, 2021). All PDCs flagged by

PESTPP-iES were removed to eliminate model bias induced by history matching. Otherwise, erroneous parameter results would compensate for "model defects" (e.g., multi-rate NAPL dissolution below the grid resolution and NAPL migration) and data noise, lumped together as "model error", biasing model predictions (White, 2018; Doherty & Moore, 2020). Moreover, PESTPP-iES tracks the evolution of a "base realization" during the optimization process, corresponding to the initial parameter realization upgraded without **ε** ensembles. Estimates of NAPL mass removed by natural dissolution produced by Model A were compared to estimates generated with the posterior base realization of Models B and C.

3.7.4. Data-Worth Analysis

First-order second-moment (FOSM) analysis was used to evaluate data worth for reducing the uncertainty of model parameters and predictions through history-matching. The GENLINPRED and PREDUNC utilities from the PEST software suite (Watermark Numerical Computing, 2018) were used for FOSM analyses. The primary assumption in FOSM analysis is model linearization (Equation 3-5):

$$\mathbf{h} = \mathbf{Zk} + \boldsymbol{\varepsilon} \tag{3-6}$$

which states that a vector of measurements of system state **h** (aqueous-phase concentrations) equals the action of the model **Z** (Jacobian sensitivity matrix weighted by $\sigma_{\varepsilon}^{-1}$) on a vector of parameters **k** plus a vector of measurement noise **ε** (Doherty, 2015). In this case, $\sigma_{\varepsilon}^{-1}$ was calculated on the basis of misfit between measurements and model outputs using the PEST-based utility PWTADJ2 (Watermark Numerical Computing, 2018) after history-matching. GENLINPRED and PREDUNC calculate the posterior uncertainty variance of model parameters through covariance propagation:

$$C'(\mathbf{k}) = C(\mathbf{k}) - C(\mathbf{k})\mathbf{Z^t}[\mathbf{Z}C(\mathbf{k})\mathbf{Z^t} + C(\boldsymbol{\varepsilon})]^{-1}\mathbf{Z}C(\mathbf{k}) \tag{3-7}$$

where the posterior covariance matrix C'(**k**) is obtained through history-matching (Doherty, 2015). In this case, the prior covariance matrix C(**k**) is diagonal with no spatial correlations between

NAPL zones. The estimated initial NAPL mass, a SEAM3D output, was treated as a linearized model prediction:

$$s = \mathbf{y^t k} \tag{3-8}$$

where **y** is a vector of sensitivities of *s* with respect to **k**. The prior (σ_s^2) and posterior ($\sigma'_s{}^2$) uncertainty variances of *s* were calculated as:

$$\sigma_s^2 = \mathbf{y^t} C(\mathbf{k}) \mathbf{y} \tag{3-9}$$

$$\sigma'^2_s = \mathbf{y^t} C'(\mathbf{k}) \mathbf{y} \tag{3-10}$$

The worth of individual MLS ports for reducing prior parameter uncertainties was calculated with model A, whereas the worth of compound-specific MLS and MD datasets was calculated with the posterior base realization of model C. Model C was also used to quantify the worth of individual MLS and MD measurements and to quantify the relative uncertainty variance reduction (RUVR) of each parameter (*i*), defined as:

$$RUVR_i = 1 - \frac{\sigma'^2_i}{\sigma_i^2} \tag{3-11}$$

where σ_i^2 are prior parameter variances encapsulated in C(**k**) and $\sigma'_i{}^2$ are posterior parameter variances extracted from C'(**k**) (Doherty, 2015).

3.8. Results and Discussion

3.8.1. Parameter Estimation and Uncertainty Quantification

A comparison of estimated NAPL mass and k_0^N multipliers is presented in Table 3-1. In general, the known NAPL mass (7.7 Kg) was underestimated (6.4 – 7.2 Kg) when history-matching to MLS data only, particularly with gradient-based optimization (PEST_HP). An improvement in the

accuracy of mass estimation with PESTPP-iES was achieved through the removal of 206 PDC values flagged by PESTPP-iES (Figures 3-5, 3-6, and 3-7) comprising 13% of the MLS constraints. Likewise, 10 PDCs (Figure 3-8) representing 13% of the MD dataset were also flagged by PESTPP-iES and removed for history-matching. Including the MD constraints resulted in an excellent agreement with the known initial source mass, which was encompassed by 95% confidence limits (Table 3-1). Prior-based Monte Carlo results suggested that emphasizing early peak concentrations for history-matching can result in underestimation of NAPL mass and overestimation (bias) of k_0^N values, leading to underestimation of source dissipation timeframes. In this case, removing PDC values, rather than modifying the model design, was sufficient to accurately estimate NAPL mass and constrain mass transfer coefficients.

Table 3-1. Model-estimated DNAPL mass and k_0^N multipliers.

Parameter/Prediction	PEST_HP (A: MLS)	PESTPP-iES (B: MLS)	PESTPP-iES (C: MLS and MD)
Mass (Kg)	6.367	μ = 7.187 σ = 0.120	μ = 7.626 σ = 0.110
$k_{0,TCE}^N$ (d^{-1})	1.00	μ = 0.99 σ = 0.006	μ = 0.99 σ = 0.005
$k_{0,PCE}^N$ (d^{-1})	0.95	μ = 0.93 σ = 0.018	μ = 0.88 σ = 0.017

μ = mean estimated value. σ = standard deviation of estimated parameters (k_0^N) and predictions (Mass).

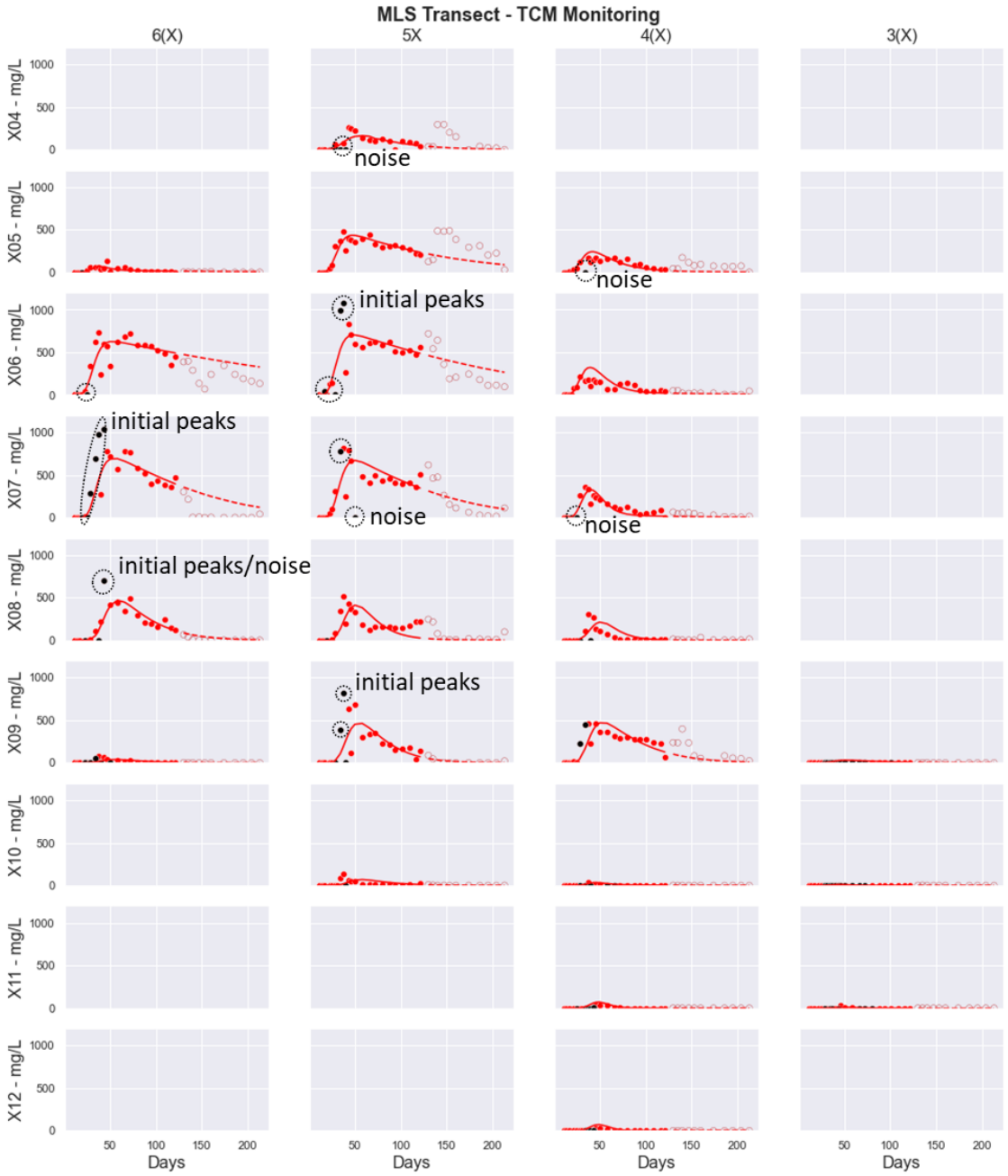

Figure 3-5. Comparison of measured (circles) and simulated (lines) aqueous-phase TCM concentrations at the MLS fence. Simulation results correspond to the posterior base realization of model C, including MLS and MD constraints. Empty circles correspond to concentrations ignored for history-matching because of significant measurement noise induced by water table fluctuations after 130 days of monitoring. The dashed lines correspond to simulated values beyond 130 days, informed by MD data exclusively. Black-filled circles are prior-data conflicts removed from the history-matching process to avoid parameter bias. The dashed circles emphasize some of the detected PDC values labeled as “initial peaks” and “noise”.

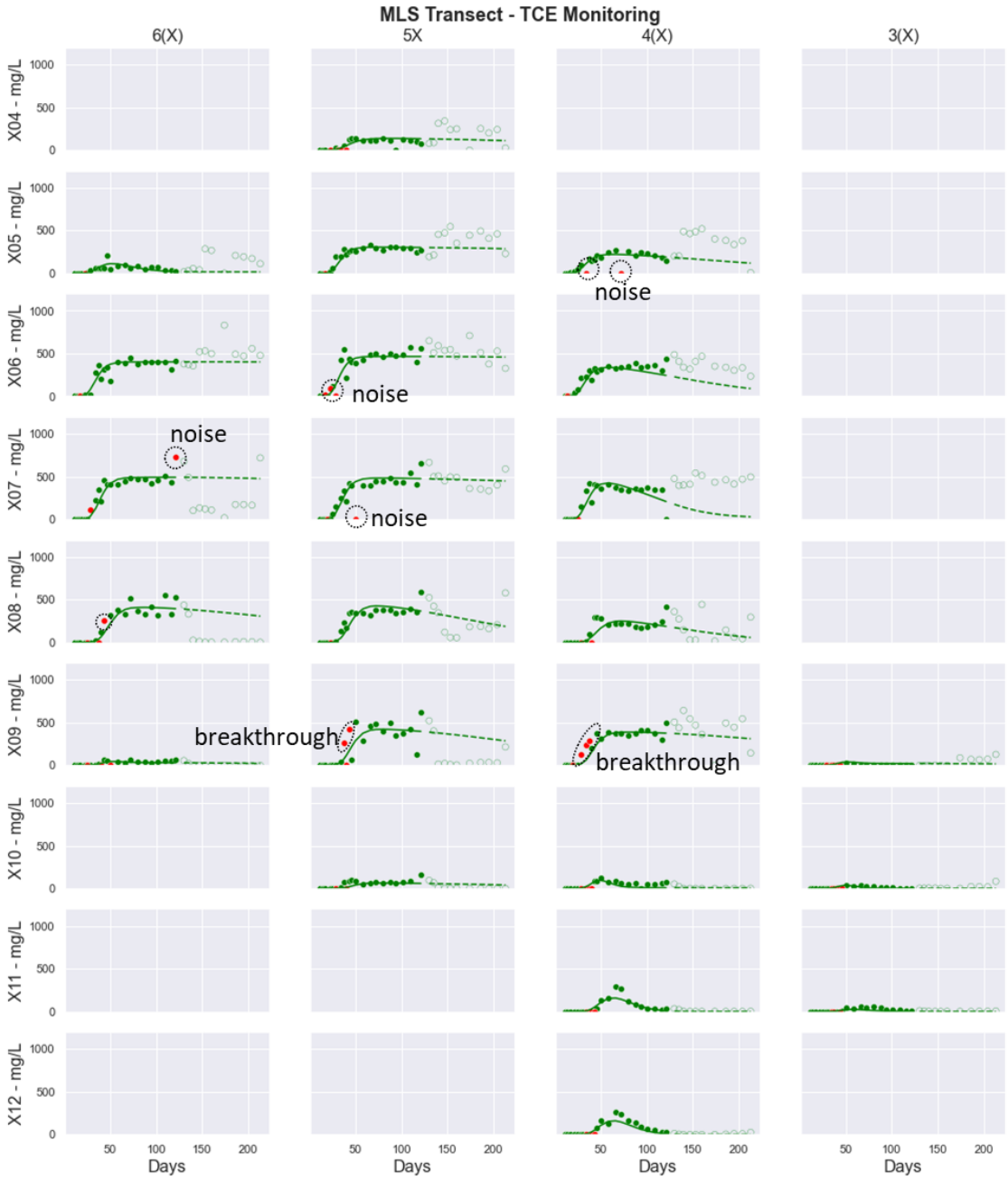

Figure 3-6. Comparison of measured (circles) and simulated (lines) aqueous-phase TCE concentrations at the MLS fence. Simulation results correspond to the posterior base realization of model C, including MLS and MD constraints. Empty circles correspond to concentrations ignored for history-matching because of significant measurement noise induced by water table fluctuations after 130 days of monitoring. The dashed lines correspond to simulated values beyond 130 days, informed by MD data exclusively. Red-filled circles are prior-data conflicts removed from the history-matching process to avoid parameter bias. The dashed circles emphasize some of the detected PDC values labeled as “breakthrough” and “noise”.

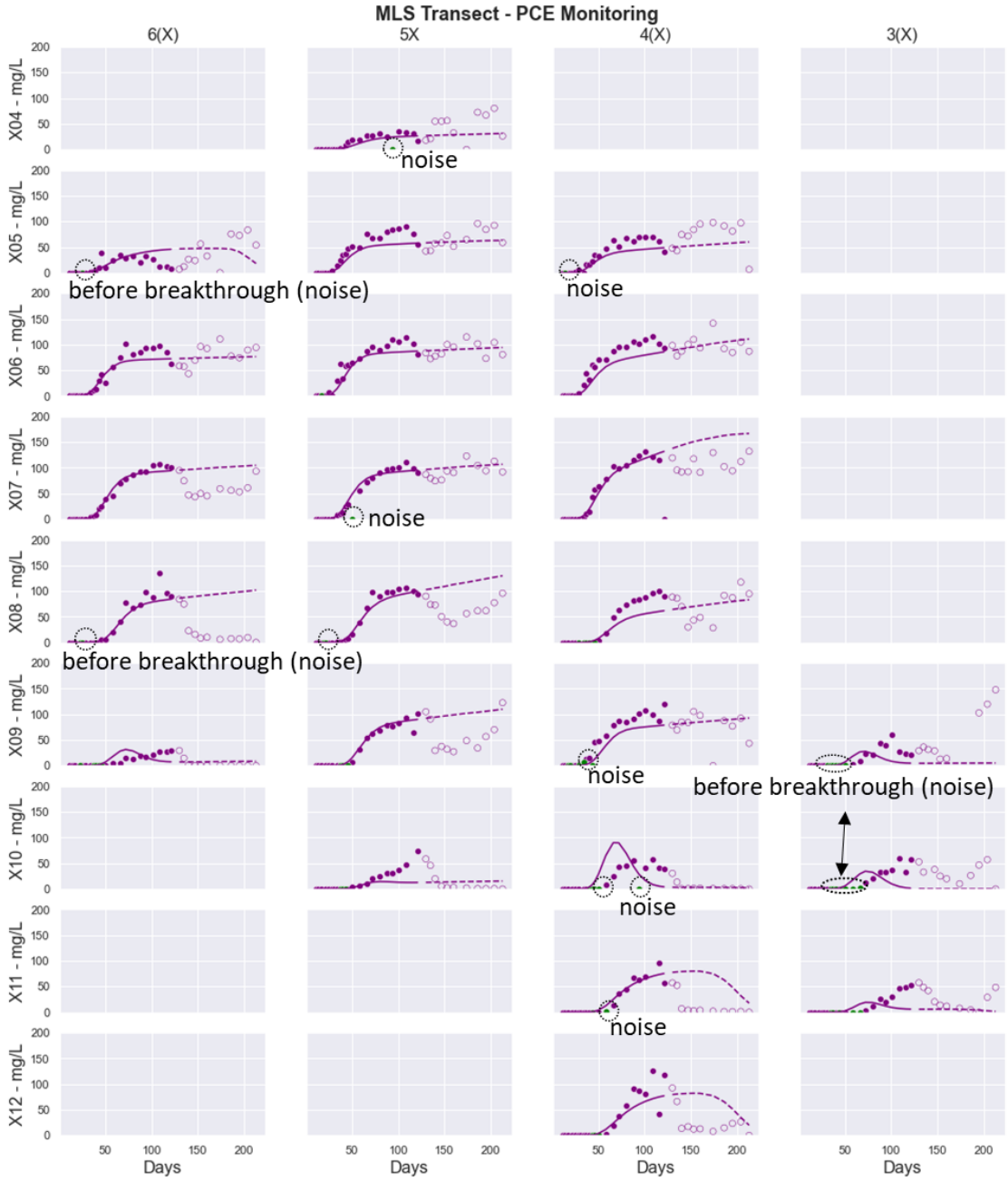

Figure 3-7. Comparison of measured (circles) and simulated (lines) aqueous-phase PCE concentrations at the MLS fence. Simulation results correspond to the posterior base realization of model C, including MLS and MD constraints. Empty circles correspond to concentrations ignored for history-matching because of significant measurement noise induced by water table fluctuations after 130 days of monitoring. The dashed lines correspond to simulated values beyond 130 days, informed by MD data exclusively. Green-filled circles are prior-data conflicts removed from the history-matching process to avoid parameter bias. The dashed circles emphasize some of the detected PDC values labeled as “before breakthrough” and “noise”.

Prior-data conflicts pertaining to each dissolved NAPL component were detected at similar locations along the MLS and MD profiles (Figures 3-5 through 3-8). Most PDCs corresponded to initial TCM concentration peaks (Figure 3-5), some were detected at TCE breakthrough (Figure 3-6), and a few before PCE breakthrough (Figure 3-7). Most PDCs were attributed to measurement noise ($\boldsymbol{\varepsilon}$), encompassing possible sampling/analytical error, water table fluctuations, and/or dissolution heterogeneities that cannot be simulated explicitly. In addition, the dynamic evolution of the source zone architecture by DNAPL migration during the experiment may have contributed to differences in PDC locations along monitoring profiles on a component-specific basis. For example, PDCs at initial TCM peaks (Figures 3-5 and 3-8) may represent early ganglia dissolution favoring TCM mass transfer driven by its relatively high solubility (Equation 3-1), whereas peaks of TCE and PCE were covered by model ensembles because their dissolution rates were lower than the DNAPL migration rate. Specifically, this explained why DNAPL mass was depleted of TCM below MLS level X09 (Figure 3-5) relative to TCE (Figure 3-6) and PCE (Figure 3-7). Relatively late PCE breakthrough below MLS level X09 was also identified by Broholm et al. (1999) as evidence of DNAPL migration with an evolving composition.

In theory, the dissolution of NAPL mixtures has been described as a chromatographic process, where component-specific mass transfer zones propagate at different velocities through NAPL accumulations as a function of their local solubilities and downgradient length (Geller & Hunt, 1993; Soerens et al., 1998). In practice, the numerical discretization of NAPL zones along the flow direction may influence the estimation of k_0^N values, as grid-scale concentration gradients (Equation 3-1) would also regulate the mass transfer simulation for any prescribed q (Darcy velocity) and $\alpha_{L,T}$ (dispersivity) values (Falta, 2003; Frind et al., 1999; Hunt & Sitar, 1988; Rivett & Feenstra, 2005). In this work, the horizontal discretization was designed for numerical stability of the aqueous-phase transport simulation with a downgradient grid Peclet number of $Pe_x = \Delta X / \alpha_L = 2$. Although fitting $\alpha_{L,T}$ parameters to history-matching targets may account for early dissolution PDC values, driving $k_{i,0}^N$ uncertainty, PDC removal in this case accurately constrained the mass transfer simulation and architecture estimation on the basis of steady-state PCE dissolution profiles (Figure 3-10), and the TCM and TCE dissolution tailing profiles (Figures 3-5 and 3-6) representative of the heterogeneous multicomponent source depletion.

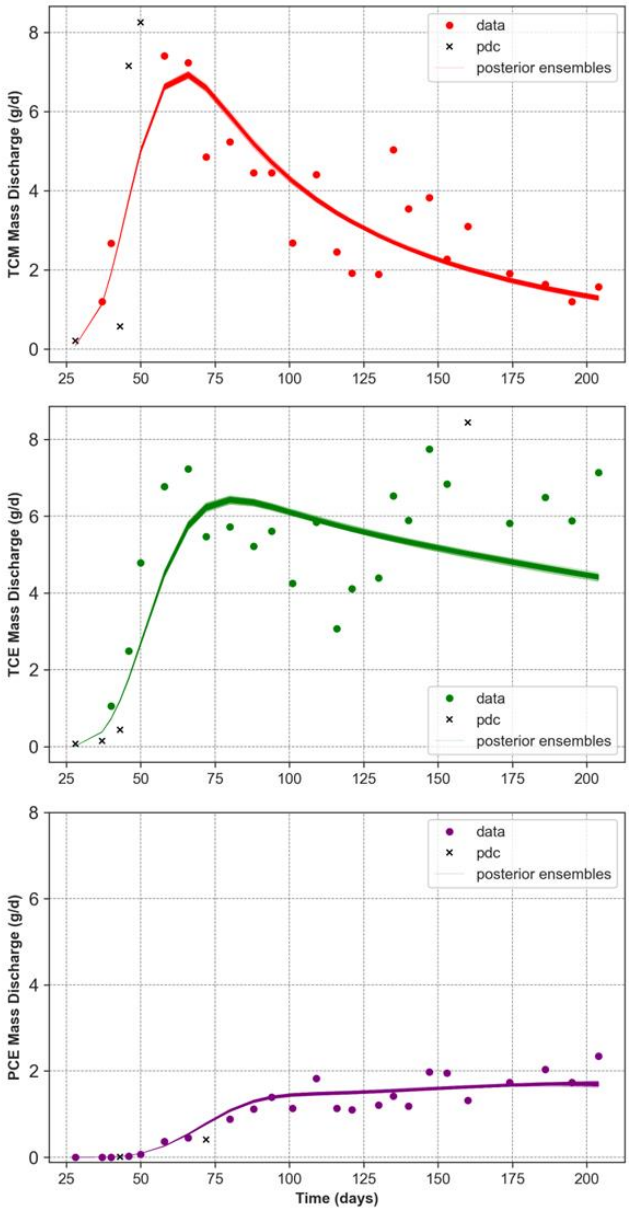

Figure 3-8. Posterior ensembles of MD profiles generated with model C.

Table 3-1 indicates that both $k_{i,0}^{N}$ multipliers estimated with Model A showed a tendency to reach their upper bounds. Only the values of $k_{PCE,0}^{N}$ estimated with PESTPP-iES were constrained within their prior uncertainty bounds (Table 3-1). In addition to the **ε** effects on potential parameter bias, multistage NAPL dissolution below the MLS scale may have impacted posterior results. For example, inspecting the TCM signature of ports 506 and 507 in Figure 3-5 suggested two slopes of declining concentrations before 130 days. An initially steep slope between the concentration peaks through day 50, followed by a more gradual slope through day 130, suggested heterogeneity

of NAPL architecture and dissolution below the MLS scale. Despite removing PDCs, sub-grid-scale multistage NAPL dissolution cannot be adequately simulated with a single parameter set (C_0^N, k_0^N) per NAPL zone. This explained why model A produced lower mass estimates with an increased propensity for biasing (overestimating) $k_{TCM,0}^N$ parameters (e.g., port 608 in Table 3-2), whereas model B (PDC targets removed) produced $k_{TCM,0}^N$ values consistent with model C (Table 3-2). Although these results suggested that a dual-domain approach may have better captured TCM profiles at MLS ports, removing PDCs to estimate single-domain parameters accurately constrained NAPL mass and a consistent range of $k_{0,TCM}^N$ values. However, identifying a final stage of NAPL depletion in monitoring data, such as the TCM profiles in this work, may not be straightforward in a field setting. In that case, dual-domain models with an explicit, physical mass transfer basis supported by direct source delineation/characterization data (e.g., borehole data, laser induced fluorescence LIF, membrane interface probe MIP, or aquifer profiling tools) would provide an opportunity to estimate NAPL dissolution rates, which may be refined by fitting monitoring data (Stewart et al., 2022). In either case, performing a prior-based Monte Carlo analysis would allow for identifying drivers of model bias, including removal of PDC values cause by data noise, or if necessary, refining model conceptual assumptions to simulate observations without incurring parameter bias (White et al., 2021).

Table 3-2. Distribution of estimated DNAPL mass and mass transfer coefficients

NAPL	MLS	$k_{TCM,0}^{N}$ (day^{-1})			NAPL Mass (Kg)		
Zone	Port	A	B	C	A	B	C
4	404	0.037	0.041	0.041	0.14	0.14	0.15
5.1	605	0.038	0.029	0.037	0.02	0.02	0.01
5.2	505	0.102	0.104	0.106	0.59	0.59	0.64
5.3	405	0.050	0.061	0.067	0.12	0.13	0.13
6.1	606	0.174	0.171	0.175	1.23	1.63	1.79
6.2	506	0.252	0.226	0.236	1.16	1.32	1.43
6.3	406	0.147	0.138	0.131	0.10	0.11	0.13
7.1	607	0.735	0.282	0.303	0.79	0.93	0.96
7.2	507	0.183	0.231	0.251	0.79	0.81	0.85
7.3	407	0.303	0.255	0.245	0.11	0.11	0.11
8.1	608	3.259	0.220	0.202	0.33	0.35	0.36
8.2	508	0.227	0.254	0.204	0.15	0.17	0.20
8.3	408	0.108	0.115	0.082	0.07	0.07	0.09
9.1	609	0.385	0.019	0.048	0.00	0.00	0.00
9.2	509	0.248	0.196	0.216	0.29	0.30	0.31
9.3	409	0.314	0.184	0.171	0.35	0.38	0.40
9.4	309	0.010	0.010	0.066	0.01	0.00	0.00
10.1	510	0.024	0.033	0.016	0.03	0.02	0.04
10.2	410	0.015	0.068	0.534	0.01	0.01	0.01
10.3	310	0.010	0.015	0.049	0.01	0.00	0.00
11.1	411	0.056	0.097	0.081	0.02	0.03	0.02
11.2	311	0.010	0.017	0.084	0.02	0.01	0.00
12	412	0.077	0.109	0.083	0.02	0.03	0.02
Total NAPL Mass (Kg)					6.4	7.2	7.6

A (PEST_HP, MLS only), B (PESTPP-iES, MLS only), C (PESTPP-iES, MLS and MD)

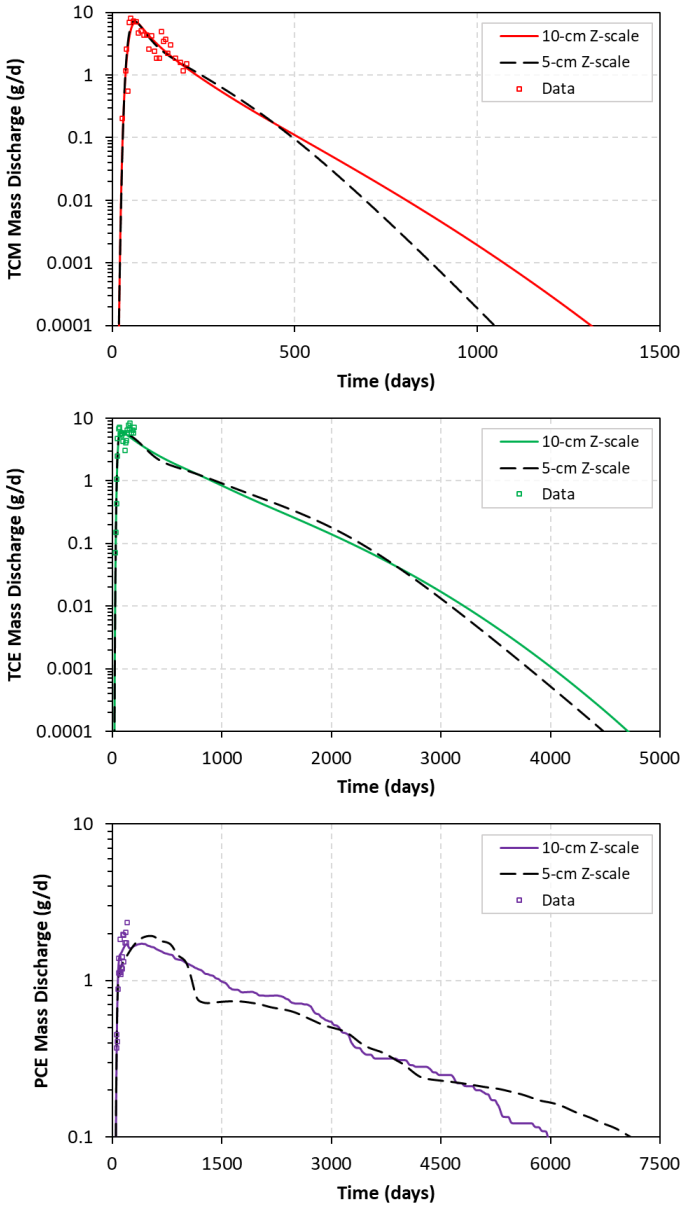

Figure 3-9. Comparisons of long-term projections of MD profiles generated with the base parameter realization of model C (continuous lines) and the modeling results of Mobile et al. (2012) (dashed lines). All projections were generated with $\beta = 0$. In both cases, multistage behavior of NAPL depletion emerged from the NAPL architecture, which was constrained by the known mass and the post-experiment source footprint in Mobile et al. (2012). Small differences in long-term projections of source depletion emphasized the importance of constraining the source mass.

Long-term projections of MD using the posterior base realization of Model C (Table 3-2) are compared to the model calibrated by Mobile et al. (2012) in Figure 3-9. In both cases, multistage dissolution profiles emerged from the spatial distribution of NAPL mass and dissolution rates, as

MD projections were produced with $\beta = 0$ (Equation 3-3). The mass transfer rates shown in Table 3-2 encompassed the same order-of-magnitude range reported in Mobile et al. (2012), although the values determined in this study were lower by ~50% on average, reflecting the grid-scale dependence of estimated k_0^N values. Specifically, the grid-block size in Mobile et al. (2012) of 500 cm^3 was also 50% smaller than the 1000 cm^3 scale used in this study. For this experiment, both the 5-cm-thick (excavation-layer NAPL parameterization) and 10-cm-thick (vertical MLS port spacing) layers are suitable for parameter estimation because while MLS screen lengths are below 10 cm, mixing and dilution along the flow path is captured by the MLS port spacing (Broholm et al., 1999, 2005). In both cases, the horizontal grid resolution is numerically stable for the simulated transport conditions, but history-matching more adjustable NAPL-zone parameters than available MLS ports, using 5-cm thick layers, resulted in erroneous mass overestimation by orders of magnitude and inconsistent k_0^N and C_0^N distributions (results not shown) by a lack of inversion regularization. Here, regularization was achieved by parsimony between NAPL zones and MLS ports.

3.8.2. FOSM-Analysis Results

The worth of monitoring datasets for reducing prior uncertainty variance of NAPL mass is shown in Figure 3-10. This figure highlights the importance of TCM data for constraining NAPL mass in contrast to the negligible worth in the monitoring profiles of other dissolved components. Likewise, Figure 3-10 shows the increase in data worth for reducing prior uncertainty of NAPL mass by removing PDCs. Although the short-term TCM MLS signatures (< 130 days) alone constrained the prior uncertainty of NAPL mass by ~100%, adding the complete TCM MD signature (220 days) improved mass estimates by spreading $\boldsymbol{\varepsilon}$ induced by water table fluctuations across all NAPL zones. Furthermore, Table 3-3 indicates a decrease in the worth of MLS ports commensurate with the S_0^N of their corresponding upgradient NAPL zones. This apparent correlation reflected the similarity between the TCM dissolution profile of each MLS port and the TCM MD profile, emphasizing the indirect value of multilevel monitoring for characterizing NAPL distribution and reducing the uncertainty of source depletion rates.

Table 3-3. Distribution of S_0^N and worth of MLS ports for reducing prior uncertainty of NAPL mass.

NAPL Zone	MLS Port	Prior Uncertainty Variance Decrease	S_0^N (%) A	S_0^N (%) B	S_0^N (%) C
6.1	606	54.0%	9.7%	12.8%	14.0%
6.2	506	42.6%	9.1%	10.4%	11.2%
7.2	507	19.0%	6.2%	6.4%	6.7%
7.1	607	15.7%	6.2%	7.3%	7.5%
5.2	505	5.1%	4.6%	4.6%	5.1%
8.1	608	4.0%	2.6%	2.8%	2.8%
6.3	406	3.2%	0.8%	0.9%	1.0%
7.3	407	2.7%	0.9%	0.9%	0.9%
8.2	508	2.6%	1.2%	1.3%	1.6%
9.3	409	2.4%	2.8%	3.0%	3.1%
9.2	509	1.8%	2.3%	2.4%	2.4%
5.1	605	1.5%	0.1%	0.1%	0.1%
9.1	609	0.7%	0.0%	0.0%	0.0%
9.4	309	0.6%	0.1%	0.0%	0.0%
5.3	405	0.6%	1.0%	1.0%	1.0%
8.3	408	0.3%	0.5%	0.5%	0.7%
10.2	410	0.0%	0.1%	0.1%	0.1%
10.1	510	0.0%	0.2%	0.2%	0.3%
12	412	0.0%	0.1%	0.3%	0.2%
11.1	411	0.0%	0.1%	0.2%	0.2%
11.2	311	0.0%	0.1%	0.1%	0.0%
10.3	310	0.0%	0.1%	0.0%	0.0%
4	404	0.0%	1.1%	1.1%	1.1%

A (PEST_HP, MLS only), B (PESTPP-iES, MLS only), C (PESTPP-iES, MLS and MD)

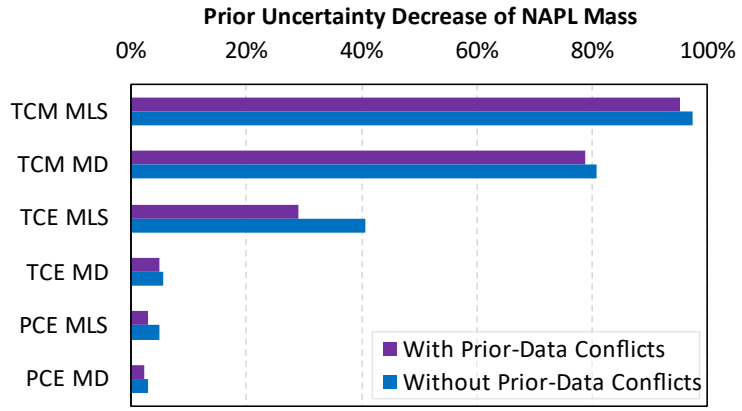

Figure 3-10. Percent worth of monitoring datasets for reducing the prior (pre-calibration) uncertainty of initial source mass. The prior uncertainty was defined on the basis of residual saturation of NAPL zones ranging between 0.05% and 15%, where ~100 % uncertainty reduction was attained by TCM concentrations measured at MLS ports.

An example of the worth of individual MLS and MD measurements for reducing the prior uncertainty of NAPL-zone parameters is presented in Figure 3-11. These results indicated opposite trends in the worth of aqueous-phase concentrations for estimating C_0^N and k_0^N. Maximum concentrations constrained k_0^N parameters, while declining concentrations constrained C_0^N parameters accounting for NAPL mass. This explained why only TCM data significantly reduced the prior uncertainty of NAPL mass, as all MLS ports showed declining TCM concentrations (Figure 3-5). Similarly, ~30% (with PDCs) and ~40% (without PDCs) reductions in the prior uncertainty of NAPL mass by TCE MLS data (Figure 3-10) was attributed to MLS ports with approximately more than 100 g of NAPL mass (e.g., port 508 in Table 3-2 and Figure 3-6) and declining TCE concentrations. Conversely, Table 3-4 indicates parameters with a low RUVR corresponding to deeper NAPL zones accounting for less than 1% of total NAPL mass. The low RUVR values in Table 3-4 were also caused by narrower prior uncertainty bounds compared to those of other NAPL-zone parameters. As shown in Figure 3-11, NAPL zones harboring most of the NAPL mass (e.g., 6.1 and 6.2 in Table 3-3) also benefited from additional C_0^N uncertainty reductions by TCM MD data, highlighting the contribution of those zones to the overall source depletion rates.

Table 3-4. Source zone parameters with lower than 80% prior uncertainty variance reduction.

MLS	NAPL	RUVR (with PDC)		RUVR (without PDC)	
Port	Zone	C_0^N	$k_{TCM,0}^N$	C_0^N	$k_{TCM,0}^N$
605	5.1	65%	> 80%	79%	> 80%
609	9.1	11%	13%	18%	22%
309	9.4	11%	5%	17%	8%
510	10.1	50%	> 80%	67%	> 80%
410	10.2	> 80%	17%	> 80%	18%
310	10.3	12%	15%	18%	15%
311	11.2	7%	1%	28%	1%
NA	$k_{TCE,0}^N$	NA	5%	NA	8%
NA	$k_{PCE,0}^N$	NA	18%	NA	30%

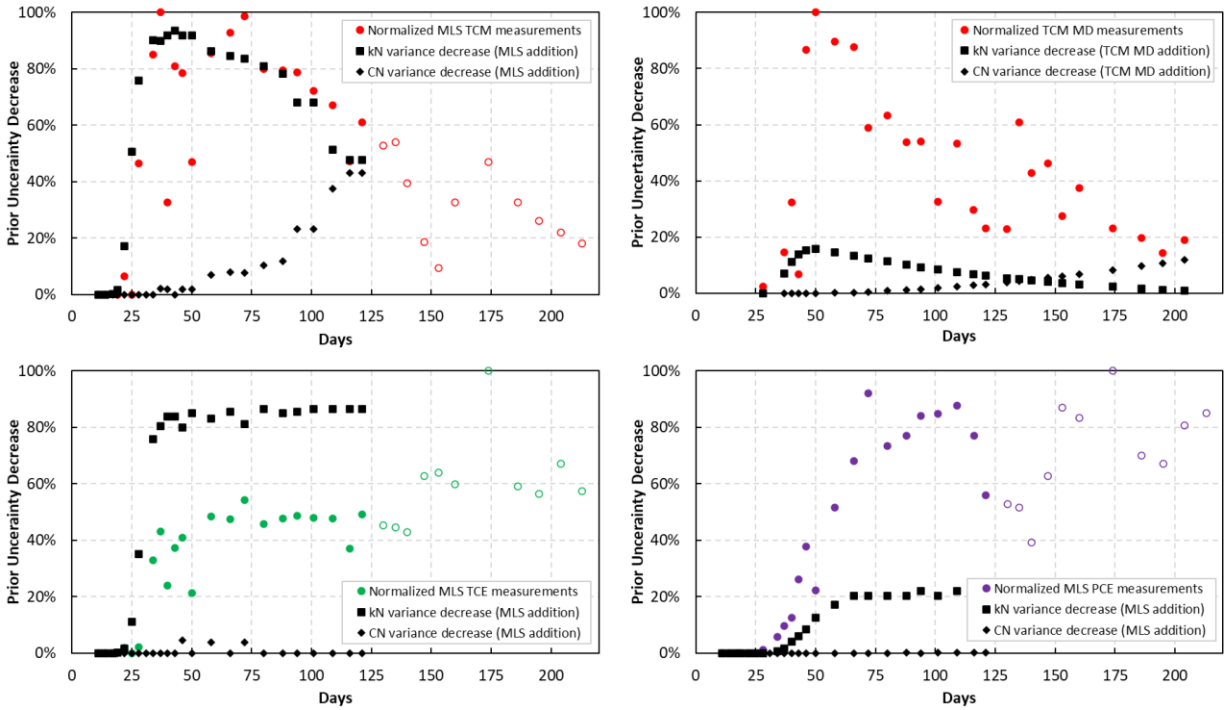

Figure 3-11. Percent worth of individual aqueous-phase concentrations (MLS port 606 and TCM MD) for reducing the prior uncertainty variance of C_0^N and $k_{TCM,0}^N$ of NAPL zone 6.1. Although the same trend of added value by individual measurements was determined for all ports, only NAPL zones containing most of the source mass benefited from additional uncertainty reductions by TCM MD data. In turn, the correspondence between the TCM MD profile with individual MLS ports emphasized the value of multilevel monitoring for estimating NAPL architecture.

Except for parameters listed in Table 3-4, history-matching reduced the prior uncertainty of all NAPL parameters by up to 100%. In contrast to C_0^N parameters constrained by TCM data exclusively, maximum TCE and PCE concentrations also constrained $k_{0,TCM}^N$ parameters (Figure 3-11). However, as indicated in Table 3-4, the prior uncertainty of $k_{0,TCE}^N$ and $k_{0,PCE}^N$ (global $k_{0,TCM}^N$ multipliers) was not reduced, partially because of their narrow prior uncertainty bounds. Yet the small RUVR of these mass transfer parameters was driven by their corresponding MLS datasets (results not shown). Moreover, while the mean values of both multipliers (Table 3-1) were in close agreement with those estimated by Mobile et al. (2012), as $k_{TCE,0}^N$ = 0.96 and $k_{0,PCE}^N$ = 0.85, FOSM analysis with Models A, B, and C suggested that $k_{TCE,0}^N$ could take a value greater than 1, which would not be consistent with previous findings (Mobile et al. 2012) or with mass transfer correlations with component diffusivities (Imhoff et al., 1993; Powers et al., 1992, 1994). As previously discussed, possible explanations for remaining uncertainties on $k_{TCE,0}^N$ and $k_{PCE,0}^N$ could include sub-grid-scale NAPL dissolution behavior, noticeable primarily in TCM MLS data, and/or the influence of grid scale on concentration gradients and $\alpha_{L,T}$ (transverse and longitudinal). Transverse dispersion has been shown to regulate mass transfer rates from DNAPL pools (Hunt & Sitar, 1988, Stewart et al., 2022), requiring an ultrafine grid scale for accurate numerical simulations of DNAPL dissolution (Falta, 2003).

3.8.3. Analysis of DNAPL Mass Depletion

Table 3-5 presents mass balance results of NAPL mass removed by natural dissolution calculated using all models. The percent reductions of initial mass were calculated using the known initial composition values. Despite differences in the estimated source zone architectures, Model C produced nearly identical results as Mobile et al. (2012), emphasizing the importance of constraining NAPL mass for estimating source depletion rates. Conversely, Model A resulted in a 40% reduction of initial NAPL mass, almost doubling Model C results. Model C also indicated a source persistence at the end of the natural dissolution period ~4 and ~2 times lower than indicated by Models A and B, respectively, using PCE as reference. These results reflected the advantage of implementing prior Monte Carlo analyses to understand model deficiencies in relation to the observed system behavior. Additionally, Table 3-5 indicates the amount of NAPL mass eliminated by methanol remediation, calculated by subtracting the NAPL mass remaining in the soil estimated

by Broholm et al. (1999) after conclusion of the experiment, from the remaining mass after 220 days estimated with Model C. Differences in the methanol calculations were linked to post-experiment mass estimated by Broholm et al. (1999) from C_i^N values assuming different S^N values. The obvious impact that such differences would have on remedial designs at hazardous waste sites highlighted difficulties in measuring S^N directly, even by soil confirmatory sampling. These results suggested value in the indirect source characterization method undertaken in this study to estimate and reduce the uncertainty of site-specific mass-transfer parameters, which is critical for effective, risk-based remedial optimizations.

Table 3-5. Mass of NAPL removed.

Data Source	NAPL Mass Removed (kg)				Initial NAPL Mass Reduction (%)			
	TCM	TCE	PCE	Total	TCM	TCE	PCE	Total
Initial (injected)	0.74	2.92	4.04	7.70	0	0	0	0
Model A	0.67	1.46	0.97	3.10	91	50	24	40
Model B	0.63	1.10	0.55	2.28	85	38	14	30
Model C	0.61	0.92	0.25	1.78	82	32	6	23
Mobile et al. (2012)	0.59	0.91	0.24	1.74	80	31	6	23
Methanol flush (1)	0.13	1.47	1.88	3.49	17	50	47	45
Methanol flush (2)	0.13	1.18	0.80	2.11	17	40	20	27

Mass removed by methanol flushing was calculated by subtracting post-experimental NAPL mass remaining in soil estimated by Broholm et al. (1999) with C_i^N values assuming (1) a homogeneous 3.6% S^N in all excavation layers (Figure B-1) and (2) assuming 20% S^N in excavation layer 2 (where a DNAPL pool was observed), from the remaining NAPL mass on day 220 estimated with the posterior base realization of Model C. The percent reductions of initial NAPL mass were calculated with respect to the known initial composition of the mixture.

3.8.4. Limitations and Alternatives

Primary limitations to the indirect source characterization method in this study include availability of long-term monitoring histories, and uncertainty on NAPL depletion stages reflected in monitoring profiles. An alternative to the former involves the field test described by Mobile et al. (2016) to determine mass transfer rate coefficients in situ. This test would induce breakthrough of nonequilibrium concentrations through forced hydraulic gradients and flushing in the source zone, generating monitoring profiles suitable for the inverse modeling techniques applied in this study.

Conversely, situations where available MD data is uncertain with respect to source depletion trends, upscaled, dual-domain models with explicit mass transfer parameters constrained by direct site characterization, provide a viable alternative to estimate source zone depletion behavior (Stewart et al., 2022). Furthermore, sites where natural attenuation mechanisms are significant may benefit from several monitoring transects along the flow direction, differentiating attenuation capacity from NAPL dissolution rates for decision-support modeling (McMillan et al., 2018; Rivett et al., 2014).

3.9. Conclusions

A combination of mass-discharge and depth-discrete groundwater monitoring data allowed for characterizing the mass distribution and dissolution rates of a heterogeneous, multicomponent DNAPL source zone with numerical modeling of mass transfer and transport. Investigating numerical model uncertainties linked the depleting signatures of the most soluble NAPL component and least by volume, TCM, to the accurate quantification of residual NAPL mass. Yet early TCM concentration peaks were identified as drives of model bias through prior Monte Carlo uncertainty analysis. The analysis emphasized several system complexities, including multiscale heterogeneity of source architecture and NAPL dissolution, and NAPL migration during the multicomponent dissolution process, reflected in dissolved-phase concentrations excluded for history-matching to eliminate mass transfer bias. Spatially-varying, component-specific mass transfer rates were thereby constrained by maximum TCM, TCE, and PCE concentrations, attributed to steady-state source zone depletion by data-worth analyses.

In contrast to the soil excavation analyses, coupling numerical modeling with uncertainty analyses in this work proved useful for characterizing NAPL mass and saturation distributions, which cannot be measured directly at field sites and are critical to effective remedial designs. However, despite the availability of high-resolution monitoring data, the source mass depletion exponent β could not be constrained, highlighting the benefit of model uncertainty quantification accounting for all possible scenarios of source zone depletion. Similar predictions of source depletion were also obtained with respect to a previous modeling effort using a different parameterization and parameter estimation strategy. Both methods regularized the inversion process through parsimony

between available multilevel monitoring ports and NAPL-zone parameters, avoiding erroneous estimates and model predictions. In this case, reasonable model predictions were obtained by removing aqueous concentrations representing sub-grid-scale heterogeneity and data noise. Although identifying and removing the latter can benefit any decision-support modeling situation, future research is needed to develop methods capable of constraining grid-scale mass-transfer parameters in the absence of consistent monitoring data.

3.10. Acknowledgements

This study was partially supported by the Environmental Security Technology Certification Program (ESTCP) under Project ER19-5223. The content of this manuscript has not been subject to agency review and does not necessarily represent the view of the sponsoring agency.

3.11. Data Availability Statement

The Groundwater Modeling System (GMS) software hosting the MODFLOW2000 and SEAM3D programs used in this study is available through Aquaveo at https://www.aquaveo.com/software/gms-groundwater-modeling-system-introduction. The PWTADJ2, PREDUNC, GENLINPRED, and PEST_HP programs are available at https://pesthomepage.org/programs. The PESTPP-iES software is available at https://www.usgs.gov/software/pest-software-suite-parameter-estimation-uncertainty-analysis-management-optimization-and (version 5.1.6 was used and the source code is available on https://github.com/usgs/pestpp/releases/tag/5.1.6). Figures 3-5 through 3-7 were produced with the Matplotlib (https://matplotlib.org/) version 3.5.1 and Seaborn (https://seaborn.pydata.org/) version 0.11.2 libraries using the Python programming language. Aqueous-phase concentration data, model input and output files, and Python scripts used for postprocessing output files and for generating figures are archived at https://doi.org/10.7294/22718026.

References

Abriola, L. M. (1989). Modeling Multiphase Migration of Organic Chemicals in Groundwater Systems - A Review and Assessment. *Environmental Health Perspectives, 8*, 117-143. https://doi.org/10.1289/ehp.8983117

Abriola, L. M., Miller, E. L., Pennell, K. D., Ramsburg, A., & Christ, J. A. (2013). *Metric identification and protocol development for characterizing DNAPL source zone architecture and associated plume response.* Alexandria, VA: SERDP Project ER-1612.

Agaoglu, B., Copty, N. K., Scheytt, T., & Hinkelmann, R. (2015). Interphase mass transfer between fluids in subsurface formations: A review. *Advances in Water Resources, 79*, 162-194. https://doi.org/10.1016/j.advwatres.2015.02.009

Arshadi, M., De Paolis Kaluza, M. C., Miller, E. L., & Abriola, L. M. (2020). Subsurface Source Zone Characterization and Uncertainty Quantification Using Discriminative Random Fields. *Water Resources Research*. https://doi.org/10.1029/2019WR026481

Broholm, K., Feenstra, S., & Cherry, J. A. (1999). Solvent Release into a Sandy Aquifer. 1. Overview of Source Distribution and Dissolution Behavior. *Environmental Sicence & Technology, 33*(5), 681-690. https://doi.org/10.1021/es980097d

Broholm, K., Feenstra, S., & Cherry, J. A. (2005). Solvent Release into a Sandy Aquifer. 2. Estimation of DNAPL Mass Based on a Multiple-Component Dissolution Model. *Environmental Science & Technology, 39*(1), 317-324. https://doi.org/10.1021/es0306462

Brusseau, M. L., Matthieu III, D. E., Carroll, K. C., Mainhagu, J., Morrison, C., McMillan, A., . . . Plaschke, M. (2013). Characterizing Long-term Contaminant Mass Discharge and the Relationship Between Reductions in Discharge and Reductions in Mass for DNAPL Source Areas. *Journal of Contaminant Hydrology*, 1-12. https://doi.org/10.1016/j.jconhyd.2013.02.011

Christ, J. A., Ramsburg, A. C., Pennell, K. D., & Abriola, L. M. (2006). Estimating mass discharge from dense nonaqueous phase liquid source zones using upscaled mass transfer coefficients: An evaluation using multiphase numerical simulations. *Water Resources Research, 42*(11). https://doi.org/10.1029/2006WR004886

Christ, J. A., Ramsburg, C. A., Pennell, K. D., & Abriola, L. M. (2010). Predicting DNAPL mass discharge from pool-dominated source zones. *Journal of Contaminant Hydrology, 114*(1-4), 18 - 34. https://doi.org/10.1016/j.jconhyd.2010.02.005

Dekker, T. J., & Abriola, L. M. (2000). The influence of field-scale heterogeneity on the infiltration and entrapment of dense nonaqueous phase liquids in saturated formations. *Journal of Contaminant Hydrology, 42*(2-4), 187-218. https://doi.org/10.1016/S0169-7722(99)00092-3

DiFilippo, E. L., & Brusseau, M. L. (2008). Relationship Between Mass Flux Reduction and Source-Zone Mass Removal: Analysis of Field Data. *Journal of Contaminant Hydrology, 98*(1-2), 22-35. https://doi.org/10.1016/j.jconhyd.2008.02.004

DiFilippo, E. L., & Brusseau, M. L. (2011). Assessment of a Simple Function to Evaluate the Relationship Between Mass Flux Reduction and Mass Removal for Organic-Liquid Contaminated Source Zones. *Journal of Contaminant Hydrology, 123*(3-4), 104-113. https://doi.org/10.1016/j.jconhyd.2010.12.011

Doherty, J. (2015). *Calibration and Uncertainty Analysis for Complex Environmental Models.* Brisbane, Australia: Watermark Numerical Computing.

Doherty, J. (2020). *PEST_HP. PEST for highly parallelized computing environments.* Watermark Numerical Computing. Retrieved from https://pesthomepage.org/documentation

Doherty, J., & Moore, C. (2020). Decision Support Modeling: Data Assimilation, Uncertainty Quantification, and Strategic Abstraction. *Groundwater, 58*(3), 327-337. https://doi.org/10.1111/gwat.12969

Engelmann, C., Handel, F., Binder, M., Yadav, P. K., Dietrich, P., Liedl, R., & Walther, M. (2019). The fate of DNAPL contaminants in non-consolidated subsurface systems – Discussion on the relevance of effective source zone geometries for plume propagation. *Journal of Hazardous Materials, 375*, 233-240. https://doi.org/doi.org/10.1016/j.jhazmat.2019.04.083

Falta, R. (2003). Modeling sub-grid-block-scale dense nonaqueous phase liquid (DNAPL) pool dissolution using a dual-domain approach. *Water Resources Research, 39*(12). https://doi.org/10.1029/2003WR002351

Falta, R. W., Rao, S. P., & Basu, N. (2005a). Assessing the impacts of partial mass depletion in DNAPL source zones I. Analytical modeling of source strength functions and plume response. *Journal of Contaminant Hydrology*, 259-280. https://doi.org/0.1016/j.jconhyd.2005.05.010

Falta, R. W., Basu, N., & Rao, S. P. (2005b). Assessing impacts of partial mass depletion in DNAPL source zones: II. Coupling source strength functions to plume evolution. *Journal of Contaminant Hydrology*, 45-66. https://doi.org/10.1016/j.jconhyd.2005.05.012

Frind, E. O., Molson, J. W., & Schirmer, M. (1999). Dissolution and mass transfer of multiple organics under field conditions: The Borden emplaced source. *Water Resources Research, 35*(3), 683-694. https://doi.org/10.1029/1998WR900064

Geller, J. T., & Hunt, J. R. (1993). Mass Transfer From Nonaqueous Phase organic Liquids in Water-Saturated Porous Media. *Water Resources Research, 29*(4), 883-845. https://doi.org/10.1029/92WR02581

Guo, Z., Russo, A. E., DiFilippo, E. L., Zhang, Z., Zheng, C., & Brusseau, M. L. (2020). Mathematical modeling of organic liquid dissolution in heterogeneous source zones. *Journal of Contaminant Hydrology, 235*. https://doi.org/10.1016/j.jconhyd.2020.103716

Harbaugh, A. W., Banta, E. R., Hill, M. C., & McDonald, M. G. (2000). *MODFLOW-2000, The U.S. Geological Survey Modular Ground-Water Model: User Guide to Modularization Concepts and the Ground-Water Flow Process.* Reston, Virginia: U.S. Geological Survey. https://doi.org/10.3133/ofr200092

Hunt, J. R., & Sitar, N. (1988). Nonaqueous Phase Liquid Transpot and Cleanup 1. Analysis of Mechanisms. *Water Resources Research, 24*(8), 1247-1258. https://doi.org/10.1029/WR024i008p01247

Imhoff, P. T., Jaffe, P. R., & Pinder, G. F. (1993). An experimental study of complete dissolution of a nonaqueous phase liquid in saturated porous media. *Water Resources Research, 30*(2), 307-320. https://doi.org/10.1029/93WR02675

Kang, X., Kokkinaki, A., Kitandis, P. K., Shi, X., Lee, J., Mo, S., & Wu, J. (2021a). Hydrogeophysical Characterization of Nonstationary DNAPL Source Zones by Integrating a Convolutional Variational Autoencoder and Ensemble Smoother. *Water Resources Research, 57*(1). https://doi.org/10.1029/2020WR028538

Kang, X., Kokkinaki, A., Power, C., Kitandis, P. K., Shi, X., Duan, L., . . . Wu, J. (2021b). Integrating deep learning-based data assimilation and hydrogeophysical data for improved monitoring of DNAPL source zones during remediation. *Journal of Hydrology, 601*, 126655. https://doi.org/10.1016/j.jhydrol.2021.126655

Koch, J., & Nowak, W. (2015). Predicting DNAPL mass discharge and contaminated site longevity probabilities: Conceptual model and high-resolution stochastic simulation. *Water Resources Research, 51*(2), 806 - 831. https://doi.org/10.1002/2014WR015478.

Koch, J., & Nowak, W. (2016). Identification of contaminant source architectures—A statistical inversion that emulates multiphase physics in a computationally practicable manner. *Water Resources Research, 52*, 1009–1025. https://doi.org/10.1002/2015WR017894

Kokkinaki, A., O'Carroll, M., Werth, C. J., & Sleep, B. E. (2013). Coupled simulation of DNAPL infiltration and dissolution in three-dimensional heterogeneous domains: Process model validation. *Water Resources Research, 49*, 7023-7036. https://doi.org/10.1002/wrcr.20503, 2013

Kokkinaki, A., Werth, C. J., & Sleep, B. E. (2014). Comparison of upscaled models for multistage mass discharge from DNAPL source zones. *Water Resources Research*, 3187 - 3205. https://doi.org/10.1002/2013WR014663

Kueper, B. H., Stroo, H. F., Vogel, C. M., & Ward, C. H. (2014). *Chlorinated Solvent Source Zone Remediation.* Springer New York. https://doi.org/10.1007/978-1-4614-6922-3

Luciano, A., Mancini, G., Torreta, V., & Viotti, P. (2018). An empirical model for the evaluation of the dissolution rate from a DNAPL-contaminated area. *Environmental Science and Pollution Research*, 33992-34004. https://doi.org/10.1007/s11356-018-3193-6

Mackay, D. M., Freyberg, D. L., & Roberts, P. V. (1986). A Natural Gradient Experiment on Solute Transport in a Sand Aquifer: 1. Approach and Overview of Plume Movement. *Water Resources Research, 22*(13), 2017-2029. https://doi.org/10.1029/WR022i013p02017

Marble, J. C., DiFilippo, E. L., Zhang, Z., Tick, G. R., & Brusseau, M. L. (2008). Application of a lumped-process mathematical model to dissolution of non-uniformly distributed

immiscible liquid in heterogeneous porous media. *Journal of Contaminant Hydrology, 100*, 1-10. https://doi.org/10.1016/j.jconhyd.2008.04.003

Mayer, A. S., & Hassanizadeh, M. S. (2005). *Soil and Groundwater Contamination: Nonaqueous Phase Liquids–Principles and Observations.* Washington, D.C.: American Geophysical Union.

McMillan, L. A., Rivett, M. O., Wealthall, G. P., Zeeb, P., & Dumble, P. (2018). Monitoring well utility in a heterogeneous DNAPL source zone area: Insights from proximal multilevel sampler wells and sampling capture-zone modelling. *Journal of Contaminant Hydrology, 210*, 15-30. https://doi.org/10.1016/j.jconhyd.2018.02.001

Miller, C. T., Christakos, G., Imhoff, P. T., McBride, J. F., & Pedit, J. A. (1998). Multiphase flow and transport modeling in heterogeneous porous media: challenges and approaches. *Advances in Water Resources, 21*(2), 77-120. https://doi.org/10.1016/S0309-1708(96)00036-X

Mobile, M. A., Widdowson, M. A., & Gallagher, D. L. (2012). Multicomponent NAPL Source Dissolution: Evaluation of Mass-Transfer Coefficients. *Environmental Science & Technology, 46*(18), 10047-10054. https://doi.org/10.1021/es301076p

Mobile, M., Widdowson, M., Stewart, L., Nyman, J., Deeb, R., Kavanaugh, M., . . . Gallagher, D. (2016). In-situ determination of field-scale NAPL mass transfer coefficients: Performance, simulation and analysis. *Journal of Contaminant Hydrology, 187*, 31-46. https://doi.org/10.1016/j.jconhyd.2016.01.010

National Research Council. (2005). *Contaminants in the subsurface: Source zone assessment and remediation.* Washington, D.C.: The National Academic Press.

Park, E., & Parker, J. C. (2005). Evaluation of an upscaled model for DNAPL dissolution kinetics in heterogeneous aquifers. *Advances in Water Resources, 28*(12), 1280-1291. https://doi.org/10.1016/j.advwatres.2005.04.002

Parker, J. C., & Park, E. (2004). Modeling field-scale dense nonaqueous phase liquid dissolution kinetics in heterogeneous aquifers. *Water Resources Research, 40*(5). https://doi.org/10.1029/2003WR002807

Powers, S. E., Abriola, L. M., & Weber Jr, W. J. (1992). An Experimental Investigation of Nonaqueous Phase Liquid Dissolution in Saturated Subsurface Systems: Steady State Mass Transfer Rates. *Water Resources Research, 28*(10), 2691-2705. https://doi.org/10.1029/92WR00984

Powers, S. E., Abriola, L. M., & Weber, W. J. (1994). An experimental investigation of nonaqueous phase liquid dissolution in saturated systems: Transient mass transfer rates. *Water Resources Research, 30*(2), 321-332. https://doi.org/10.1029/93WR02923

Prieto Estrada, Andres (2023): Numerical Modeling and Data-Worth Analysis for Characterizing the Architecture and Dissolution Rates of a Multicomponent DNAPL Source [Dataset]. University Libraries, Virginia Tech. https://doi.org/10.7294/22718026

Rivett, M. O., & Feenstra, S. (2005). Dissolution of an Emplaced Source of DNAPL in a Natural Aquifer Setting. *Environmental Science & Technology, 39*, 447-455. https://doi.org/10.1021/es040016f

Rivett, M. O., Dearden, R. A., & Wealthall, G. P. (2014). Architecture, persistence and dissolution of a 20 to 45 year old trichloroethene DNAPL source zone. *Journal of Contaminant Hydrology, 170*, 95-115. https://doi.org/10.1016/j.jconhyd.2014.09.008

Rivett, M. O., Feenstra, S., & Cherry, J. A. (2001). A controlled field experiment on groundwater contamination by a multicomponent DNAPL: creation of the emplaced-source and overview of dissolved plume development. *Journal of Contaminant Hydrology, 49*, 111-149.

Saenton, S., & Illangasekare, T. H. (2004). Determination of DNAPL entrapment architecture using experimentally validated numerical codes and inverse modeling. *Developments in Water Science, 55*, 767-778. https://doi.org/10.1016/S0167-5648(04)80098-4

Saenton, S., & Illangasekare, T. H. (2007). Upscaling of mass transfer rate coefficient for the numerical simulation of dense nonaqueous phase liquid dissolution in heterogeneous aquifers. *Water Resources Research, 43*(2). https://doi.org/10.1029/2005WR004274

Soerens, T. S., Sabatini, D. A., & Harwell, J. H. (1998). Effects of flow bypassing and nonuniform NAPL distribution on the mass transfer characteristics of NAPL dissolution. *Water Resources Research, 34*(7), 1657-1673. https://doi.org/10.1029/98WR00554

Stewart, L. D., Chambon, J. C., Widdowson, M. A., & Kavanaugh, M. C. (2022). Upscaled modeling of complex DNAPL dissolution. *Journal of Contaminant Hydrology, 244*. https://doi.org/10.1016/j.jconhyd.2021.103920

Waddill, D. W., & Widdowson, M. A. (2000). *SEAM3D: A numerical model for three-dimensional solute transport and sequential electron acceptor-based bioremediation in groundwater*. ERDC/EL TR- 00-18. U.S. Army Engineer Research and Development Center, Vicksburg, MS.

Watermark Numerical Computing. (2018). *Model-Independent Parameter Estimation. User Manual Part II: PEST Utility Suport Software.* Retrieved from https://pesthomepage.org/documentation

White, J. T. (2018). A model-independent iterative ensemble smoother for efficient history-matching and uncertainty quantification in very high dimensions. *Environmental Modelling & Software, 109*, 191-201. https://doi.org/doi.org/10.1016/j.envsoft.2018.06.009

White, J. T., Hemmings, B., Fienen, M. N., & Knowling, M. J. (2021). Towards improved environmental modeling outcomes: Enabling low-cost access to high-dimensional, geostatistical-based decision-support analyses. *Environmental Modelling and Software, 139*, 105022. https://doi.org/10.1016/j.envsoft.2021.105022

White, J., Hunt, R., Fienen, M., & Doherty, J. (2020). *Approaches to Highly Parameterized Inversion: PEST++ Version 5, a Software Suite for Parameter Estimation, Uncertainty Analysis, Management Optimization and Sensitivity Analysis.* Reston, VA: U.S. Geological Survey. https://doi.org/10.3133/tm7C26

Yang, L., Wang, X., Mendoza-Sanchez, I., & Abriola, L. M. (2018). Modeling the influence of coupled mass transfer processes on mass flux downgradient of heterogeneous DNAPL source zones. *Journal of Contaminant Hydrology, 211*, 1-14. https://doi.org/10.1016/j.jconhyd.2018.02.003

Zhu, J., & Skyes, J. (2004). Simple screening models of NAPL dissolution in the subsurface. *Journal of Contaminant Hydrology, 72*(1-4), 245-258. https://doi.org/10.1016/j.jconhyd.2003.11.002

Chapter 4. Scaling of DNAPL Dissolution Rates: Numerical Modeling Analyses

Andres E. Prieto-Estrada[1], Mark A. Widdowson[1], and Lloyd D. Stewart[2]

[1] The Charles E. Via, Jr. Department of Civil and Environmental Engineering, Virginia Tech, Blacksburg, Virginia 24061-0105, United States

[2] Praxis Environmental Technologies, Inc., 1440 Rollins Road, Burlingame, California 94010, United States

Corresponding author, e-mail address: mwiddows@vt.edu (M.A. Widdowson)

4.1. Key Points

- Source zone architectural dimensions and numerical grid resolutions were correlated for scaling bulk DNAPL dissolution rates
- Increasing vertical grid resolution decreased mass transfer coefficient sensitivity, incurring non-unique estimates of DNAPL depletion
- Scaled mass transfer coefficients replicated effluent histories and physical predictions of DNAPL depletion at multiple grid resolutions

4.2. Abstract

Modeling the dissolution of dense non-aqueous phase liquids (DNAPLs) in groundwater for environmental management support is limited by data availability, inadequate mass transfer assumptions, and/or computational efficiency. A practical volume-averaging (VA) system capable of estimating DNAPL dissolution with a physical basis was leveraged to obtain grid-scale mass transfer parameters using SEAM3D, a numerical biodegradation and transport simulator. The dissolution of DNAPL pools documented by effluent monitoring in flow-cell experiments was simulated a priori with the VA model, translating initial source zone characteristics into upscaled mass transfer coefficients. A discretized mass transfer function was used to evaluate relationships between 1D and 2D numerical grid resolutions and source mass depletion results with respect to

VA physical predictions. Comparative analyses revealed an empirical relationship for approximating VA simulations with SEAM3D by scaling mass transfer coefficients to grid resolutions. Both inverse and forward numerical results showed decreasing sensitivity of mass transfer parameters to effluent profiles with increasing source-zone vertical discretization, regulated by vertical dispersive transport across DNAPL grid blocks. Similarities in grid-resolution effects were observed despite differences in magnitude of source characteristic dimensions, model layer thicknesses, and magnitude of vertical transfer dispersivity coefficients between experiments. In addition to history-matching of effluent data, the scaling analysis proved beneficial for constraining the uncertainty of mass transfer coefficients and source mass depletion estimates in numerical models of DNAPL dissolution and aqueous-phase transport.

4.3. Plain Language Summary

Practical and effective modeling methods can inform restoration efforts of groundwater contaminated by source zones of immiscible liquids, such as dense chlorinated solvents. Yet environmental managers typically rely on remediation performance monitoring with limited quantitative interpretation, often resulting in costly and ineffective site cleanup strategies. Our work merged a spatially-averaged, computationally-efficient physical model of source zone contaminant discharge with numerical modeling of groundwater flow and contaminant transport. Simulations of flow-cell experiments documenting contaminant dissolution rates allowed us to explore relationships between source zone discretization and long-term dissolution variability. Deterministic numerical analyses were complemented by inverse modeling of monitoring profiles, which did not yield unique parameter estimates as vertical discretization was increased. The resulting methodology leveraged the spatially-averaged model to constrain predictive uncertainties of long-term contaminant dissolution with numerical modeling of contaminant transport in groundwater.

4.4. Keywords

Source zone architecture, DNAPL dissolution, numerical flow and transport modeling, scaling method, bulk mass transfer coefficient, numerical grid resolution

4.5. Introduction

Groundwater contamination by spills of dense non-aqueous phase liquids (DNAPLs) can persist long term because of mass transfer limitations, which may be estimated with mathematical modeling for environmental management support (Mayer & Hassanizadeh, 2005; Kueper et al., 2014; Agaoglu et al., 2015). However, estimating mass transfer rates requires an adequate mathematical representation of contributing processes, including the interplay between DNAPL saturation and hydraulic accessibility to groundwater flow (Miller et al., 1998a, 1998b; Kokkinaki et al., 2014). Because representing these processes with pore-scale numerical models and typical data limitations is highly impractical (Falta, 2003; Engelmann et al., 2019), upscaled modeling methods have been developed to account for physical mass transfer processes within a contaminated aquifer volume, i.e., a DNAPL source zone (Parker & Park, 2004; Christ et al., 2006; 2010). Provided with source characterization data, upscaled process models can readily predict average mass transfer rates, which can be estimated along with residual saturations at multiple scales of spatial resolution with inverse numerical modeling of monitoring data (NRC, 2005; Mobile et al., 2012; Stewart et al., 2022; Prieto-Estrada et al., 2022b). Although coupling mass transfer and transport models can support decision-making at contaminated sites (Falta et al., 2005a, 2005b; Liu et al., 2014), the simulation of aqueous transport across numerical grid blocks introduces additional uncertainties on the scaling of effective mass transfer coefficients (Parker & Park, 2005; Fernandez-Garcia et al., 2009; Leung & Srinivasan, 2016; Zhang et al., 2021).

Field-scale rates of DNAPL mass transfer are primarily governed by the distribution of residual saturation in the subsurface, referred to as the source zone architecture (Lemke & Abriola, 2006; DiFilippo & Brusseau, 2008, 2011; Brusseau et al., 2013). The source zone architecture is controlled by subsurface geological heterogeneity, governing DNAPL migration pathways and entrapment within aquifers (Dekker & Abriola, 2000). Hydraulic accessibility to groundwater flow through and around DNAPL mass accumulations limits dissolution rates, resulting in nonequilibrium discharge concentrations typically observed in monitoring systems (Frind et al., 1999; Park & Parker, 2005; Rivett & Feensta, 2005; Rivett et al., 2014; McMillan et al., 2018). Monitoring profiles exhibiting multistage and nonmonotonic dissolution trends reflect gradual changes in source zone architecture, primarily comprised by low-saturation ganglia and high-

saturation DNAPL pools (Brusseau et al., 2013; Kokkinaki et al., 2014; Stewart et al., 2022). Rather than representing geological heterogeneities in detail, upscaled models of DNAPL dissolution account for gradual changes in source architectural characteristics by incorporating implicit or explicit mass transfer relationships (Parker & Park, 2004; Stewart et al., 2020). The former approach can benefit from high-resolution site characterization (HRSC), including dye-enhanced laser induced fluorescence (dye-LIF) for delineating chlorinated solvents (Horst et al., 2018), hydraulic profiling tool (HPT) for discrete aquifer hydraulic mapping, soil confirmatory sampling, and partitioning or push-pull tracer tests for estimating local saturations (Basu et al., 2008; Huang et al., 2010; Stewart et al., 2022; Prieto-Estrada et al., 2023a). An alternative upscaled modeling approach simplifies source architectural characteristics through best-fit mass transfer coefficients estimated from downgradient monitoring data (Marble et al., 2008; Guo et al., 2020).

Upscaled models of DNAPL dissolution may incorporate scale-dependent, lumped-process mass transfer coefficients estimated inversely from monitoring data (Parker & Park, 2005; Mobile et al., 2012; 2016). However, their predictive capability may be biased by the monitoring profiles used for parameter estimation (Parker et al., 2010; Prieto-Estrada et al., 2023b). For example, early in the life cycle of a DNAPL source zone, the contributions of slowly dissolving pools governing complete depletion may not be discernible in mass discharge data (Abriola et al., 2013). In contrast, upscaled models incorporating source architectural parameters can leverage both HRSC and monitoring data to constrain the explicit estimation of mass transfer coefficients (Stewart et al., 2022; Prieto-Estrada et al., 2023a). Examples include an upscaled Gilland-Sherwood correlation and the dual-domain ganglia-to-pool (GTP) mass ratio model (Christ et al., 2006, 2010; Saenton & Illangasekare, 2007). However, these upscaled correlation models have impractical data requirements on residual saturation distributions and neglect vertical dispersivity as a mass transfer component, which has been shown critical for regulating DNAPL pool dissolution and source zone longevity at multiple dimensional scales (Eberhardt & Grathwohl, 2002; Falta, 2003; Carey et al., 2014; Klemm et al., 2021; Stewart et al., 2022). Stewart et al. (2022) developed a volume-averaged (VA) model for NAPL source zone that accounts for dispersive and through-flow mass transfer mechanisms and demonstrated applicability accurately reproducing complex DNAPL dissolution profiles monitored in laboratory, numerical, and field experiments through. The VA model is designed to assimilate HRSC and monitoring data to parameterization of characteristic dimensions

of source zones and estimate timeframes of source zone depletion with computational efficiency and a physical mass transfer basis.

A practical advantage of the VA modeling approach is that detailed saturation and grain-size distributions, and geostatistical modeling are not required for testing site conceptual assumptions to readily estimate source mass fluxes and quantify predictive uncertainties. Instead, the VA model accounts for multi-rate and nonmonotonic dissolution processes on the basis of source-zone characteristic dimensions and the relative location of DNAPL masses along groundwater flow paths (Stewart et al., 2022). Moreover, unlike pore-scale numerical models relying on dispersive transport for simulating DNAPL dissolution assuming local equilibrium (see Miller et al., 1998 and Agaoglu et al., 2015 for reviews), the VA model incorporates transverse vertical dispersivity into an analytical expression for pool dissolution (see derivations by Hunt et al., 1988 and Johnson & Pankow, 1992). While this VA mass transfer parameter can be constrained by characterization methods, such as push-pull tracer tests and borehole lithologic analyses (Huang et al., 2010; Carey et al., 2018), numerical models incorporating lumped-process parameters are advantageous for leveraging multilevel monitoring data to simultaneously characterize the architecture and dissolution rates of heterogenous source zones (Mobile et al., 2012; Prieto-Estrada et al., 2023b).

Although using a single-cell mass transfer function for numerical modeling may be consistent with upscaled DNAPL dissolution theory (Hunt et al., 1998; Johnson & Pankow, 1992), discretizing a source zone may introduce dissolution inconsistencies by simulating aqueous-phase transport across DNAPL grid blocks (Falta, 2003; Park & Parker, 2005). Such grid resolution effects would be particularly relevant to modeling DNAPL pool dissolution, as vertical transverse hydrodynamic dispersion is the primary mass transfer mechanism (Stewart et al., 2022), and is also included in multidimensional numerical transport simulations (Zheng & Bennett, 2002). Therefore, adapting a VA model to a discretized domain requires a methodology accounting for the regulating effect of dispersive transport simulation on effective mass transfer coefficients at the grid block scale (Park & Parker, 2005; Saenton & Illangasekare, 2007; Leung & Srinivasan, 2016; Zhang et al., 2021). Investigating relationships between grid resolution and DNAPL dissolution variability would thereby allow for leveraging the VA physical basis to constrain the uncertainty of lumped-process parameters (e.g., Mobile et al. 2012; Prieto-Estrada et al., 2023), supporting the inverse

characterization of source zones with monitoring data (Stroo et al., 2012; Rivett et al., 2014; Eniarson et al., 2018; McMillan et al., 2018).

Our primary objective was to devise a methodology for simulating DNAPL dissolution with VA mass transfer coefficients scaled to match numerical grid resolutions. The modeling analyses were focused on the dissolution of DNAPL pools because studies have shown that these architectural features govern source zone longevity through kinetic mass transfer at multiple scales. Bench- and intermediate-scale laboratory flow-cell DNAPL dissolution experiments were simulated with the VA model by parameterizing known, initial source zone properties into bulk mass transfer coefficients to replicate monitored TCE and PCE effluent mass discharge profiles, respectively. Because of the VA model capability to estimate DNAPL discharge concentrations without effluent history-matching, VA projections for attaining a target concentration level, referred to as Time of Remediation (TOR), served as comparison metrics to determine equivalent VA and numerical simulation results. Numerical mass transfer and transport models were designed to represent the architectural dimensions of the experimental source zones with different grid resolutions. The flow-cell experiments were constructed using 1D single-cell upscaled DNAPL block models and 2D models using systemically finer horizontal and vertical discretization. Source zone discretization in the downgradient (1D and 2D models) and vertical directions (2D models only) were designed to examine the how aqueous transport across pool zones impacts mass discharge at various grid resolutions. Both the downgradient and vertical discretization dimensions replaced the source zone characteristic dimensions in the VA mass transfer coefficients, in order to identify grid-architecture correlations for scaling estimable bulk mass transfer coefficients and matching effluent profiles at any grid resolution. Forward modeling analyses were complemented by the inverse estimation of scale-dependent, lumped-process mas transfer coefficients, providing additional insights on a scaling methodology. Comparative numerical analyses included transverse vertical dispersivity coefficients in both aqueous-phase transport and mass transfer to evaluate the contribution of both mechanisms to DNAPL pool dissolution in discretized domains.

4.6. Numerical and Volume-Averaged Modeling of DNAPL Dissolution

Interphase mass transfer was represented in this work by a linear driving force relating the single component DNAPL dissolution rate J [M T^{-1} L^{-3}] to the local aqueous phase concentration C [M L^{-3}] averaged within a source zone reference volume [L^3]:

$$J = k^N (C^{sol} - C) \tag{4-1}$$

where k^N [T^{-1}] is a time-varying, bulk mass transfer coefficient and C^{sol} [M L^{-3}] is the aqueous solubility of the DNAPL. Numerical modeling was undertaken with SEAM3D (Waddill & Widdowson, 2000), coupling Equation 4-1 to the following relationship representing DNAPL dissolution from the soil medium into the aqueous phase:

$$J = -\rho_b \frac{dC^N}{dt} \tag{4-2}$$

where ρ_b [M L^{-3}] is the bulk density of the soil and C^N [M M^{-1}] is the DNAPL mass per unit mass of dry soil. A modified version of SEAM3D incorporates the upscaled DNAPL dissolution model developed by Parker and Park (2004) to simulate transient mass transfer:

$$k^{S3D} = k_0^{S3D} \left(\frac{q}{K}\right)^{\alpha} \left(\frac{M(t)}{M_0}\right)^{\beta} \tag{4-3}$$

where k_0^{S3D} is the initial mass transfer coefficient [T^{-1}], q is the Darcy velocity [L T^{-1}], K is the hydraulic conductivity [L T^{-1}], $M(t)/M_0$ is the transient ratio of DNAPL mass [M M^{-1}], and α and β are dimensionless empirical parameters. Previous investigations have reported a linear relationship between k^{S3D} and q, with α = 1 for source zones comprised of heterogeneous media (Parker & Park, 2004; Park & Parker, 2005). Here, the α parameter was set to 0 in all numerical simulations in order to parameterize k_0^{S3D} values using the VA mass transfer concepts, defined below. The transient mass ratio raised to the empirical depletion exponent β represents a gradual reduction of DNAPL/water interfacial areas, regulating dissolution tailing as the source mass is

depleted (Parker & Park, 2004; Stewart et al., 2022). The β parameter was fixed at 0.5 in all models, representing a theoretical value associated with tailing of DNAPL pool dissolution (Stewart et al., 2022).

Transient dissolution of a single DNAPL accumulation, defined as a volume of relative uniformity in saturation, can be simulated by coupling Equation 4-1 to a generalized mass transfer function (Stewart et al., 2022):

$$k_a^{VA} = \frac{q}{V_S}\left[A_{a,yz}k_r(M_a) + A_{a,xy}\sqrt{\frac{4\alpha_T}{\pi X_a}}\right]\left(\frac{M_a(t)}{M_{a,0}}\right)^{\beta} \tag{4-4}$$

where interphase mass transfer (k_a^{VA}) from an individual DNAPL accumulation *"a"* is upscaled by q with respect to a source zone reference volume V_S, which may contain multiple DNAPL accumulations (Figure 4-1). The first term inside the bracket represents dissolution attributable to through flow, which is proportional to the projected area facing flow ($A_{a,yz}$) of "a". Flow through "a" is regulated by the soil relative permeability (k_r) which gradually increases the dissolution rate as the DNAPL volume is reduced. The second term represents dissolution attributable to mechanical dispersion into bypassing flow, which is proportional to the hydrodynamic transverse vertical dispersivity (α_T) around "a" and its horizontal area ($A_{a,xy}$). Dissolution of low DNAPL saturations (ganglia) is dominated by flow through, while dissolution of high-saturation zones (pools) are dominated by dispersion. Theoretically, β = 2/3 for ganglia-dominated accumulations and β = ½ for pool-dominated accumulations, but may be adjusted within a relative narrow range to allow for deviations of mass transfer assumptions such as nonuniformity in the DNAPL saturation (Stewart et al., 2022).

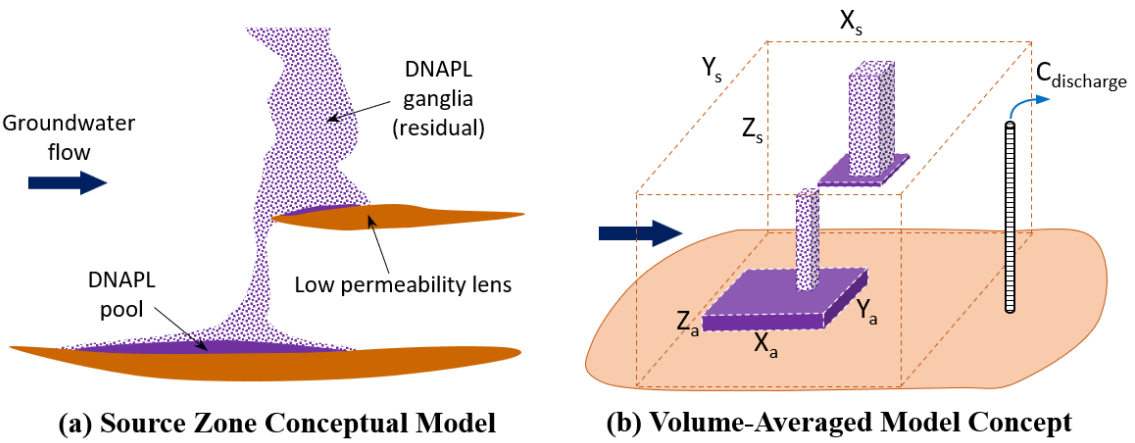

Figure 4-1. (a) Conceptual and (b) Volume-Averaged Model representation of a DNAPL source zone, where the dissolution of four distinct DNAPL accumulations are upscaled by a source-zone reference volume (V_S) to yield the average source discharge concentration. Adapted from Stewart et al. (2022).

4.7. Applications of DNAPL Dissolution Modeling

Previous work by Stewart et al. (2022) and Prieto-Estrada et al. (2023a) demonstrated the ability of the VA model to reproduce complex DNAPL dissolution trends without undertaking history matching. Thus, the VA model is useful for translating site conceptual assumptions into mass transfer coefficients, while history matching of monitoring profiles can further constrain critical parameters such as DNAPL mass and α_T. Both of these parameters govern the longevity of source zones when pertaining to high-saturation DNAPL accumulations, i.e., pool-dominated zones (Stewart et al., 2022; Prieto-Estrada et al., 2023a). Because previous studies have shown ganglia dissolution to be a largely equilibrium process with a negligible contribution to source zone lifespans in the presence of pools (Frind et al., 1999; Rivet et al., 2005; Abriola et al., 2013), the focus of this study was on simulating DNAPL pool dissolution using VA mass transfer coefficients scaled to discretized domains. Two laboratory experiments of DNAPL dissolution with order-of-magnitude differences in source-zone depletion time and dimensional scales provided reference datasets for comparative mass transfer analyses. The datasets yielded a correlation of numerical and VA modeling results as a function of architecture dimensions and grid resolution. Results obtained with downscaled mass transfer coefficients were also contrasted with inverse numerical modeling results.

4.7.1. Flow-Cell Experiments

A bench-scale flow-cell experiment conducted by DiFilippo et al. (2010) consisted of a "mixed" source zone architecture developed within a uniform pack of sand (40/50 mesh) with a 2-cm thick capillary barrier along the bottom of the cell (Figure 4-2). An injection of ~12 mL of trichloroethylene (TCE) at the top of the test cell followed by a 48-hour rest period generated a stable source zone architecture consisting of a vertical ganglia zone underlain by a pool prior to flow initiation. The DNAPL saturation distribution was characterized using a light reflection visualization (LRV) method and TCE effluent concentrations were monitored until source mass depletion. The effluent concentrations were simulated in Stewart et al. (2022) by parameterizing source architectural dimensions into VA mass transfer coefficients. Our analyses focused on the pool zone architecture and its mass dissolution following depletion of the low-saturation ganglia zone, initially hosting ~58% of the injected TCE mass (Stewart et al., 2022). The experiment authors estimated a 59% of initial TCE mass removal after 3.2 days of monitoring, primarily attributed to ganglia dissolution by LRV saturation imaging (DiFilippo et al., 2010). The characteristic pool dissolution signature used in this study included the effluent data recorded after 4.4 days of monitoring.

An intermediate-scale flow-cell experiment conducted by MacKinnon and Thomson (2002) consisted of a DNAPL pool developed in a physical aquifer model consisting of silica sand above a capillary barrier (d_{60} of 0.149 mm, and d_{10} of 0.0085 mm) comprised of silica flour mixed with deionized water to a putty-like consistency (Figure 4-3). An injection of ~1,257 g of dyed tetrachloroethylene (PCE) through five equally spaced glass tubes placed 2 cm above the silica flour base generated a continuous DNAPL accumulation. Water flow through the model was stopped prior to PCE emplacement until 35 days after, allowing for PCE redistribution, which was characterized by soil core data. Water flushing was maintained through the test cell for 90 days prior to a permanganate oxidation flush and resumed 150 days post oxidation. Effluent concentrations were monitored before and after the oxidant flush (MacKinnon & Thomson, 2002).

4.7.2. Volume-Averaged Modeling of Flow-Cell Experiments

Herein, the subscript "*a*" defined in Equation 4-4 for a generalized DNAPL *accumulation* is replaced by the subscript "*p*", for DNAPL *pool*. Likewise, the subscript "0" designates *initial conditions*. Table 4-1 lists the VA model parameters representing initial DNAPL pool and source zone properties used to simulate the flow-cell experiments. The DNAPL pool of the mixed source architecture experiment by DiFilippo et al. (2010) was referred to as "Pool 1", whereas the MacKinnon experiment was referred to as "Pool 2". Figure 4-2 illustrates how the DNAPL architecture and source zone dimensions of Pool 1 were used to estimate mass transfer coefficients a priori. The saturation (S_p^N) of the DNAPL pool was calculated as:

$$S_p^N = \frac{M_p}{V_p \theta \rho^N} \tag{4-5}$$

where M_p is DNAPL mass [M], V_p is volume [L^3] of uniform S_p^N, θ is porosity, and ρ^N is DNAPL density [m L^{-3}]. Relative permeability (k_r) was calculated assuming an irreducible water saturation of 0.15 using the Wyllie correlation (Wyllie, 1962; Stewart et al., 2022):

$$k_r(M_p) = \left(\frac{1 - S_p^N - S_{irr}}{1 - S_{irr}}\right)^3 \tag{4-6}$$

Table 4-1. Source-zone and DNAPL parameters of flow-cell experiments representing initial system conditions.

Parameter	Pool 1	Source	Pool 2	Source
α_T (cm)	0.1	Stewart et al. (2022)	0.04	Estimated
θ	0.45	DiFilippo et al. (2010)	0.41	MacKinnon and Thomson (2002)
q (cm/d)	97.57	DiFilippo et al. (2010)	8.53	MacKinnon and Thomson (2002)
X_S (cm)	22	Equal to X_p	230	Equal to X_p
Y_S (cm)	2.54	Stewart et al. (2022)	15	MacKinnon and Thomson (2002)
Z_S (cm)	19	DiFilippo et al. (2010)	45	MacKinnon and Thomson (2002)
X_p (cm)	22	Stewart et al. (2022)	230	MacKinnon and Thomson (2002)
Y_p (cm)	2.54	Stewart et al. (2022)	15	MacKinnon and Thomson (2002)
Z_p (cm)	0.5	Stewart et al. (2022)	1	MacKinnon and Thomson (2002)
M (g)	7.3	Stewart et al. (2022)	688	MacKinnon and Thomson (2002)
ρ^N (g/cm^3)	1.46	DiFilippo et al. (2010)	1.63	MacKinnon and Thomson (2002)
ρ_b (g/cm^3)	1.60	Assumed	1.57	MacKinnon and Thomson (2002)
C^{sol} (g/m^3)	1100	DiFilippo et al. (2010)	237	MacKinnon and Thomson (2002)
MW (g/mol)	131	Stewart et al. (2022)	166	MacKinnon and Thomson (2002)
S_0^N (%)	39.81	Calculated	29.84	Calculated
$k_{r,0}$	0.15	Calculated	0.27	Calculated
$^*\overline{k_r}$	0.58	Calculated	0.64	Calculated
k_0^{VA} (d^{-1})	0.408	Calculated	0.003	Calculated
γ	0.5	Theoretical	0.5	Theoretical

* The $\overline{k_r}$ parameter used for numerical mass transfer modeling is defined in section 3.3.

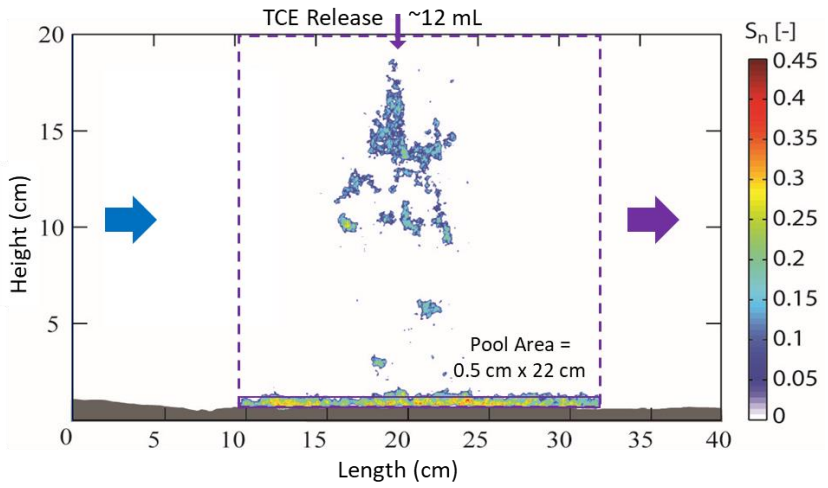

Figure 4-2. Single-cell, volume-averaged (VA) model representation of mixed source experiment. The dashed purple line represents the source zone volume (V_s) and the solid purple lines represent DNAPL pool volume (V_p) of the DNAPL accumulations. Only the pool zone was considered in this study. Adapted from Stewart et al. (2022).

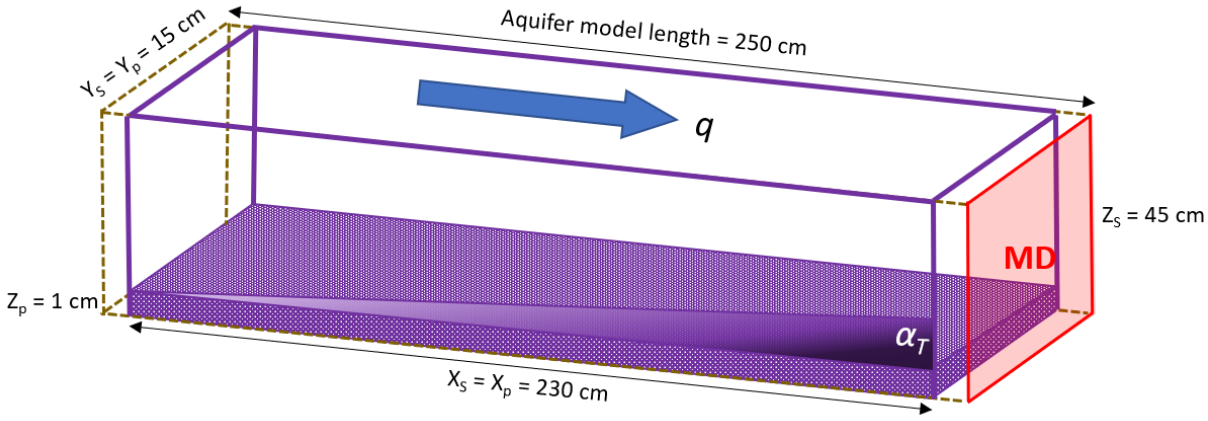

Figure 4-3. Single-cell, volume-averaged (VA) conceptualization of the PCE pool dissolution experiment conducted by MacKinnon and Thomson (2002). The thick purple lines represent the source zone volume (V_S) encompassing the DNAPL pool. The dashed lines represent the experimental apparatus dimensions, where the horizontal distance of 10 cm between V_S and tank edges corresponds to influent/effluent mixing zones generated by clearwell screens. The red square represents the numerical mass-discharge measurement plane.

4.7.3. Numerical Modeling of Flow-Cell Experiments

Steady-state pore-water flow conditions reported in both experiments (Table 4-1) were simulated using MODFLOW2000 (Harbaugh et al., 2000). The experimental DNAPL pools were discretized

as indicated in Table 4-2. Figure 4-4 illustrates the combination of maximum and minimum scales of the source zone discretization scenarios for Pool 1, listed in Table 4-2. The numerical grids of both experiments included two blocks upgradient from the source, or two columns of grid blocks depending on the vertical source zone discretization, as illustrated in Figure 4-3. All model domains included 6 and 8 grid blocks or columns downgradient from Pool 1 and Pool 2, respectively. All grid blocks upgradient and downgradient from the DNAPL sources measured 1.25 cm along the flow direction (X-axis) for consistency between models. Aqueous-phase transport was simulated with SEAM3D, neglecting retardation, and defining a constant concentration of C = 0 mg/L in all blocks upgradient from the DNAPL sources. This prevented numerical dispersion of aqueous-phase concentrations into upstream blocks located behind the source.

Table 4-2. Vertical and horizontal numerical discretization of Pools 1 and 2. Models were discretized for the range of values longitudinal (ΔX_p) and transverse (ΔZ_S) to flow.

Pool 1				**Pool 2**			
ΔZ_S (cm)	**Z_S / ΔZ_S**	**ΔX_p (cm)**	**X_p / ΔX_p**	**ΔZ_S (cm)**	**Z_S / ΔZ_S**	**ΔX_p (cm)**	**X_p / ΔX_p**
19	1	22	1	45	1	230	1
9.5	2	11	2	22.5	2	115	2
3.8	5	4.4	5	9	5	46	5
1.9	10	2.75	8	4.5	10	28.75	8
1	19	2	11	1	45	23	10
0.5	38	-	-	-	-	-	-

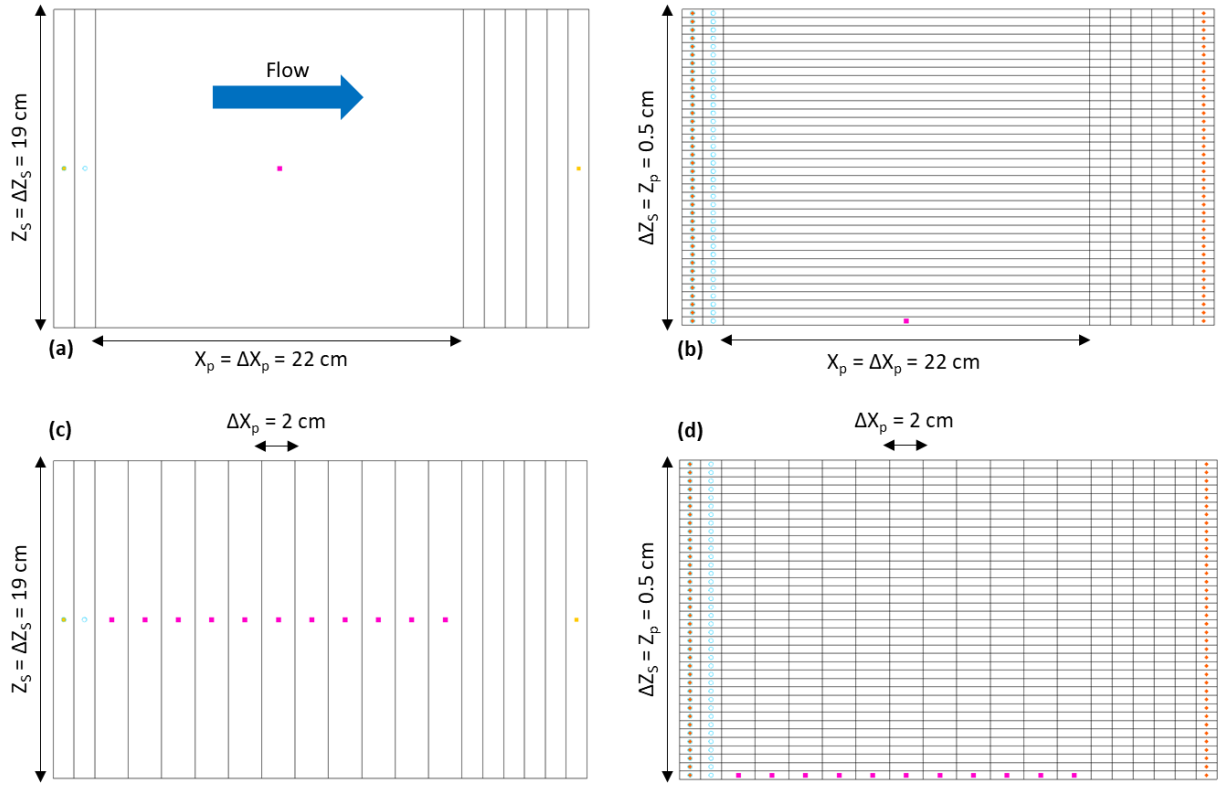

Figure 4-4. Examples of model discretization of the DiFilippo et al. (2010) bench-scale experiment (Pool 1). (a) Upscaled single-source DNAPL block with no vertical discretization (1D); (b) Single-source block with vertical discretization matching initial DNAPL pool dimensions (2D); (c) Upscaled source block discretized along the flow direction (1D); (d) Single source block discretized along the flow direction with vertical discretization matching initial DNAPL pool dimensions and (2D).

Mass discharge (MD) rates were calculated with SEAM3D by integrating flow-weighted, aqueous-phase concentrations observed at the most downgradient grid block(s) in all model domains. For both VA and numerical modeling results, a time of remediation (TOR) output was arbitrarily defined as the time when source discharge concentrations reached a value of C_i = 0.005 mg/L. A constant value of α_L = 0.025 cm was assigned to longitudinal dispersivity in all numerical models to minimize discrepancies with the VA model, which neglects α_L within the source zone (Stewart et al., 2022). Sensitivity analyses (not shown) showed numerical error for lower α_L values approaching 0, while greater values reduced MD rates. Moreover, α_T coefficients were assigned a value of 0.1 cm and 0.04 cm to the 2D domains of Pool 1 and Pool 2, respectively (Table 4-1). The α_T values matched the flow-cell media conditions and effluent observations using VA mass transfer concepts (Stewart et al. 2021 provides details on the Pool 1 VA simulation).

Initial mass transfer coefficients (k_0^{S3D} [T^{-1}] in Equation 4-3) were calculated modifying Equation 4-4 as:

$$k_0^{S3D} = \frac{q}{\Delta X_p \times Y_S \times \Delta Z_S \times \theta}\left[A_{p,yz}\overline{k_r} + \left(\Delta X_p \times Y_p\right)\sqrt{\frac{4\alpha_T}{\pi \Delta X_p}}\right] \quad (4\text{-}7)$$

where the subscript p = DNAPL pool. Parameter values are listed in Table 4-1. The range of values for the discretization parameters ΔX_p and ΔZ_S are listed in Table 4-2, and $\overline{k_r} = \left(1 + k_{0,r}\right)/2$. Because the NAPL dissolution package in SEAM3D does not include k_r, $\overline{k_r}$ was used as a surrogate (Table 4-1). The $\overline{k_r}$ parameter averaged the initial $k_{0,r}$ value with the maximum possible value of 1, maintaining a constant value in k_0^{S3D}. Also, k_0^{S3D} was divided by θ for equivalency in mass transfer definitions between the SEAM3D and VA models (Appendix B). Equation 4-7 indicates that the source zone height Z_S was discretized as ΔZ_S, while discretization of the coinciding source zone length X_S and pool length X_p was represented by ΔX_p. In turn, the $A_{p,yz}$ parameter was kept constant in all SEASM3D models because no discretization scale was below the DNAPL pool cross-sectional area perpendicular to flow. This method was conceived to maintain consistency with the VA model concept, where k_0^{VA} is upscaled by q and V_S (Stewart et al., 2022); and in this case, X_p was scaled by discretizing the DNAPL pools along the flow direction.

4.7.4. Comparative Modeling Analyses

Equation 4-7 was used to calculate values of the mass transfer coefficient based on the varied discretization of the pools provided in Table 4-2. Each discretization and the parameters in Table 4-1 were used with SEAM3D to calculate bulk discharge concentrations and the time of remediation (TOR) for each pool. Root-mean squared error (RMSE) calculated with respect to experimental discharge concentrations (Tables B-2 and B-4; Figures B-1 and B-2) did not yield clear relationships with the discretized parameters (Table 4-2), but consistent trends of numerical TOR outputs suggested a correlation between model layering ($Z_S/\Delta Z_S$) and the X_p lengths. The correlation allowed for scaling the VA mass transfer function (k_0^{VA} – Equation 4-4) to empirically

find a single optimal k_0^{S3D} value for each prescribed ΔZ_S height, capable of matching upscaled effluent rates and physical TOR predictions. Subsequent analyses incorporated single, scaled k_0^{S3D} values across all ΔX_p lengths, for each ΔZ_S height, and were contrasted with inverse parameter estimates (Tables B-5 and B-7).

Inverse numerical modeling was undertaken with PEST (Watermark Numerical Computing, 2018) to estimate k_0^{S3D} values for *all* combinations of pool discretization parameters (Table 4-2). For Pool 1, history-matching targets included MD measurements attributed to the pool zone dissolution; whereas these corresponded to steady-state MD rates induced by flow dissolution of Pool 2 prior to oxidant flushing (both monitoring profiles shown in Figure 4-5). The resulting variability of inversely estimated parameters (Tables B-3 and B-4) and outputs were contrasted with the deterministic numerical investigation, including the initial analyses where $X_p = \Delta X_p$, and the ensuing correlation where X_p values were empirically scaled as a function of model layering. The comparison involved quantifying summary statistics to assess accuracy (mean values, μ) and variability (standard deviations, σ) of numerical TOR results averaged across all discretization scenarios, with respect to VA predictions. Both forward and inverse numerical results elucidated upon a methodology for scaling k_0^{VA} to minimize complex grid effects driven by the simulation of dispersive aqueous transport across discretized source zones, allowing for reproducing upscaled DNAPL pool dissolution at any grid resolution.

4.8. Results and Discussion

4.8.1. Numerical Discretization of Bulk Mass Transfer Coefficients

Figure 4-5 presents a comparison between VA and SEAM3D simulations of experimental mass discharge rates. As shown, the single-block numerical models produced the best fit to the VA models and the effluent data when using Equation 4-7 to parameterize the pool and without calibrating models by modifying k_0^{S3D}. The results also showed greater sensitivity with respect to variability of k_0^{S3D} values calculated with Equation 4-7 and the source zone discretization parameters in Table 4-2 (calculated k_0^{S3D} and RMSE values in Appendix B). Figure 4-5 also indicates a relatively lower numerical sensitivity to increasing k_0^{S3D} rates, suggesting the

possibility for non-unique predictions of pool mass depletion by mass transfer models with multiple source zone layers. Therefore, fitting effluent data with multi-layered source zone models, where dispersive transport plays a significant role on the mass transfer simulation, may bias TOR predictions without adequate parameter uncertainty constraints. While resulting RMSE values did not provide a concise comparison metric (Figures B-1 and B-2), the VA physical TOR predictions provided a reference metric for constraining k_0^{S3D} parameters. Specifically, the deterministic SEAM3D TOR results, produced with Equation 4-7 and Table 4-2, exhibited a clear tendency as a function of pool source discretization. These trends are presented in Figure 4-6.

Figure 4-6 shows clear trends of decreasing TOR values with smaller ΔX_p lengths; i.e., a greater number of grid blocks discretizing the X_p lengths. As shown, the trends were consistent for all ΔZ_S heights (Table 4-2), where the VA predictive TOR values intersected the linearly-interpolated SEAM3D results at greater number of X_p grid blocks for smaller ΔZ_S heights. This indicates that the multi-layered models with greater vertical resolution require larger, yet specific k_0^{S3D} values, where aqueous transport across the discretized pool zone disperses source mass fluxes to reproduce the upscaled effluent rates. As studies have shown, resolving source dispersive fluxes by aqueous transport simulation requires a grid resolution adequate to the scale of dispersivity (Falta, 2003; Fernandez-Garcia et al., 2009), corresponding to α_T values (0.1 cm for Pool 1, 0.04 cm for Pool 2) representative of DNAPL pool dissolution in this study (Carey et al., 2018; Stewart et al., 2022). Figure 4-6 thereby suggests that α_T coefficients played a complementary role in both kinetic mass transfer and aqueous transport, regulating pool mass depletion rates in vertically-discretized source zones. Given that effluent rates simulated with SEAM3D models with finer vertical resolution were less sensitive to k_0^{S3D} variability (Figure 4-5), yet clearly sensitive to the VA physical TOR predictions (Figure 4-6), controlled by ΔX_p lengths, scaling the VA mass transfer function would constrain the uncertainty of k_0^{S3D} parameters estimated in discretized domains.

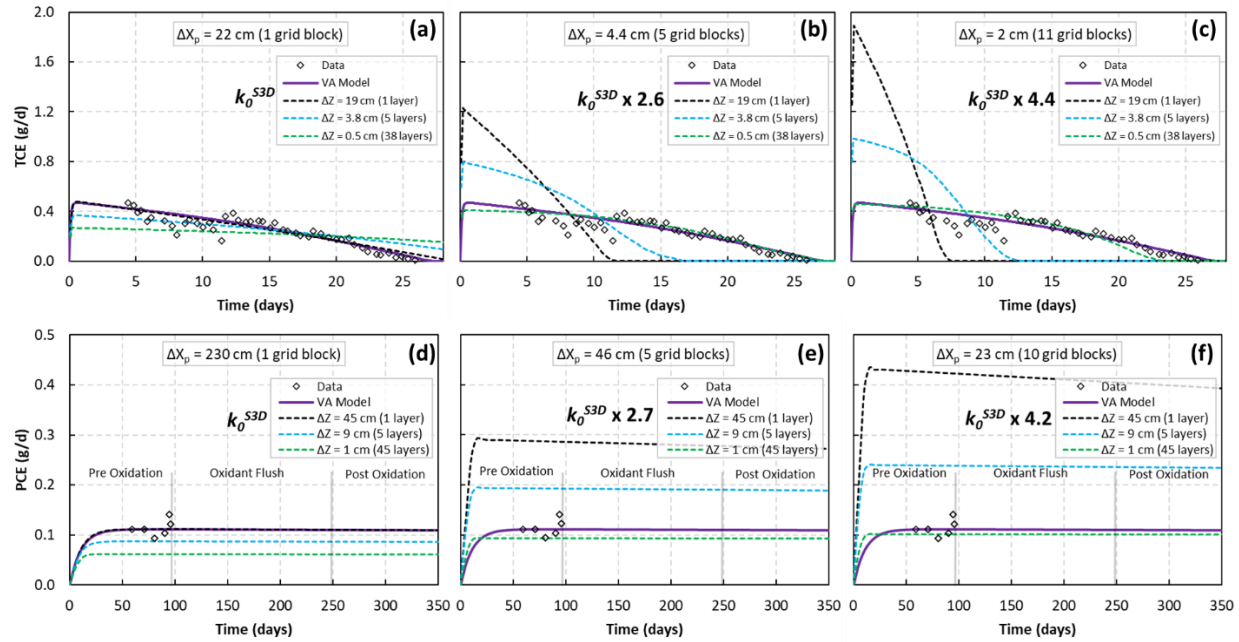

Figure 4-5. Comparison between measured and simulated experimental mass discharge (MD) rates. Panels (a) through (c) correspond to Pool 1, whereas panels (d) through (f) correspond to Pool 2. The k_0^{S3D} values were calculated with Equation 4-7 and the indicated ΔX_p lengths, where the shown k_0^{S3D} increments are with respect to $\Delta X_p = X_p$ (a and d).

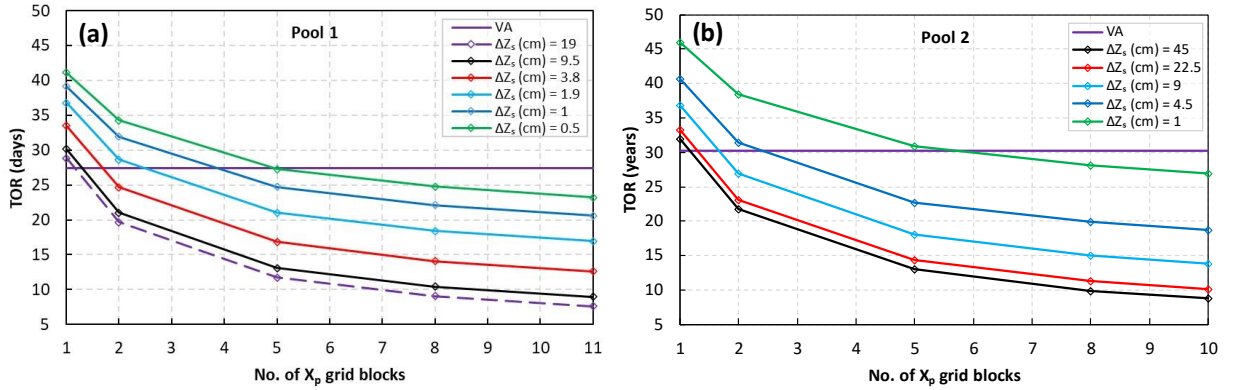

Figure 4-6. Comparison of TOR results between VA and SEAM3D models of (a) Pool 1 and (b) Pool 2 using k_0^{S3D} values calculated with Equation 4-7 and parameters in Table 4-2.

4.8.2. Scaling of Bulk Mass Transfer Coefficients

Trends shown in Figure 4-6 indicated that comparable numerical and VA TOR values can be obtained using the entire X_p length to calculate k_0^{S3D} values in 1D models and 2D models with source zones vertically discretized in 2 layers. Hence, *dispersion* in aqueous-phase transport had a

negligible role in replicating monitored effluent histories using coarser 2D discretization scales of source zone reference volumes (V_S), regardless of the difference in α_T magnitudes (Table 4-1) and ΔZ_S dimensions (Table 4-2) between both experiments. The intersection of the VA TOR line with numerical TOR lines in Figure 4-6 was used to produce the empirical k_0^{VA} scaling correlations shown in Figure 4-7. For both experiments, best-fit trend lines were found through power functions correlating the number of prescribed Z_S blocks to the number of necessary X_p grid blocks.

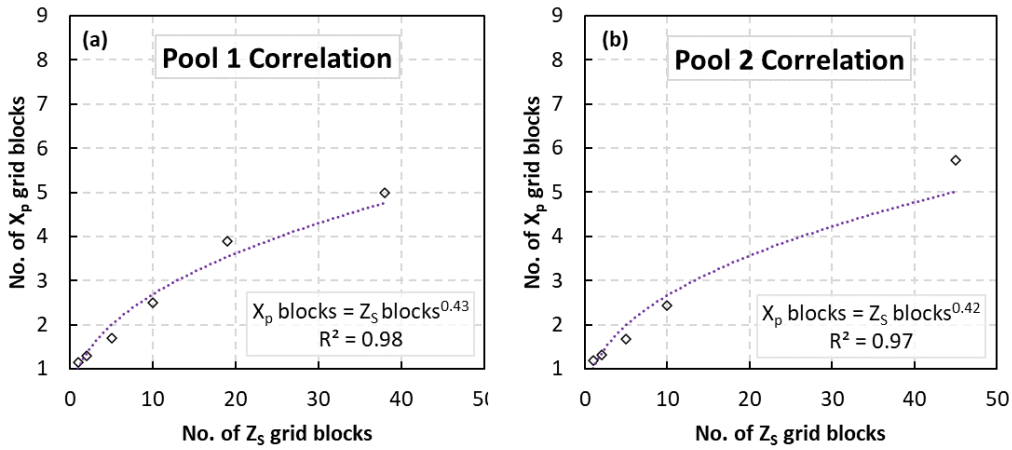

Figure 4-7. Empirical correlations between the number of X_p blocks and the prescribed number of Z_S blocks that produced comparable (a) Pool 1 and (b) Pool 2 dissolution results with the VA models.

For clarity, the "number of necessary X_p blocks" refers to the number by which to divide the actual X_p length only for the purpose of calculating a single k_0^{S3D} value for each ΔZ_S height, expressed by Equations 4-8 and 4-9:

$$k_0^{S3D} = \frac{q}{\tilde{X}_p \times Y_S \times \Delta Z_S \times \theta}\left[A_{p,yz}\overline{k_r}(M_p) + (\tilde{X}_p \times Y_p)\sqrt{\frac{4\alpha_T}{\pi \tilde{X}_p}}\right] \tag{4-8}$$

where $\tilde{X}_p$ is a scaled X_p length in relation to the source zone vertical discretization:

$$\tilde{X}_p = \frac{X_p}{\left(\frac{Z_S}{\Delta Z_S}\right)^{\eta}} \tag{4-9}$$

and η is a scaling parameter for empirically minimizing grid effects on the numerical mass transfer simulation. The range of η values is expected to vary between ~0.2 – 0.4 in most practical applications, per results in Figure 4-7 and Table 4-3. As indicated in Table 4-3, the $\tilde{X}_p$ parameter decreases in magnitude with finer ΔZ_S discretization and/or larger α_T values. This is because the accurate resolution of concentrations gradients driven by low α_T values has more stringent discretization requirements, which are relaxed by higher α_T values in relation to the grid Peclet (Pe) number (Zheng & Bennett, 2002). Here, the vertical $Pe = \Delta Z_S/\alpha_T$ (Table 4-3). Equations 4-8 and 9 thereby provide a means to constrain the uncertainty of k_0^{S3D} parameters as a function of source architectural and discretization dimensions. This represents an advantage over assuming DNAPL pool dissolution as local equilibrium process resolved by ultrafine numerical grids for decision-support applications (Falta, 2003; Parker & Park, 2004; Kokkinaki et al., 2014; Stewart et al., 2021). Equation 4-8 and 4-9 could instead be used to constrain mass transfer uncertainty in layered models, such as numerical modeling of multilevel monitoring systems for characterizing heterogenous sources (Mobile et al., 2012; 2016; Prieto-Estrada et al., 2023b).

Table 4-3. Comparison of grid-scaled DNAPL pools lengths ($\tilde{X}_p$) and k_0^{S3D} coefficients calculated using different η values (Equations 4-8 and 4-9), including absolute and normalized Pe values. TOR results are shown in Figure 4-8.

Z_S / ΔZ_S	Pe	Pe/Pe^{max}	η	$\tilde{X}_p$ (cm)	k_0^{S3D} (d^{-1})	η	$\tilde{X}_p$ (cm)	k_0^{S3D} (d^{-1})
Pool 1								
1	-	-	0.43	22.0	1.018	0.30	22.0	1.018
2	95	1	0.43	16.3	2.420	0.30	17.9	2.296
5	38	0.4	0.43	11.0	7.634	0.30	13.6	6.742
^10	^19	^0.2	0.43	8.2	18.278	^0.36	9.6	16.576
19	10	0.11	0.43	6.2	41.165	0.43	6.2	41.165
*38	*5	*0.05	0.43	4.6	99.314	*0.43	4.6	99.314
Pool 2								
1	-	-	0.42	230.0	0.008	0.30	230	0.008
2	562.5	1	0.42	171.9	0.019	0.30	186.8	0.018
5	225	0.4	0.42	117.0	0.061	0.30	141.9	0.054
^10	^112.5	^0.2	0.42	87.4	0.145	^0.30	115.3	0.123
*45	*25	*0.04	0.42	46.5	0.974	*0.42	46.5	0.974

Symbols ^ and * highlight an increase of η values relative to decreasing Pe/Pe^{max} values.

Figures 4-8a and 4-8b show a TOR comparison between VA results and SEAM3D simulations using k_0^{S3D} coefficients scaled for Pools 1 and 2, respectively, using constant η values (Figure 4-7 and Table 4-3). Better approximations to VA TOR values were achieved by 1D numerical results, and by 2D numerical results produced with the smallest ΔZ_S heights in both experiments. Figures 4-8a and 4-8b also indicate a tendency for underestimating TOR with numerical models corresponding to intermediate ΔZ_S heights using the correlations shown in Figure 4-7, suggesting a need for adjusting the η parameter for greater SEAM3D-VA TOR equivalencies at multiple grid resolutions. Figures 4-8c and 8d show improved TOR equivalency by adjusting the η exponent as indicated in Table 4-3. Both the adjusted and constant η values, presented in Table 4-3, are consistent with further scaling of k_0^{S3D} values with decreasing vertical Pe values to reproduce upscaled MD and TOR predictions. However, while the absolute Pe magnitudes differed between both experiments, the normalized Pe values in Table 4-3 suggested a complex relationship between the scaling exponent η and the model layering, highlighting the worth of Equations 4-8 and 4-9 to

empirically account for complex grid effects on upscaled mass transfer rates. A statistical summary of the variability in predictive TOR values across all discretization scenarios is presented in Table 4-4.

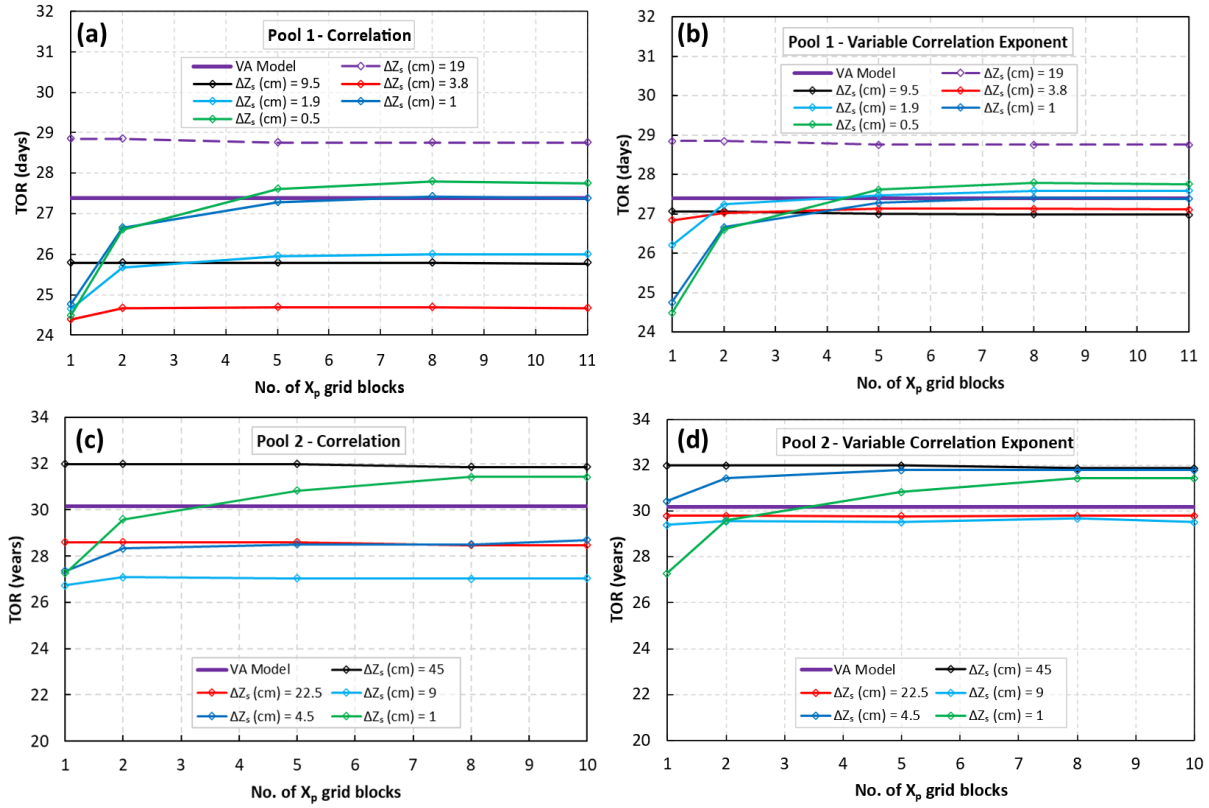

Figure 4-8. Comparison between SEAM3D and VA TOR results. Panels (a) and (c) depict results estimated with constant η values, whereas (b) and (d) with η values adjusted empirically for Pools 1 and 2, respectively. All panels show a tendency for underestimating TOR by models with more than 10 layers and normalized Pe values ≥ 0.2 (Table 4-3), contrasting the insensitivity to downgradient discretization (ΔX_p) of coarse-layered and 1D models. All 2D models required k_0^{S3D} scaling (Equations 4-8 and 4-9) to approximate the VA physical TOR predictions.

Table 4-4. Statistics of TOR results averaged across all discretization scenarios (Table 4-2) depicted in Figure 4-8. Estimated VA TOR values are 27.4 days and 30.2 years for Pool 1 and Pool 2, respectively.

Average	Pool 1			Pool 2		
Statistic	Fixed η	Variable η	PEST	Fixed η	Variable η	PEST
μ	26.4 days	27.3 days	29.3 days	29.2 years	30.6 years	26.7 years
σ	1.5 days	0.9 days	1.1 days	2 years	1.2 years	2.1 years

As shown in Figures 4-8b and 4-8d, and as quantified by the summary statistics presented in Table 4-4, reducing VA-SEAM3D disparities in TOR predictions through empirical adjustment of the η parameter can also approximate optimal ΔX_p lengths. Specifically, all 2D numerical models required scaling of k_0^{S3D} coefficients, but only models with 10 or more layers ($Pe/Pe^{max} \geq 0.2$ in Table 4-3) showed sensitivity to ΔX_p, as shown by all panels in Figure 4-8. Figures 4-8b and 4-8d suggest that $\tilde{X}_p$ lengths calculated with Equation 4-8 and 4-9, by empirically adjusting η, can be used to define ΔX_p lengths, minimizing grid effects on upscaled mass transfer rates. For example, when ΔZ_S = 0.5 cm in the Pool 1 case, ΔX_p = 4.4 cm and $\tilde{X}_p$ = 4.6 cm produced the closest approximation to the upscaled TOR values (five X_p grid blocks in Figure 4-8b). Similarly, when ΔZ_S = 1 cm in the Pool 2 case, ΔX_p = 46 cm and $\tilde{X}_p$ = 46.5 cm approximated the upscaled TOR prediction (five X_p grid blocks in Figure 4-8d) without underestimating it. The empirical approach for scaling estimable bulk mass transfer coefficients (k_0^{VA}) can be valuable for constraining numerical simulations where dispersive transport across NAPL blocks is significant.

4.8.3. Inverse Numerical Modeling

Figure 4-9 shows a TOR comparison between VA predictions and inverse SEAM3D results derived from lumped-process k_0^{S3D} parameters (Equation 4-3) estimated for *each* combination of source discretization lengths (Tables B-5 and B-7). The goal of estimating "unique" k_0^{S3D} parameters by matching pool dissolution histories was to gain insights on source mass depletion variability induced by dispersive transport across DNAPL grid blocks, referred to as grid resolution effects. As shown in Figure 4-9, TOR estimates varied minimally with ΔX_p lengths within each ΔZ_S, except for single-block numerical results. Overall, PEST results tended to slightly overestimate TOR, except for the finest ΔZ_S case of Pool 2 (Figure 4-9b). This case emphasized the propensity for model biasing by history matching without uncertainty constraints (i.e., parameter uncertainty bounds). Yet discrepancies with respect to VA predictions were negligible from a practical standpoint.

In the Pool 1 case, PEST minimization of residual error ($\boldsymbol{\varepsilon}$) with respect to fluctuating discharge concentrations (measurement noise) slightly underestimated k_0^{S3D} values (Table B-5) and TOR (Figure 4-9a), despite the availability of a complete monitoring profile (Figures 4-5 and 4-10). In

the Pool 2 case, fitting a few steady-state dissolution measurements required arbitrarily truncating the allowed parameter movement to avoid further TOR underestimation when ΔZ_S = 1 cm (Table B-7). Otherwise, k_0^{S3D} values would have reached any prescribed upper parameter bounds driven by unconstrained **ε** minimization. These results corroborated the decreasing sensitivity (Figure 4-5) to effluent rates by layered models where dispersive transport across source grid blocks regulated the mass transfer simulation. Inverse modeling results supported the calculation of a single k_0^{S3D} parameter (Equation 4-8) for each ΔZ_S, where $\tilde{X}_p$ values (Equation 4-9) can be used to define optimal ΔX_p lengths, minimizing numerical and predictive errors.

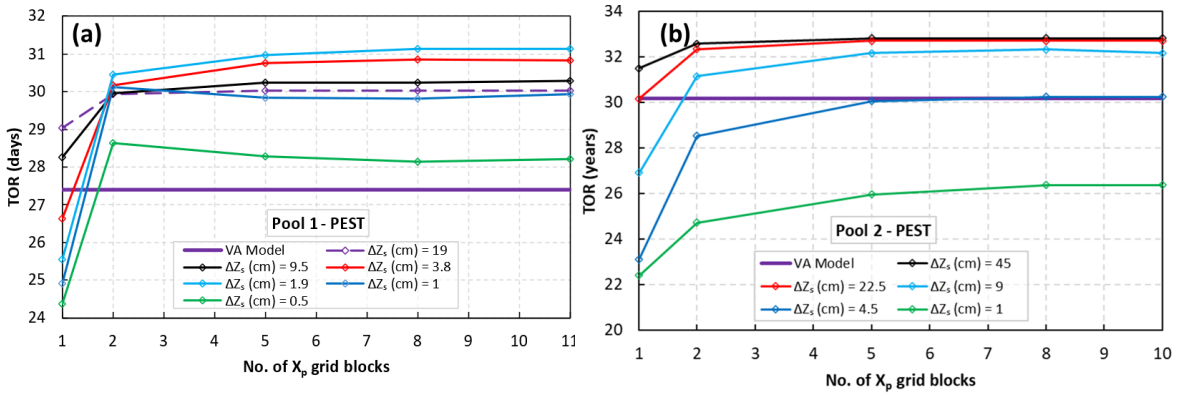

Figure 4-9. Comparison between inverse SEAM3D modeling and VA estimates of TOR. (a) Pool 1 results show a slight overestimation of TOR values, whereas (b) Pool 2 results show a slight underestimation. Both panels show minimal TOR variability across all ΔX_p lengths for each ΔZ_S, except for all single-block numerical results.

Figure 4-10 shows a comparison between MD rates simulated with k_0^{S3D} using Equations 4-8 and 4-9 vs twofold and solubility-limit k_0^{S3D} increments in models with the finest vertical layering. While numerical error is obvious in the short- and long-term Pool-1 simulations (Figures 4-10a and 4-10b), modeling the steady-state Pool-2 dissolution does not show any error (Figure 4-10c). The latter emphasizes the non-uniqueness of lumped-process k_0^{S3D} parameters, whereas all panels in Figure 4-10 highlight the ultrafine gridding required to simulate DNAPL pool dissolution assuming local equilibrium. Attributing numerical error to grid resolution was confirmed by reducing time steps calculated implicitly by the generalized conjugate gradient (GCG) solver in SEAM3D. Although the GCG solver calculated time steps well below the explicit criteria for numerical stability in dispersive transport simulation (Appendix B), decreasing time steps further by an order of magnitude did not reduce error (results not shown). These analyses supported the

empirical scaling of estimable k_0^{VA} coefficients to constrain the uncertainty of lumped k_0^{S3D} parameters, regulated by aqueous hydrodynamic dispersion across DNAPL grid blocks in relation to vertical and downgradient source discretization, and monitoring data availability.

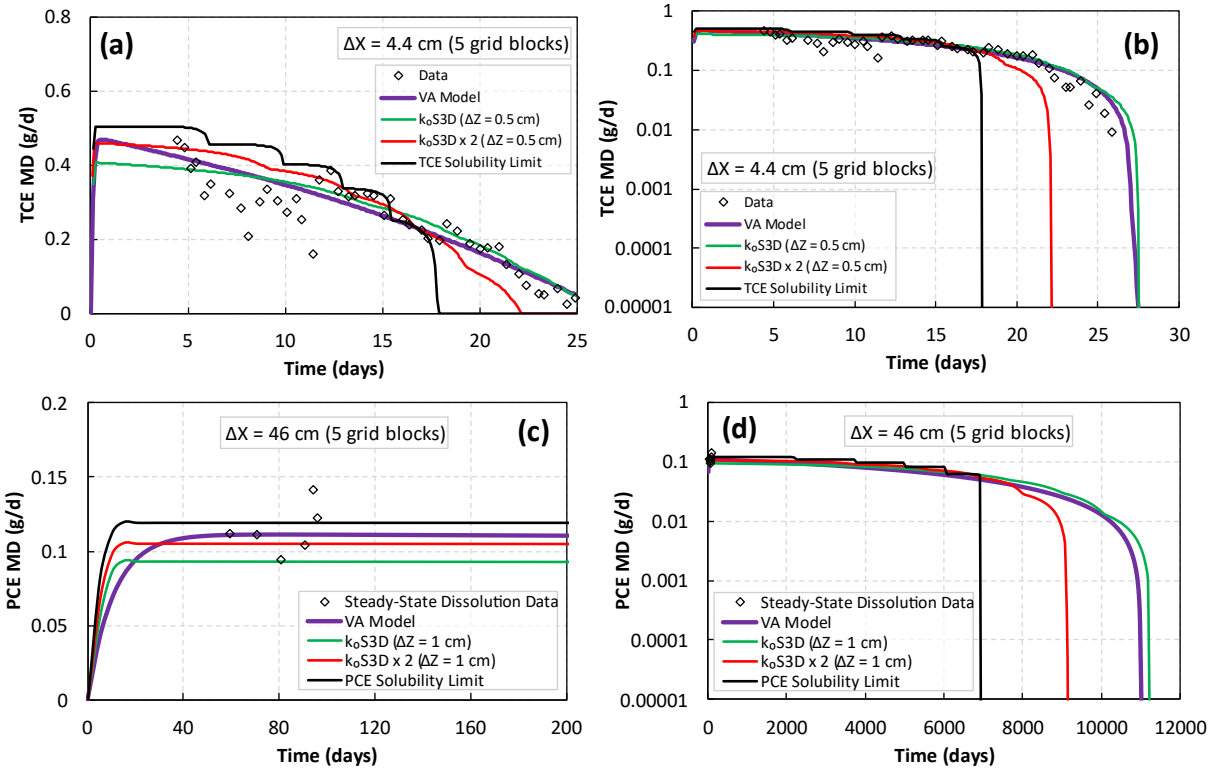

Figure 4-10. Comparison between measured and simulated MD rates using the VA and SEAM3D models. SEAM3D simulations correspond to the finest vertical discretization of Pools 1 (a and b) and 2 (c and d). All panels contrast results of k_0^{S3D} parameters constrained by Equations 4-8 and 4-9 vs twofold k_0^{S3D} increments up to solubility limits.

4.9. Conclusions

A straightforward method for simulating upscaled DNAPL dissolution in discretized domains correlated the numerical grid resolution to pool zone lengths in the downgradient direction. Scaling the downgradient pool lengths for constraining a single mass transfer parameter as a function of source-zone model layering was supported by a series of forward and inverse numerical analyses. The former showed a decreasing sensitivity of mass transfer parameters to experimental mass discharge rates with increasing number of model layers, while the latter revealed minimal variability in estimated values as a function of downgradient source discretization. In turn,

downgradient discretization was found relevant for reproducing upscaled DNAPL dissolution in cases where dispersive transport regulated mass transfer rates, corresponding to models with 10 or more layers in both experiments. This attribution was found to be independent of the difference in magnitude in source zone dimensions, model layer thicknesses, and transverse vertical dispersivity coefficients between experiments, suggesting value in empirical scaling of physical mass transfer coefficients for lumped parameter constraining. The empirical approach involved adjusting a scaling parameter to match upscaled simulations of DNAPL pool dissolution and physical predictions of source mass depletion in discretized domains. Nonetheless, limitations to the approach for practical applications include the scale of the laboratory experiments, encompassing relatively homogenous porous media characteristics and idealized flow conditions not representative of large-scale field systems. While the VA mass transfer model offers adaptability to source zone dimensions and flexibility for accommodating flow-field heterogeneity, additional research leveraging high-resolution site characterization and historical mass discharge monitoring could prove beneficial for additional testing of the scaling methodology.

A key advantage of the methodology leverages the physical basis of the upscaled DNAPL dissolution model to explicitly constrain numerical simulations of mass transfer and transport. The simplest approach involves designating a single source block within a single-layer numerical model, as the analyses indicated that providing Equation 7 with source architectural dimensions would not require scaling bulk mass transfer coefficients to the downgradient grid resolution. Conversely, layered models may benefit from the empirical scaling analysis in situations where the grid resolution and/or the scale of vertical hydrodynamic dispersion regulate mass transfer across DNAPL grid blocks. Examples of potential applications include inverse modeling of multilevel monitoring systems to estimate spatially-varying lumped-process parameters and saturations, and the simulation of DNAPL dissolution in multiple hydrostratigraphic units. In these situations, the explicit relationships of the VA model provide a viable method for constraining the plausible variability of lumped-process parameters on the basis of source zone delineation, which may be refined by fitting monitoring histories constrained by the scaling approach. Defining scale-dependent mass-transfer uncertainty bounds would thereby reduce the possibility for incurring model error and predictive bias through history matching.

Future research is needed to discern grid resolution effects on numerical mass transfer simulation vs scale-dependent transverse hydrodynamic dispersion not captured by the VA model, including datasets from contaminated field sites. Multicomponent dissolution analyses are also needed to evaluate the variability of the empirical scaling parameter η with aqueous solubility, regulating interphase mass transfer rates (Equation 1). Although mass transfer variability was not directly attributed to vertical Pe numbers, accurately fitting VA simulations with SEAM3D required slightly larger η values for Pool 1, relative to Pool 2 in models with 10 or more layers. These comparative trends suggest value in future examination of multicomponent data to discern drivers of mass transfer variability. Specifically, distinguishing variability caused by grid resolution effects vs hydrodynamic vertical dispersion not captured by the upscaled model would increase confidence in decision-support applications. Such distinction can be explored by comparing simulated vs measured concentrations at discrete vertical intervals, using lumped-process parameters constrained on the basis of NAPL zone dimensions (Equations 4-4 and 4-5), with or without parameter scaling (Equations 8 and 9) to fit observations. Furthermore, implementing multi-rate coefficients in single SEAM3D source blocks may be of further practical value, where geostatistically-correlated flow and transport parameters can support the quantification of plume and source attenuation uncertainties at field scales.

4.10. Acknowledgments

This study was partially supported by the Environmental Security Technology Certification Program (ESTCP) under Project ER19-5223. The content of this manuscript has not been subject to agency review and does not necessarily represent the view of the sponsoring agency.

4.11. Data Availability Statement

The Groundwater Modeling System (GMS) software hosting the MODFLOW2000 and SEAM3D programs is available through Aquaveo at https://www.aquaveo.com/software/gms-groundwater-modeling-system-introduction. PEST software is available at https://pesthomepage.org/programs. Aqueous-phase concentration data will be archived in an online repository maintained by Virginia Tech with a unique DOI number.

References

Abriola, L. M., Miller, E. L., Pennell, K. D., Ramsburg, A., & Christ, J. A. (2013). *Metric identification and protocol development for characterizing DNAPL source zone architecture and associated plume response.* Alexandria, VA: SERDP Project ER-1612.

Agaoglu, B., Copty, N. K., Scheytt, T., & Hinkelmann, R. (2015). Interphase mass transfer between fluids in subsurface formations: A review. *Advances in Water Resources, 79*, 162-194. https://doi.org/10.1016/j.advwatres.2015.02.009

Basu, N. B., Fure, A. D., & Jawitz, J. W. (2008). Predicting dense nonaqueous phase liquid dissolution using a simplified source depletion model parameterized with partitioning tracers. *Water Resources Research, 44*(7). https://doi.org/:10.1029/2007WR006008

Brusseau, M. L., Matthieu III, D. E., Carroll, K. C., Mainhagu, J., Morrison, C., McMillan, A., . . . Plaschke, M. (2013). Characterizing Long-term Contaminant Mass Discharge and the Relationship Between Reductions in Discharge and Reductions in Mass for DNAPL Source Areas. *Journal of Contaminant Hydrology*, 1-12. https://doi.org/10.1016/j.jconhyd.2013.02.011

Carey, G. R., McBean, E. A., & Feenstra, S. (2014). DNAPL Source Depletion: 1. Predicting Rates and Timeframes. *Remediation, 14*(3), 21-47. https://doi.org/10.1002/rem.21393

Carey, G. R., McBean, E. A., & Feenstra, S. (2018). Estimating transverse dispersivity based on hydraulic conductivity. *Environmental Technology & Innovation, 10*, 36-45. https://doi.org/10.1016/j.eti.2018.01.008

Christ, J. A., Ramsburg, A. C., Pennell, K. D., & Abriola, L. M. (2006). Estimating mass discharge from dense nonaqueous phase liquid source zones using upscaled mass transfer coefficients: An evaluation using multiphase numerical simulations. *Water Resources Research, 42*(11). https://doi.org/10.1029/2006WR004886

Christ, J. A., Ramsburg, C. A., Pennell, K. D., & Abriola, L. M. (2010). Predicting DNAPL mass discharge from pool-dominated source zones. *Journal of Contaminant Hydrology, 114*(1-4), 18 - 34. https://doi.org/10.1016/j.jconhyd.2010.02.005

Dekker, T. J., & Abriola, L. M. (2000). The influence of field-scale heterogeneity on the infiltration and entrapment of dense nonaqueous phase liquids in saturated formations. *Journal of Contaminant Hydrology, 42*(2-4), 187-218. https://doi.org/10.1016/S0169-7722(99)00092-3

DiFilippo, E. L., & Brusseau, M. L. (2008). Relationship Between Mass Flux Reduction and Source-Zone Mass Removal: Analysis of Field Data. *Journal of Contaminant Hydrology, 98*(1-2), 22-35. https://doi.org/10.1016/j.jconhyd.2008.02.004

DiFilippo, E. L., & Brusseau, M. L. (2011). Assessment of a Simple Function to Evaluate the Relationship Between Mass Flux Reduction and Mass Removal for Organic-Liquid

Contaminated Source Zones. *Journal of Contaminant Hydrology, 123*(3-4), 104-113. https://doi.org/10.1016/j.jconhyd.2010.12.011

DiFilippo, E. L., Carroll, K. C., & Brusseau, M. (2010). Impact of organic-liquid distribution and flow heterogeneity on reductions in mass flux. *Journal of Contaminant Hydrology, 115*(1-4), 14-25. https://doi.org/10.1016/j.jconhyd.2010.03.002

Eberhardt, C., & Grathwohl, P. (2002). Time scales of organic contaminant dissolution from complex source zones: coal tar pools vs. blobs. *Journal of Contaminant Hydrology, 59*(1-2), 45-66. https://doi.org/10.1016/S0169-7722(02)00075-X

Engelmann, C., Handel, F., Binder, M., Yadav, P. K., Dietrich, P., Liedl, R., & Walther, M. (2019). The fate of DNAPL contaminants in non-consolidated subsurface systems – Discussion on the relevance of effective source zone geometries for plume propagation. *Journal of Hazardous Materials, 375*, 233-240. https://doi.org/doi.org/10.1016/j.jhazmat.2019.04.083

Eniarson, M., Fure, A., St. Germain, R., Chapman, S., & Parker, B. (2018). DyeLIF™: A New Direct-Push Laser-Induced Fluorescence Sensor System for Chlorinated Solvent DNAPL and Other Non-Naturally Fluorescing NAPLs. *Groundwater Monitoring & Remediation*, 28-42. https://doi.org/10.1111/gwmr.12296

Falta, R. (2003). Modeling sub-grid-block-scale dense nonaqueous phase liquid (DNAPL) pool dissolution using a dual-domain approach. *Water Resources Research, 39*(12). https://doi.org/10.1029/2003WR002351

Falta, R. W., Basu, N., & Rao, S. P. (2005a). Assessing impacts of partial mass depletion in DNAPL source zones: II. Coupling source strength functions to plume evolution. *Journal of Contaminant Hydrology*, 45-66. https://doi.org/10.1016/j.jconhyd.2005.05.012

Falta, R. W., Rao, S. P., & Basu, N. (2005b). Assessing the impacts of partial mass depletion in DNAPL source zones I. Analytical modeling of source strength functions and plume response. *Journal of Contaminant Hydrology*, 259-280. https://doi.org/0.1016/j.jconhyd.2005.05.010

Fernandez-Garcia, D., Llerar-Meza, G., & Gomez-Hernandez, J. (2009). Upscaling transport with mass transfer models: Mean behavior and propagation of uncertainty. *Water Resources Research, 45*, W10411. https://doi.org/10.1029/2009WR007764

Frind, E. O., Molson, J. W., & Schirmer, M. (1999). Dissolution and mass transfer of multiple organics under field conditions: The Borden emplaced source. *Water Resources Research, 35*(3), 683-694. https://doi.org/10.1029/1998WR900064

Guo, Z., Russo, A. E., DiFilippo, E. L., Zhang, Z., Zheng, C., & Brusseau, M. L. (2020). Mathematical modeling of organic liquid dissolution in heterogeneous source zones. *Journal of Contaminant Hydrology, 235*. https://doi.org/10.1016/j.jconhyd.2020.103716

Harbaugh, A. W., Banta, E. R., Hill, M. C., & McDonald, M. G. (2000). *MODFLOW-2000, The U.S. Geological Survey Modular Ground-Water Model: User Guide to Modularization Concepts and the Ground-Water Flow Process.* Reston, Virginia: U.S. Geological Survey. https://doi.org/10.3133/ofr200092

Horst, J., Welty, N., Stuetzle, R., Wenzel, R., & Germain, R. (2018). Fluorescent dyes: A new weapon for conquering DNAPL characterization. *Groundwater Monitoring & Remediation, 38*(1), 19-25. https://doi.org/10.1111/gwmr.12261

Huang, J., Christ, J. A., & Goltz, M. N. (2010). Analytical solutions for efficient interpretation of single-well push-pull tracer tests. *Water Resources Research*. https://doi.org/10.1029/2008WR007647

Hunt, J. R., & Sitar, N. (1988). Nonaqueous Phase Liquid Transpot and Cleanup 1. Analysis of Mechanisms. *Water Resources Research, 24*(8), 1247-1258. https://doi.org/10.1029/WR024i008p01247

Johnson, R. L., & Pankow, J. F. (1992). Dissolution of dense chlorinated solvents into groundwater. 2. Source function for pools of solvent. *Environmental Science & Technology, 26*(5), 869-901. https://doi.org/doi.org/10.1021/es00029a004

Klemm, S. M., Seagren, E. A., Becker, J. G., & Mayer, A. S. (2021). Mass Flux Analysis of Abiotic Tetrachloroethene Dense Nonaqueous Phase Liquid Pool Dissolution in a Heterogeneous Flow Environment. *Groundwater Monitoring & Remediation, 41*(4), 34-48. https://doi.org/10.1111/gwmr.12466

Kokkinaki, A., Werth, C. J., & Sleep, B. E. (2014). Comparison of upscaled models for multistage mass discharge from DNAPL source zones. *Water Resources Research*, 3187 - 3205. https://doi.org/10.1002/2013WR014663

Kueper, B. H., Stroo, H. F., Vogel, C. M., & Ward, C. H. (2014). *Chlorinated Solvent Source Zone Remediation.* Springer New York. https://doi.org/10.1007/978-1-4614-6922-3

Lemke, L. D., & Abriola, L. M. (2006). Modeling dense nonaqueous phase liquid mass removal in nonuniform formations: Linking source-zone architecture and system response. *Geosphere, 2*(2), 74-82. https://doi.org/10.1130/GES00025.1

Leung, J. Y., & Srinivasan, S. (2016). Effects of reservoir heterogeneity on scaling of effective mass trasnfer coefficient for solute transport. *Journal of Contaminant Hydrology, 192*, 181-193. https://doi.org/10.1016/j.jconhyd.2016.07.007

Liu, Y., Illangasekare, T. H., & Kitandis, P. K. (2014). Long-term mass transfer and mixing-controlled reactions of a DNAPL plume from persistent residuals. *Journal of Contaminant Hydrology, 157*, 11-24. https://doi.org/10.1016/j.jconhyd.2013.10.008

MacKinnon, L. K., & Thomson, N. R. (2002). Laboratory-scale in situ chemical oxidation of a perchloroethylene pool using permanganate. *Journal of Contaminant Hydrology, 56*, 49-74. https://doi.org/doi.org/10.1016/S0169-7722(01)00203-0

Marble, J. C., DiFilippo, E. L., Zhang, Z., Tick, G. R., & Brusseau, M. L. (2008). Application of a lumped-process mathematical model to dissolution of non-uniformly distributed immiscible liquid in heterogeneous porous media. *Journal of Contaminant Hydrology, 100*, 1-10. https://doi.org/10.1016/j.jconhyd.2008.04.003

Mayer, A. S., & Hassanizadeh, M. S. (2005). *Soil and Groundwater Contamination: Nonaqueous Phase Liquids–Principles and Observations.* Washington, D.C.: American Geophysical Union.

McMillan, L. A., Rivett, M. O., Wealthall, G. P., Zeeb, P., & Dumble, P. (2018). Monitoring well utility in a heterogeneous DNAPL source zone area: Insights from proximal multilevel sampler wells and sampling capture-zone modelling. *Journal of Contaminant Hydrology, 210*, 15-30. https://doi.org/10.1016/j.jconhyd.2018.02.001

Miller, C. T., Christakos, G., Imhoff, P. T., McBride, J. F., & Pedit, J. A. (1998a). Multiphase flow and transport modeling in heterogeneous porous media: challenges and approaches. *Advances in Water Resources, 21*(2), 77-120. https://doi.org/10.1016/S0309-1708(96)00036-X

Miller, C. T., Wilson, C. S., Gleyzer, S. N., Farthing, M. W., McBride, J. F., & Imhoff, P. T. (1998b). NAPL-aqueous phase mass transfer in heterogeneous porous media. *Groundwater Quality: Remediation and Protection. 250*, pp. 141-148. Tubingen, Germany: International Association of Hydrological Sciences.

Mobile, M. A., Widdowson, M. A., & Gallagher, D. L. (2012). Multicomponent NAPL Source Dissolution: Evaluation of Mass-Transfer Coefficients. *Environmental Science & Technology, 46*(18), 10047-10054. https://doi.org/10.1021/es301076p

Mobile, M., Widdowson, M., Stewart, L., Nyman, J., Deeb, R., Kavanaugh, M., . . . Gallagher, D. (2016). In-situ determination of field-scale NAPL mass transfer coefficients: Performance, simulation and analysis. *Journal of Contaminant Hydrology, 187*, 31-46. https://doi.org/10.1016/j.jconhyd.2016.01.010

National Research Council. (2005). *Contaminants in the subsurface: Source zone assessment and remediation.* Washington, D.D.: The National Academic Press.

Park, E., & Parker, J. C. (2005). Evaluation of an upscaled model for DNAPL dissolution kinetics in heterogeneous aquifers. *Advances in Water Resources*, 1280-1291. https://doi.org/10.1016/j.advwatres.2005.04.002

Parker, J. C., & Park, E. (2004). Modeling field-scale dense nonaqueous phase liquid dissolution kinetics in heterogeneous aquifers. *Water Resources Research, 2004*. https://doi.org/10.1029/2003WR002807

Parker, J. C., Kim, U., Widdowson, M., Kitandis, P., & Gentry, R. (2010). Effects of model formulation and calibration data on uncertainty in dense nonaqueous phase liquids source dissolution predictions. *Water Resources Research, 46*, W12517. https://doi.org/10.1029/2010WR009361

Prieto-Estrada, A. E., Widowson, M., & Stewart, L. (2022a). Quantifying DNAPL source zone longevity with upscaled modeling: practical insights from flow-cell experiments and uncertainty analyses. *Authorea*. https://doi.org/10.22541/essoar.167169841.11588321/v1

Prieto-Estrada, A. E., Widdowson, M., & Stewart, L. (2022b). Numerical modeling and data-worth analysis for characterizing the architecture and dissolution rates of a multicomponent DNAPL source. *Authorea*. https://doi.org/10.22541/essoar.167214630.01839069/v1

Rivett, M. O., & Feenstra, S. (2005). Dissolution of an Emplaced Source of DNAPL in a Natural Aquifer Setting. *Environmental Science & Technology, 39*, 447-455. https://doi.org/10.1021/es040016f

Rivett, M. O., Dearden, R. A., & Wealthall, G. P. (2014). Architecture, persistence and dissolution of a 20 to 45 year old trichloroethene DNAPL source zone. *Journal of Contaminant Hydrology, 170*, 95-115.

Saenton, S., & Illangasekare, T. H. (2007). Upscaling of mass transfer rate coefficient for the numerical simulation of dense nonaqueous phase liquid dissolution in heterogeneous aquifers. *Water Resources Research, 43*(2). https://doi.org/10.1029/2005WR004274

Stewart, L. D., Chambon, J. C., Widdowson, M. A., & Kavanaugh, M. C. (2022). Upscaled modeling of complex DNAPL dissolution. *Journal of Contaminant Hydrology, 244*, 103920. https://doi.org/10.1016/j.jconhyd.2021.103920

Stroo, H. F., Leeson, A., Marqusee, J. A., Johnson, P. C., Ward, C. H., Kavanaugh, M. C., . . . Unger, M. (2012). Chlorinated Ethene Source Remediation: Lessons Learned. *Environmental Science & Technology*, *46*, 6438−6447. https://doi.org/10.1021/es204714w

Waddill, D. W., & Widdowson, M. A. (2000). *SEAM3D: A numerical model for three-dimensional solute transport and sequential electron acceptor-based bioremediation in groundwater*. ERDC/EL TR- 00-18. U.S. Army Engineer Research and Development Center, Vicksburg, MS.

Watermark Numerical Computing. (2018). *PEST. Model-Independent Parameter Estimation. User Manual Part I: PEST, SENSAN, and Global Optimisers.* Retrieved from pesthomepage: https://pesthomepage.org/documentation

Wyllie, M. R. (1962). Relative permeability. In T. Frick, & W. Taylor, *Petroleum Production Handbook* (Vol. II: Reservoir Engineering, pp. 25.1-25.14). New York: McGraw-Hill.

Zhang, X., Ma, F., Yin, S., Wallace, C. D., Soltanian, M. R., Dai, Z., . . . Lu, X. (2021). Application of upscaling methods for fluid flow and mass transport in multi-scale heterogeneous media: A critical review. *Applied Energy, 303*, 117603. https://doi.org/10.1016/j.apenergy.2021.117603

Zheng, C., & Bennett, G. D. (2002). Chapter 10: Building a Contraminant Transport Model. In C. Zheng, & G. D. Bennett, *Applied Contaminant Transport Modeling* (Second ed., pp. 271-29). New York: John Wiley and Sons, Inc.

Chapter 5. Conclusions

Multiple findings in this work contributed to the development of quantitative approaches for estimating rates of DNAPL dissolution in groundwater. Given the uncertainty of DNAPL mass transfer processes and source zone characterization challenges at field sites, decision-support modeling tools must be able to assimilate multiple data to quantify and reduce environmental risks. This research combined numerical and upscaled modeling approaches with uncertainty analysis tools to elucidate upon advantages, limitations, and recommendations on data assimilation techniques for estimating source zone parameters and DNAPL depletion timeframes. High-resolution experimental datasets were leveraged to investigate adequate model parameterization methods to avoid predictive bias. Research findings are summarized as follows:

Chapter 2. Quantifying DNAPL source zone longevity with upscaled modeling: practical insights from flow-cell experiments and uncertainty analyses.

Oftentimes there is a lack of consistent groundwater monitoring data representative of final stages of DNAPL depletion, or of source zone delineation measurements. Also, even if there are historical release records, measuring the amount of entrapped DNAPL mass and saturations by direct characterization technologies is not possible. If pertaining to high-saturation accumulations (e.g., pools), DNAPL mass, vertical dispersivity (α_T), and dissolution-tailing (β) coefficients were shown to regulate DNAPL longevity by sensitivity analyses of volume-averaged (VA) models of flow-cell experiments. While experimental effluent profiles were not sensitive to systematic variations of DNAPL pool parameters, first-order second-moment (FOSM) analyses revealed that uncertainties on mass and α_T values could be significantly constrained by monitoring of pool dissolution, whereas β could not. Predicting source depletion scenarios must thereby express remaining model uncertainties, including the plausible variability of β parameters.

Coupling the VA modeling system with an iterative parameter-ensemble smoother (iES) facilitated the stochastic expression of model uncertainties on predictions of source zone longevity. Generating unbiased, low-density probability distributions of source depletion timeframes was possible by assuming prior knowledge of coarse DNAPL delineation with no effluent records.

However, history-matching of multi-stage and non-monotonic dissolution profiles required increasing model parameterization complexity to avoid biasing (underestimating) predictions of source longevity. Increasing the number of DNAPL mass accumulations commensurate with dissolution stages, observed in monitoring profiles, constrained unbiased model predictions. Likewise, although sensitivity and nonlinear uncertainty analyses showed that low-saturation ganglia dissolution did not impact source longevity estimates, inverse modeling of discharge concentration peaks excluding ganglia parameters significantly underestimated residual saturations. In practice, incorrectly estimating low saturations could mislead injection-based remedial designs aimed at reducing source discharge concentrations.

Regardless of source zone architectural complexities, FOSM data-worth analyses emphasized the importance of discharge concentrations reflecting final DNAPL depletion stages for constraining source longevity estimates. Nonetheless, inflection points along the complex dissolution profile of a heterogeneous source zone were also linked to reductions on VA model uncertainties. In this case, inverse VA modeling with iES accurately reproduced the effluent profile by excluding the α_T parameter from the most downgradient high-saturation DNAPL mass, responsible for the heterogenous source zone longevity. This finding showed value in the mass transfer coefficient generalization within the VA framework, as exclusive ganglia vs pool dissolution coefficients would not account for geological heterogeneity controls on mass transfer processes, regardless of DNAPL saturation distributions. In summary, this chapter elucidated upon VA model construction strategies suitable for quantifying the uncertainty of DNAPL longevity driven by data availability.

Chapter 3. Numerical modeling and data-worth analysis for characterizing the architecture and dissolution rates of a multicomponent DNAPL source.

Simultaneously characterizing the mass, architecture, and dissolution rates of a multicomponent (chloroform TCM, trichlorethylene TCE, perchloroethylene PCE) DNAPL source zone was achieved through inverse numerical modeling of a high-resolution monitoring dataset. The source zone architecture was inferred from breakthrough analysis of multilevel-sampling (MLS) concentrations indicative of upgradient DNAPL mass. The MLS profiles allowed for the parsimonious parameterization of DNAPL zones in a 3D numerical model of mass transfer and

aqueous-phase transport, representing a field aquifer test cell. The simultaneous estimation of spatially-varying, component-specific (i) initial mass transfer coefficients ($k_{i,0}^N$) and soil DNAPL concentrations (C_0^N), from MLS profiles only, underestimated initial DNAPL mass and longevity. This underestimation resulted from inverse modeling using a parallelized gradient-based optimization routine, in contrast to stochastic parameter optimization with iES. The latter allowed for identifying MLS and mass discharge (MD) measurements responsible for parameter bias, referred to as prior-data conflicts (PDC).

Prior-based Monte Carlo analyses showed that initial peaks of contaminant concentrations could not be simulated by randomized parameter realizations within uncertainty bounds, given the model design (including fixed transport parameter values). In turn, FOSM data-worth analysis showed that maximum MLS and MD concentrations constrained $k_{i,0}^N$ values, whereas dissolution tailing of the most soluble and least by volume DNAPL component (TCM) constrained C_0^N values. Accurate characterization of source zone architecture and depletion was thereby achieved by removing PDC values and including both MLS and MD measurements for history matching. While MLS tailing signatures were truncated for history matching because of excessive noise driven by water table fluctuations, complete MD signatures allowed for spreading data noise across all DNAPL zones, improving the estimation of initial source mass.

This investigation elucidated upon the advantages and limitations on inverse modeling of high-resolution monitoring data for decision support at field sites. Analyses of DNAPL depletion by methanol-enhanced dissolution produced significantly different results on the basis of residual saturation assumptions reported by the experiment authors. These results highlighted the value of inverse modeling for source zone characterization, where two distinctly calibrated models agreed on the amount of DNAPL mass eliminated by natural groundwater dissolution. However, multiscale architectural and dissolution heterogeneities, identified on MLS profiles, were linked to the propensity for underestimating source zone mass and longevity, as accurate estimates were constrained by final DNAPL depletion stages. Although such measurements were available for the simulated experiment, the mass depletion parameter β could not be constrained. In summary, these novel results demonstrated the benefit of coupling inverse numerical modeling with linear and

nonlinear uncertainty analysis methods for the effective assimilation of high-resolution monitoring data, supporting characterization efforts of DNAPL source zones.

Chapter 4. Scaling of DNAPL dissolution rates: Numerical modeling analyses.

As demonstrated in the previous chapters, if available, history-matching data may bias mass transfer parameters and predictions of source longevity without adequate uncertainty constraints. Exploring the variability of source longevity with numerical discretization of VA models of two flow-cell experiments of DNAPL dissolution showed a relationship between grid resolution and source architecture, providing a methodology for scaling estimable, bulk mass transfer coefficients (k^{VA}) to constrain grid-scale, lumped-process mass transfer coefficients (k^{S3D}) *a priori* (prior to history-matching). Scaling of k^{VA} coefficients as a function of numerical model layering and source downgradient length allowed for reproducing VA physical predictions of DNAPL pool depletion in 2D numerical domains, where transverse hydrodynamic dispersion regulated the sensitivity of k^{S3D} coefficients with respect to experimental MD rates. Decreasing sensitivity of k^{S3D} coefficients with increasing model layering was found independent of source zone dimensions, model layer thicknesses, and α_T values used to simulate the experiments. However, numerical analyses of both experiments coincided on the number of model layers where downgradient discretization (ΔX) controlled the variability of source longevity, caused by aqueous dispersive transport across DNAPL grid blocks.

Although only models with 10 or more layers showed sensitivity to ΔX driven by dispersive transport, all 2D models required scaling of k^{VA} coefficients to reproduce bulk effluent rates and approximate VA estimates of pool mass depletion. Accurate numerical approximations required empirical adjustment of a scaling parameter η, decreasing known downgradient source lengths with increasing model layering to obtain k^{S3D} values a priori. The deterministic numerical analyses were supported by inverse k^{S3D} estimation results, showing minimal variability with ΔX, and overestimation (non-unique solutions) of k^{S3D} driven by monitoring data availability and source zone vertical discretization (ΔZ). Similarly, increasing k^{S3D} values up to TCE and PCE aqueous solubility limits in models with discretized vertical pool heights ($\Delta Z \leq 1$ cm) resulted in numerical error and underestimation of source longevity, while fitting early dissolution data. Empirical k^{VA}

scaling proved useful for constraining the uncertainty of k^{S3D} coefficients on the basis of model layering, source zone dimensions, and α_T coefficients relevant to DNAPL pool dissolution. This research showed that merging VA and numerical modeling provides an efficient framework for reducing uncertainties on DNAPL source dissipation at multiple scales of spatial resolution.

5.1. Recommendations for Future Research and Development

Future research is needed to discern the role of hydrodynamic dispersion not captured by the VA model vs grid resolution effects on DNAPL mass transfer in discretized domains, including field datasets of historical mass discharge monitoring and source zone characterization. Chapter 4 demonstrated a relationship between vertical dispersive transport and scaling of k^{VA} coefficients to grid resolutions below MD monitoring scales. However, k^{VA} scaling may not be required in layered models where vertical dimensions of grid DNAPL zones match the monitoring scale, such as the multilevel transect in Chapter 3. The DNAPL mass and dimensions of grid parameter zones in the Borden numerical model (Chapter 3) could be used to define upscaled source reference volumes (V_S), and architectural volumes such that $V_a \leq V_S$, in order to calculate a range of plausible k^{VA} values. These could be contrasted with previously estimated k^{S3D} values to evaluate the need for k^{VA} scaling, should the latter not encompass the former. This comparison would provide further insights on constraining the uncertainty of k^{S3D} parameters in numerical models of multicomponent sources. Furthermore, Chapter 4 showed that single-cell 1D numerical models reproduced MD rates and DNAPL longevity using k^{VA} values, suggesting value in developing multi-rate mass transfer capabilities for single DNAPL grid blocks.

Specifying multiple k^{S3D} values in a single grid block would enable the efficient numerical simulation of multistage dissolution rates caused by heterogeneous DNAPL saturation distributions. Such distributions can be inferred from source characterization data, including borehole logs, laser induced fluorescence, membrane interface probes, and aquifer profiling tools, providing uncertainty ranges for k^{S3D} coefficients using VA model concepts. This approach could support modeling of DNAPL source and plume attenuation processes in heterogenous aquifer systems, including dual-domain transport, biodegradation, back-diffusion, and additional mechanisms using computationally efficient numerical grids. By gaining efficiency, numerical

models can be coupled with uncertainty analysis tools to quantify environmental risk and support groundwater remedial designs.

Appendices

Appendix A: Supplemental Information to Chapter 3.

Mathematical Model

Solute Transport Equation

$$-\frac{\partial}{\partial x_i}(v_i C^k) + \frac{\partial}{\partial x_i}\left(D_{ij}\frac{\partial C^k}{\partial x_j}\right) + \frac{q_s C_s^k}{n_e} + R^{N,k} = \left(1 + \frac{K_d^k \rho_b}{\theta}\right)\frac{\partial C^k}{\partial t} \qquad \text{(A-1)}$$

C^k	**M L^{-3}**	*Aqueous phase concentration of species k*
x_i	**L**	*Distance along cartesian coordinate axis*
t	**T**	*Time*
v_i	**L T^{-1}**	*Average pore water velocity*
D_{ij}	**L^2 T^{-1}**	*Hydrodynamic dispersion coefficient tensor*
q_s	**T^{-1}**	*Volumetric flux of water per unit volume of aquifer representing fluid sources (positive) and sinks (negative)*
C_s^k	**M L^{-3}**	*Concentration of the source or sink flux for species k*
K_d^k	**L^3 M^{-1}**	*Distribution coefficient*
ρ_b	**M L^{-3}**	*Bulk density*
θ	**L^3 L^{-3}**	*Aquifer porosity*
$R^{N,k}$	**M L^{-3} T^{-1}**	*Source term representing NAPL dissolution for species k*

NAPL mass balance term

$$\frac{\partial C^{N,k}}{\partial t} = -\frac{\theta}{\rho_b} R^{N.k} \qquad \text{(A-2)}$$

$C^{N,k}$	**M L^{-3}**	*NAPL phase concentration of species k*

NAPL source term

$$R^{N.k} = k^{N,k}\left(C_{eq}^{k} - C^{k}\right) \quad \text{(A-3)}$$

$k^{N,k}$	$\mathbf{T^{-1}}$	*Lumped mass transfer coefficient of species k*
C_{eq}^{k}	$\mathbf{M\ L^{-3}}$	*Aqueous-phase equilibrium concentration of species k calculated using Raoult's Law*

Table A-1. Input parameters of groundwater flow and solute transport model including NAPL properties

Model Parameter	Value	Data Source
Hydraulic conductivity (m/d)	2.0	Broholm et al. 1999
Porosity (%)	33.0	Broholm et al. 1999
Longitudinal dispersivity (cm)	5.0	Mobile et al. 2012
Transverse horizontal dispersivity (cm)	0.5	Mobile et al. 2012
Transverse vertical dispersivity (cm)	0.05	Mobile et al. 2012
TCM sorption coefficient (m^3/g)	3.0×10^{-8}	Mobile et al. 2012
TCE sorption coefficient (m^3/g)	5.0×10^{-8}	Mobile et al. 2012
PCE sorption coefficient (m^3/g)	1.3×10^{-7}	Mobile et al. 2012
Soil bulk density (g/m^3)	1.65×10^{6}	Mobile et al. 2012
TCM initial NAPL mass fraction (%)	9.60	Broholm et al. 1999
TCE initial NAPL mass fraction (%)	37.9	Broholm et al. 1999
PCE initial NAPL mass fraction (%)	52.5	Broholm et al. 1999
TCM ideal solubility (mg/L)	8700	Broholm et al. 1999
TCE ideal solubility (mg/L)	1400	Broholm et al. 1999
PCE ideal solubility (mg/L)	240	Broholm et al. 1999
TCM molecular weight (g/mol)	119.4	Rivett et al. 2001
TCE molecular weight (g/mol)	131.4	Rivett et al. 2001
PCE molecular weight (g/mol)	165.8	Rivett et al. 2001
TCM density (g/cm^3)	1.48	Broholm et al. 1999
TCE density (g/cm^3)	1.46	Broholm et al. 1999
PCE density (g/cm^3)	1.62	Broholm et al. 1999

Table A-2. Parameter values used to calculate percentages of initial NAPL mass removed by natural dissolution and methanol flushing presented in Table 5.

Parameter	TCM	TCE	PCE	Total	Source
Initial NAPL (L)	0.48	1.895	2.625	5	Mobile et al. (2012)
Initial NAPL (g)	739.2	2918.3	4042.5	7700	Mobile et al. (2012)
Remaining NAPL (L) [(1)]	0.001	0.34	1.24	1.58	Broholm et al. (1999)
Remaining/Initial NAPL [(1)]	0.002	0.179	0.472	0.32	Calculated
Remaining NAPL (g) [(1)]	**1.54**	**523.6**	**1909.6**	**2434.74**	**Calculated**
Remaining NAPL Fractions [(1)]	0.0006	0.2151	0.7843	1	Calculated
Remaining NAPL (L) [(2)]	0.002	0.532	1.940	2.47[^]	Calculated / Broholm et al. (1999)
Remaining/Initial NAPL [(2)]	0.0033	0.2807	0.7390	0.49	Calculated
Remaining NAPL (g) [(2)]	**2.4**	**819.1**	**2987.3**	**3808.8**	**Calculated**

[(1)] Post-excavation volumes (L) of each NAPL component provided by Broholm et al. (1999) assuming a homogeneous 3.6% NAPL saturation of the pore space in all excavation layers. [^]Total post-excavation NAPL volume (L) provided by Broholm et al. (1999) assuming a 20% NAPL saturation in excavation layer 2 and a 3.6% saturation in other soil layers. [(2)] Remaining volume (L) and mass (g) calculated for each NAPL component using the individual remaining fractions in [(1)] reported by Broholm et al. (1999), applied to the total remaining NAPL volume of [^]2.47 L also reported by Broholm et al. (1999).

Appendix B: Supplemental Information to Chapter 4

SEAM3D Mathematical Model (Waddill & Widdowson, 2000)

Solute Transport Equation

$$-\frac{\partial}{\partial x_i}(v_i C^k) + \frac{\partial}{\partial x_i}\left(D_{ij}\frac{\partial C^k}{\partial x_j}\right) + \frac{q_s C_s^k}{n_e} + R^{N,k} = \left(1 + \frac{K_d^k \rho_b}{\theta}\right)\frac{\partial C^k}{\partial t} \qquad \text{(B-4)}$$

C^k	**M L^{-3}**	*Aqueous phase concentration of species k*
x_i	**L**	*Distance along cartesian coordinate axis*
t	**T**	*Time*
v_i	**L T^{-1}**	*Average pore water velocity*
D_{ij}	**L^2 T^{-1}**	*Hydrodynamic dispersion coefficient tensor*
q_s	**T^{-1}**	*Volumetric flux of water per unit volume of aquifer representing fluid sources (positive) and sinks (negative)*
C_s^k	**M L^{-3}**	*Concentration of the source or sink flux for species k*
K_d^k	**L^3 M^{-1}**	*Distribution coefficient*
ρ_b	**M L^{-3}**	*Bulk density*
θ	**L^3 L^{-3}**	*Aquifer porosity*
$R^{N,k}$	**M L^{-3} T^{-1}**	*Source term representing NAPL dissolution for species k*

NAPL mass balance term

$$\frac{\partial C^{N,k}}{\partial t} = -\frac{\theta}{\rho_b} R^{N.k} \qquad \text{(B-5)}$$

$C^{N,k}$	**M L^{-3}**	*NAPL phase concentration of species k*

NAPL source term

$$R^{N.k} = \frac{1}{\theta V_S}\frac{dm_n}{dt} = K^{N,k}\left(C_{eq}^{k} - C^{k}\right) \tag{B-6}$$

$K^{N,k}$	$\mathbf{T^{-1}}$	*Lumped mass transfer coefficient of species k*
C_{eq}^{k}	$\mathbf{M\ L^{-3}}$	*Aqueous-phase equilibrium concentration of species k calculated using Raoult's Law*
V_S	$\mathbf{L^3}$	*Volume of source grid block containing NAPL mass*
m_n	**M**	*NAPL mass*

Volume-Averaged (VA) Mathematical Model (Stewart et al., 2021)

$$\left(1 - S_n + \frac{K_d^k \rho_b}{\theta}\right)\frac{d\bar{C}^k}{dt} = -\frac{Q}{\theta V_S}\bar{C}^k + \frac{1}{\theta V_S}\sum_{a=1}^{A}\frac{dm_a^k}{dt} \tag{B-7}$$

$$\frac{1}{V_S}\sum_{a=1}^{A}\frac{dm_a^k}{dt} = -\sum_{a=1}^{A}K_a^k\left(C_{a,eq}^{k} - C_{a,0}^{k}\right) \tag{B-8}$$

$\bar{C}^k$	**M L^{-3}**	*Average aqueous-phase concentration of species k*
t	**T**	*Time*
Q	**L^3 T**	*Volumetric flow rate through V_S*
V_S	**L^3**	*Source zone reference volume containing all NAPL accumulations*
m_a^k	**M**	*Mass of NAPL accumulation "a" for species k*
K_a^k	**T^{-1}**	*Bulk, time-varying mass transfer coefficient of NAPL accumulation "a" for species k*
K_d^k	**L^3 M^{-1}**	*Distribution coefficient for species k*
$C_{a,eq}^k$	**M L^{-3}**	*Aqueous-phase equilibrium concentration from NAPL accumulation "a" for species k calculated using Raoult's Law*
S_n	–	*Average NAPL saturation in source zone*
θ	**L^3 L^{-3}**	*Aquifer porosity*
$C_{a,0}^k$	**M L^{-3}**	*Average aqueous-phase concentration of species k entering the sub-volume of NAPL accumulation "a"*

Discretization of Bulk Mass Transfer Coefficients

Root mean squared error (RMSE) values between simulated (sim_i) and measured (obs_i) mass discharge rates were calculated as:

$$RMSE = \left[\frac{1}{N}\sum_{i=1}^{N}(sim_i - obs_i)^2\right]^{1/2} \quad \text{(B-9)}$$

where N is the number of observations.

Table B-1. Source zone discretization of Pool 1, including initial mass transfer coefficients k_0^{S3D} estimated with Equation 4-7. Coefficients estimated with Equations 4-8 and 4-9 using variable η values are included for comparison (Table 4-3).

ΔX_p (cm)	22	11	4.4	2.75	2	$\widetilde{X}_p$
ΔZ_S (cm)	**k_0^{S3D} (d^{-1})**					
19	1.018	1.528	2.690	3.653	4.525	1.018
9.5	2.037	3.056	5.380	7.306	9.050	2.296
3.8	5.092	7.639	13.450	18.265	22.626	6.742
1.9	10.185	15.278	26.901	36.529	45.252	16.576
1	19.351	29.028	51.112	69.405	85.979	41.165
0.5	38.701	58.056	102.223	138.811	171.958	99.314

Table B-2. RMSE values obtained from Equation 4-7 (Table B-1) with respect to effluent data of Pool 1.

ΔX_p (cm)	22	11	4.4	2.75	2
ΔZ_S (cm)	**RMSE**				
19	0.187	0.190	0.178	0.102	0.042
9.5	0.194	0.192	0.173	0.092	0.043
3.8	0.186	0.173	0.146	0.062	0.053
1.9	0.137	0.122	0.097	0.042	0.064
1	0.086	0.074	0.056	0.044	0.071
0.5	0.056	0.049	0.043	0.052	0.076

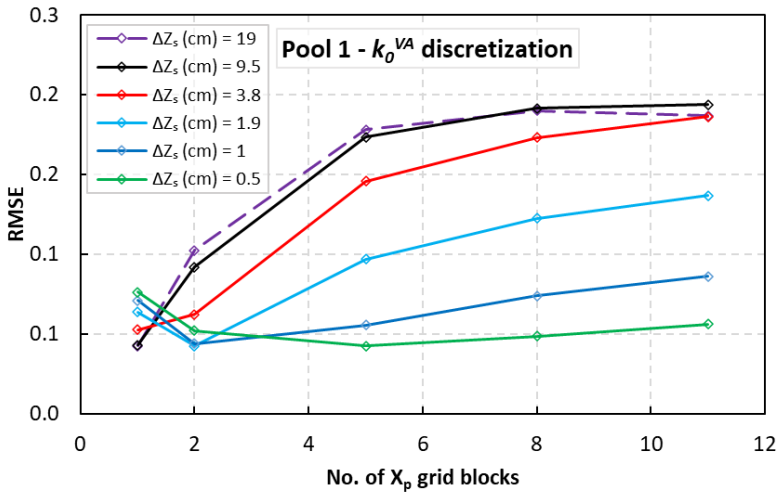

Figure B-1. Plot of Table B-2 results.

Table B-3. Source zone discretization of Pool 2, including initial mass transfer coefficients k_0^{S3D} estimated with Equation 4-7. Coefficients estimated with Equations 4-8 and 4-9 using variable η values are included for comparison (Table 4-3).

ΔX_p (cm)	230	115	46	28.75	23	$\widetilde{X}_p$
ΔZ_S (cm)	**k_0^{S3D} (d^{-1})**					
45	0.008	0.012	0.022	0.030	0.035	0.008
22.5	0.016	0.025	0.044	0.059	0.069	0.018
9	0.041	0.061	0.109	0.149	0.173	0.054
4.5	0.082	0.123	0.218	0.297	0.346	0.123
1	0.367	0.553	0.981	1.337	1.555	0.974

Table B-4. RMSE values obtained from Equation 4-7 (TableB-S3) with respect to effluent data of Pool 2.

ΔX_p (cm)	230	115	46	28.75	23
ΔZ_S (cm)	**RMSE**				
45	0.311	0.261	0.174	0.058	0.015
22.5	0.247	0.211	0.144	0.047	0.018
9	0.126	0.112	0.080	0.022	0.030
4.5	0.048	0.043	0.030	0.017	0.042
1	0.019	0.021	0.026	0.039	0.055

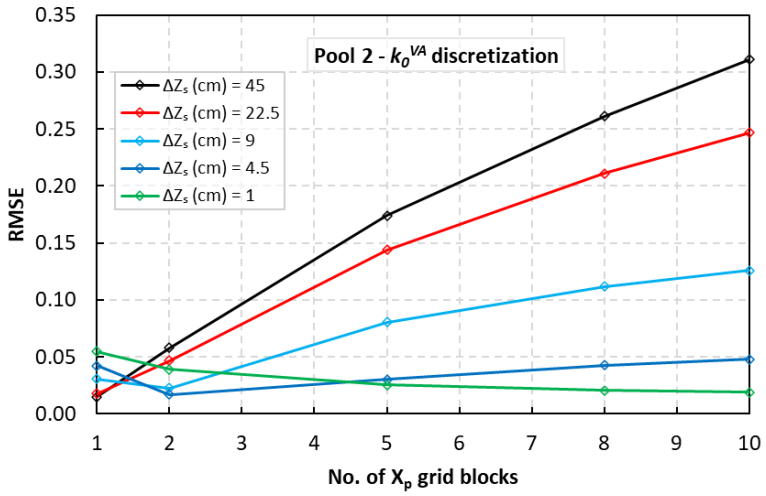

Figure B-2. Plot of Table S4 results.

Inverse Numerical Modeling

Table B-5. TOR results of inverse numerical modeling of Pool 1 with PEST.

ΔX_p	22 cm		11 cm		4.4 cm		2.75 cm		2 cm	
ΔZ_S	***k_0^{S3D}***	**TOR**	***k_0^{S3D}***	**TOR**	***k_0^{S3D}***	**TOR**	***k_0^{S3D}***	**TOR**	***k_0^{S3D}***	**TOR**
cm	d^{-1}	days	d^{-1}	days	d^{-1}	days	d^{-1}	days	d^{-1}	days
19	0.971	30.04	0.971	30.04	0.972	30.04	0.977	29.94	1.010	29.05
9.5	2.022	30.29	2.023	30.23	2.026	30.23	2.050	29.95	2.189	28.26
3.8	5.703	30.82	5.705	30.85	5.726	30.75	5.849	30.16	6.798	26.64
1.9	13.678	31.13	13.683	31.13	13.714	30.96	13.926	30.46	17.283	25.55
1	34.251	29.94	34.400	29.82	34.248	29.84	32.263	30.12	40.403	24.90
0.5	95.576	28.20	95.847	28.13	92.965	28.29	83.856	28.63	100.700	24.37

Table B-6. RMSE values of inverse numerical modeling of Pool 1 with PEST.

ΔX_p	22 cm		11 cm		4.4 cm		2.75 cm		2 cm	
ΔZ_S	k_0^{S3D}	RMSE	k_0^{S3D}	RMSE	k_0^{S3D}	RMSE	k_0^{S3D}	RMSE	k_0^{S3D}	RMSE
cm	d^{-1}	-	d^{-1}	-	d^{-1}	-	d^{-1}	-	d^{-1}	-
19	0.971	0.043	0.971	0.043	0.972	0.043	0.977	0.043	1.010	0.042
9.5	2.022	0.042	2.023	0.042	2.026	0.042	2.050	0.042	2.189	0.042
3.8	5.703	0.041	5.705	0.041	5.726	0.041	5.849	0.041	6.798	0.041
1.9	13.678	0.041	13.683	0.041	13.714	0.041	13.926	0.041	17.283	0.041
1	34.251	0.041	34.400	0.041	34.248	0.041	32.263	0.043	40.403	0.043
0.5	95.576	0.042	95.847	0.042	92.965	0.042	83.856	0.045	100.700	0.046

Table B-7. TOR results of inverse numerical modeling of Pool 2 with PEST.

ΔX_p	23 cm		28.75 cm		46 cm		115 cm		230 cm	
ΔZ_S	k_0^{S3D}	TOR	k_0^{S3D}	TOR	k_0^{S3D}	TOR	k_0^{S3D}	TOR	k_0^{S3D}	TOR
cm	d^{-1}	years	d^{-1}	years	d^{-1}	years	d^{-1}	years	d^{-1}	years
45	0.008	32.82	0.008	32.82	0.008	32.82	0.008	32.58	0.008	31.49
22.5	0.018	32.70	0.017	32.70	0.017	32.70	0.017	32.34	0.017	30.17
9	0.061	32.16	0.051	32.32	0.049	32.16	0.049	31.15	0.049	26.91
4.5	0.191	30.24	0.142	30.25	0.134	30.06	0.133	28.53	0.133	23.12
^1	1.707	26.38	1.707	26.38	1.707	25.96	1.707	24.72	1.707	22.40

^All k_0^{S3D} parameters were truncated at the indicated value to avoid excessive TOR underestimation.

Table B-8. RMSE values of inverse numerical modeling of Pool 2 with PEST.

ΔX_p	23 cm		28.75 cm		46 cm		115 cm		230 cm	
ΔZ_S cm	k_0^{S3D} d^{-1}	RMSE -	k_0^{S3D} d^{-1}	RMSE -	k_0^{S3D} d^{-1}	RMSE -	k_0^{S3D} d^{-1}	RMSE -	k_0^{S3D} d^{-1}	RMSE -
45	0.008	0.015	0.008	0.015	0.008	0.015	0.008	0.015	0.008	0.015
22.5	0.018	0.015	0.017	0.015	0.017	0.015	0.017	0.015	0.017	0.015
9	0.061	0.015	0.051	0.015	0.049	0.015	0.049	0.015	0.049	0.015
4.5	0.191	0.015	0.142	0.015	0.134	0.015	0.133	0.015	0.133	0.015
^1	1.707	0.018	1.707	0.018	1.707	0.018	1.707	0.018	1.707	0.020

^All k_0^{S3D} parameters were truncated at the indicated value to avoid excessive TOR underestimation.

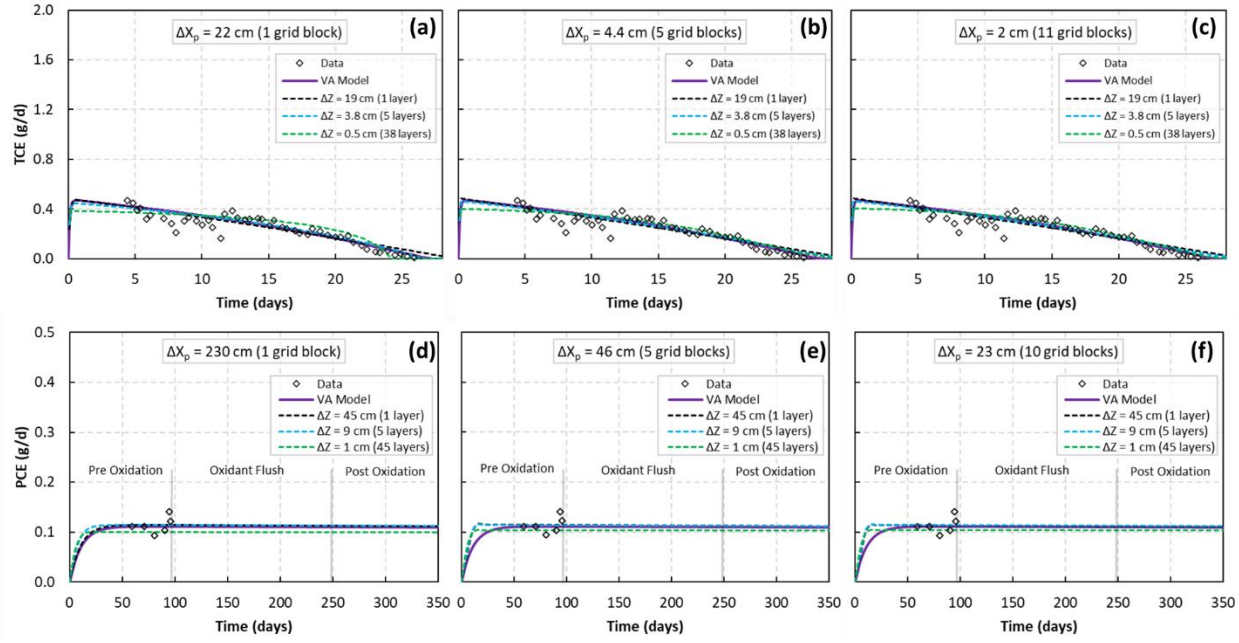

Figure B-3. Comparison between measured and inverse numerical modeling of experimental mass discharge (MD) rates. Panels (a) through (c) correspond to Pool 1, whereas panels (d) through (f) correspond to Pool 2.

Time Step Size Comparison

Criteria for maximum transport step size (Δt) for a stable solution (Zheng & Bennett, 2002):

$$\Delta t \leq \frac{0.5\ R}{\frac{D_{xx}}{(\Delta X)^2} + \frac{D_{zz}}{(\Delta Z)^2}} \tag{B-10}$$

where D_{xx} and D_{xx} are the principal components of the dispersion coefficient. Considering the numerical modeling conditions of Pools 1 and 2:

$$\Delta t \leq \frac{0.5}{\frac{\alpha_L v_x}{(\Delta X)^2} + \frac{\alpha_T v_x}{(\Delta Z)^2}} \tag{B-11}$$

where $v_x = q/\theta$ is the contaminant velocity. Considering Figure 4-10,

Pool 1:

$$\Delta t \leq \frac{0.5}{\frac{0.025\ cm\ \times 217.07 cm/d}{(4.4\ cm)^2} + \frac{0.1\ cm\ \times 217.07 cm/d}{(0.5\ cm)^2}} \leq 0.0057\ d \tag{B-12}$$

Pool 2:

$$\Delta t \leq \frac{0.5}{\frac{0.025\ cm\ \times 20.81 cm/d}{(46\ cm)^2} + \frac{0.04\ cm\ \times 20.81\ cm/d}{(1\ cm)^2}} \leq 0.6\ d \tag{B-13}$$

Compared to GCG (generalized conjugate gradient) solver implicit calculations:

Pool 1: Δt 0.00168 days
Pool 2 : Δt 0.027645 days

References

Stewart, L. D., Chambon, J. C., Widdowson, M. A., & Kavanaugh, M. C. (2022). Upscaled modeling of complex DNAPL dissolution. *Journal of Contaminant Hydrology, 244*, 103920. https://doi.org/10.1016/j.jconhyd.2021.103920

Waddill, D. W., & Widdowson, M. A. (2000). *SEAM3D: A numerical model for three-dimensional solute transport and sequential electron acceptor-based bioremediation in groundwater*. ERDC/EL TR- 00-18. U.S. Army Engineer Research and Development Center, Vicksburg, MS.

Zheng, C., & Bennett, G. D. (2002). Chapter 10: Building a Contraminant Transport Model. In C. Zheng, & G. D. Bennett, *Applied Contaminant Transport Modeling* (Second ed., pp. 271-29). New York: John Wiley and Sons, Inc.

Appendix C: Model Calibration

In this work model calibration was undertaken with PEST and PEST_HP software, which can be downloaded at no cost from the PEST website at https://pesthomepage.org/programs, including all the necessary user manuals and documentation at https://pesthomepage.org/documentation. The PEST website also provides free educational content, including a series of videos, webinars, and tutorials. Another useful website is provided by the Groundwater Modelling Decision Support Initiative (GMDSI) at https://gmdsi.org/. This website also provides free educational content, including more videos, tutorials, worked examples, and a series of PEST roadmaps with practical and theoretical considerations.

This appendix provides some key points and practical considerations for using PEST and PEST_HP, referring to their corresponding user manuals as necessary. Both programs estimate model input parameters by minimizing an objective function (Φ) defined by observation groups and weights using the Gauss-Levenberg-Marquardt (GLM) algorithm and Jacobian sensitivity matrices calculated using parameter finite differences (Doherty, 2015). All PEST versions, including PEST++iES (Appendix E) require a *control, template* (for input parameters), *and instruction* (for retrieving observations) files. PEST requires models to use text (.txt) files for model input and output files. Examples are provided for calibrating SEAM3D models, including practical suggestions.

PEST control file (.pst)

The control file contains information on model parameters, observations, and optimization settings. Refer to the PEST User Manual Part I for a detailed description of the control data sections and corresponding variable definitions. Below is an example of a control file used to calibrate a single-cell SEAM3D model of Pool 2 in Chapter 4. Purple text in parenthesis clarifies key points and should not be included in the control file. Variables not explained in the parenthesis can be left to the shown values shown or consult the PEST User Manual Part I for a detailed explanation.

pcf (there is no specific spacing between variable values on each line below)

* control data

restart estimation

2 15 1 0 1 (number of parameters, observations, parameter groups, prior information equations, and observation groups)

1 1 single point 1 0 0 (number of template and instruction files)

20.0 -3.0 0.3 0.01 10

10.0 10.0 1.0e-3 (maximum relative [untransformed parameters] and factor [log-transformed parameters] change that a parameter is allowed to undergo between optimization iterations)

0.1 1

5 0.005 3 3 0.005 3 (maximum number of iterations – consult manual for special functionality such as running the model once or calculating a Jacobian matrix)

1 1 1 parsaveitn (saves optimal parameter values after each iteration in a separate file)

* singular value decomposition

1

1 5.0e-7 (set to number of adjustable parameters or consult manual)

1

* parameter groups

knapl relative 0.01 0.001 switch 2.0 parabolic

* parameter data (unless parameters can go to 0 or negative values, log-transformation is recommended)

kn log factor 0.096 0.002 20 knapl 1 0 1

be fixed factor 0.5 0.4 0.7 knapl 1 0 1

* observation groups (Observation groups and weights define Φ. Consult PEST User Manual Part II for special utilities PWTADJ1 and PWTADJ2 to automatically modify the observation weights depending on the goal, i.e., to either balance the visibility of various groups in Φ or to undertake linear uncertainty analysis)

pool

* observation data (each monitoring observation must have a unique name, followed by it value, weight, and group)

PCE_1 0.050492678 0 pool

PCE_2 0.081952128 0 pool

PCE_3 0.100726848 0 pool

PCE_4 0.113226048 0 pool

PCE_5 0.120672 0 pool

PCE_6 0.12561408 0 pool

PCE_7 0.128543616 0 pool

PCE_8 0.130473216 0 pool

PCE_9 0.131602752 0 pool

PCE_10 0.111628922363136 1 pool

PCE_11 0.110633474772173 1 pool

PCE_12 0.093759165549792 1 pool

PCE_13 0.103760527629946 1 pool

PCE_14 0.14113658065703 1 pool

PCE_15 0.122076527694682 1 pool

* model command line

runmodel (this is a windows batch file that runs the model, see below for an example)

* model input/output

pool2_230cm_1cmY_NPL.tpl pool2_230cm_1cmY.npl (template and corresponding input parameter file)

PCE.ins massdisch.dat (instruction and corresponding model output file)

Example of windows batch (.bat) file named runmodel. Notice various commands to delete all types of model output files to prevent PEST from mistakenly reading a previous set of output files before the next model run.

del *.out

del *.dat

del *.obs

S3Dbeta.exe pool2_230cm_1cmY.FIL

PEST is run from a command windows as:

cmd /k pest pool2_230cm_1cmY

where /k prevents the command windows from disappearing after executing PEST and pool2_230cm_1cmY is the name of the pest control file (.pst). The PEST executable and all other executables can be placed in a folder that is cited in the PATH environment variable of the computer to avoid keeping all executables in each folder containing the model and PEST files. Below is an example of a control file to calibrate the SEAM3D Borden model in Chapter 3.

pcf
* control data
restart estimation
54 4848 5 0 58
1 2 single point 1 0 0
20.0 -3.0 0.3 0.01 10 uptestmin=36 #JACUPDATE=999 (Consult PEST_HP manual for the uptestmin variable and consider model runtimes and computational resources; a high value of 36 was chosen to increase the possibility for greater Φ minimization after each iteration. Consult the manual for JACUPDATE, a randomized Jacobian matrix calculation after each iteration; which can be helpful to avoid entrapment in local minima when optimizing highly nonlinear models)
10.0 10.0 1.0e-3
0.1 3 jcowarnthresh=1.0e20 jcozerothresh=1.0e30 #[NOPTSWITCH=3 prevents early 3-point derivatives] [boundscale]
15 1.0e-4 4 4 1.0e-4 4 (Compare this stringent PEST termination criteria to the previous control file example, which has standard values. While the criteria in this file may prove useful for optimizing some highly nonlinear models, overfitting is not desirable either)
1 1 1 parsaveitn
* singular value decomposition
1

48 5.0e-7

1

* parameter groups

KNAPL relative 0.01 0.01 switch 2.0 parabolic (consult PEST manual Part I for these variables)

KMULT relative 0.01 0.01 switch 2.0 parabolic

MFRAC relative 0.01 0.001 switch 2.0 parabolic

ISOL relative 0.1 0.001 switch 2.0 parabolic

CNAP relative 0.01 0.001 switch 2.0 parabolic

* parameter data

kn4	log	factor	0.1024	0.01	7.5	knapl	1	0	1	
kn5.1	log	factor	0.0772	0.01	7.5	knapl	1	0	1	
kn5.2	log	factor	0.12073		0.01	7.5	knapl	1	0	1
kn5.3	log	factor	0.0906	0.01	7.5	knapl	1	0	1	
kn6.1	log	factor	2.0043	0.01	7.5	knapl	1	0	1	
kn6.2	log	factor	2.004	0.01	7.5	knapl	1	0	1	
kn6.3	log	factor	2.004	0.01	7.5	knapl	1	0	1	
kn7.1	log	factor	2.0571	0.01	7.5	knapl	1	0	1	
kn7.2	log	factor	0.4442	0.01	7.5	knapl	1	0	1	
kn7.3	log	factor	1.4526	0.01	7.5	knapl	1	0	1	
kn8.1	log	factor	0.6348	0.01	7.5	knapl	1	0	1	
kn8.2	log	factor	0.6243	0.01	7.5	knapl	1	0	1	
kn8.3	log	factor	0.6241	0.01	7.5	knapl	1	0	1	
kn9.1	log	factor	0.6292	0.01	7.5	knapl	1	0	1	
kn9.2	log	factor	0.6227	0.01	7.5	knapl	1	0	1	
kn9.3	log	factor	0.6357	0.01	7.5	knapl	1	0	1	
kn9.4	log	factor	0.1024	0.01	7.5	knapl	1	0	1	
kn10.1	log	factor	0.1024	0.01	7.5	knapl	1	0	1	
kn10.2	log	factor	0.1024	0.01	7.5	knapl	1	0	1	
kn10.3	log	factor	0.1024	0.01	7.5	knapl	1	0	1	

kn11.1 log factor 0.1024 0.01 7.5 knapl 1 0 1

kn11.2 log factor 0.1024 0.01 7.5 knapl 1 0 1

kn12 log factor 0.1024 0.01 7.5 knapl 1 0 1

kn multipliers (the sumbol # denotes a comment ignored by PEST)

kmult1 log factor 0.9552734 0.95 1.0 kmult 1.0 0.0 1

kmult2 log factor 0.8551065 0.8 0.95 kmult 1.0 0.0 1

mass fractions

mf1 fixed relative 9.6000000E-02 0.072 0.12 mfrac 1.0 0.0 1

mf2 fixed relative 0.3790000 0.28425 0.47375 mfrac 1.0 0.0 1

mf3 fixed relative 0.5250000 0.38635 0.643755 mfrac 1.0 0.0 1

solubilities

isol1 fixed relative 8700.000 6525.0 10875.0 isol 1.0 0.0 1

isol2 fixed relative 1400.000 1050.0 1750.0 isol 1.0 0.0 1

isol3 fixed relative 240.0000 180.0 300.0 isol 1.0 0.0 1

dnapl concentrations in soil

CN4 log factor 4.3375000E-03 1.55E-04 1.55E-02 CNAP 1.0 0.0 1

CN5.1 log factor 1.7600000E-04 1.55E-04 7.73E-02 CNAP 1.0 0.0 1

CN5.2 log factor 1.2400000E-02 1.55E-04 7.73E-02 CNAP 1.0 0.0 1

CN5.3 log factor 2.1800000E-03 1.55E-04 7.73E-02 CNAP 1.0 0.0 1

CN6.1 log factor 7.3260000E-02 1.55E-04 7.73E-02 CNAP 1.0 0.0 1

CN6.2 log factor 5.7610000E-02 1.55E-04 7.73E-02 CNAP 1.0 0.0 1

CN6.3 log factor 9.6100000E-03 1.55E-04 7.73E-02 CNAP 1.0 0.0 1

CN7.1 log factor 7.3260000E-02 1.55E-04 7.73E-02 CNAP 1.0 0.0 1

CN7.2 log factor 4.4848000E-02 1.55E-04 7.73E-02 CNAP 1.0 0.0 1

CN7.3 log factor 7.6900000E-03 1.55E-04 7.73E-02 CNAP 1.0 0.0 1

CN8.1 log factor 2.7400000E-02 1.55E-04 7.73E-02 CNAP 1.0 0.0 1

CN8.2 log factor 1.0734000E-02 1.55E-04 7.73E-02 CNAP 1.0 0.0 1

CN8.3 log factor 6.3400000E-03 1.55E-04 7.73E-02 CNAP 1.0 0.0 1

CN9.1 log factor 1.7600000E-04 3.09E-05 7.73E-02 CNAP 1.0 0.0 1

CN9.2 log factor 1.7460000E-02 1.55E-04 7.73E-02 CNAP 1.0 0.0 1

CN9.3 log factor 2.7710000E-02 1.55E-04 7.73E-02 CNAP 1.0 0.0 1

CN9.4 log factor 4.3375000E-03 1.55E-04 7.73E-02 CNAP 1.0 0.0 1

CN10.1 log factor 4.3375000E-03 1.55E-04 7.73E-02 CNAP 1.0 0.0 1

CN10.2 log factor 4.3375000E-03 1.55E-04 7.73E-02 CNAP 1.0 0.0 1

CN10.3 log factor 4.3375000E-03 1.55E-04 7.73E-02 CNAP 1.0 0.0 1

CN11.1 log factor 4.3375000E-03 1.55E-04 7.73E-02 CNAP 1.0 0.0 1

CN11.2 log factor 4.3375000E-03 1.55E-04 7.73E-02 CNAP 1.0 0.0 1

CN12 log factor 4.3375000E-03 1.55E-04 7.73E-02 CNAP 1.0 0.0 1

* observation groups (Not all groups are included here. In this example the monitoring data points are grouped by multilevel sampling port and mass discharge is grouped by DNAPL component. These groups constitute Φ, considering the observation weights in the following section. By running PEST once, the initial error of various observation groups in Φ are automatically calculated)

mls_704

mls_604

mls_504

mls_404

mls_304

mls_204

mls_705

mls_605

mls_505

mls_405

mls_305

mls_205

mls_706

mls_606

mls_506

mls_406

mls_306

mls_206

mls_707

mls_607

mls_507

mls_407

mls_307

mls_207

mls_708

mls_608

mls_508

tcm_md

tce_md

pce_md

* observation data (not all individual monitoring measurements are included in this example. Notice the unique data point name defined by NAPL component name, MLS port number, and collection day. A weight of 1 is not necessary, as higher values can be assigned to individual observations depending on the Φ definition. However, for flow and transport models a uniform weight should be assigned to individual observations within observation groups)

TCM704_11	0	0	mls_704
TCM604_11	0	0	mls_604
TCM504_11	0	1	mls_504
TCM404_11	0	0	mls_404
TCM304_11	0	0	mls_304
TCM204_11	0	0	mls_204
TCM705_11	0	0	mls_705
TCM605_11	0	1	mls_605

TCM505_11	0	1	mls_505
TCM405_11	0	1	mls_405
TCM305_11	0	0	mls_305
TCM205_11	0	0	mls_205
TCM706_11	0	0	mls_706
TCM606_11	0	1	mls_606
TCM506_11	0	1	mls_506
TCM406_11	0	1	mls_406
TCM306_11	0	0	mls_306
TCM206_11	0	0	mls_206
TCM707_11	0	0	mls_707
TCM607_11	0	1	mls_607
TCM507_11	0	1	mls_507
TCM407_11	0	1	mls_407
TCM307_11	0	0	mls_307
TCM207_11	0	0	mls_207
TCM708_11	0	0	mls_708
TCM608_11	0	1	mls_608
TCM508_11	0	1	mls_508
TCM408_11	0	1	mls_408
TCM208_11	0	0	mls_208
TCM709_11	0	0	mls_709
TCM609_11	0	1	mls_609
TCM509_11	0	1	mls_509
TCM409_11	0	1	mls_409
TCM309_11	0	1	mls_309

* model command line

Run (windows batch file; see example above)

* model input/output

Borden-NPL.tpl Borden-10cmZ.npl

Borden-MLS.ins Borden-10cmZ.out

Borden-MD.ins massdisch.dat

PEST_HP is more efficient when using 10 or more “agents” to undertake parallel model runs. The agents are run by the executable AGENT_HP and execute the model and report simulation results to a “manager” (PEST_HP). A folder named “manager” containing all PEST and model files can simply be copied in the same working directory into a number of folders relabeled as “agent1”, “agent2”, etc. (although this naming convention is not a requirement). The number of agent folders in a single machine can be equal to the number of cores. Several machines can be connected in a network to leverage as many cores as possible. Below is an example of a simple python script that can be doubled-clicked to automatically start the calibration process from a working directory that contains multiple agent folders and a manager folder. This uses the version PEST_HP_MKL executable (consults the PEST_HP user manual and the GMDSI “Calibration tutorial” tutorial for detailed information).

```
import os

wd = os.getcwd()

files = os.listdir(wd)

for file in files:
   if "Agent" in file:
      agent_path = os.path.join(wd,file)
      os.chdir(agent_path)
      os.system("start cmd /k agent_hp mls_all.pst /h 192.168.0.13:4004") #this is starting all
#agents using the IP address of the machine and an available port number (port 4004 is usually
#available)
```

```
master = files.index("Manager")
master_path = os.path.join(wd,files[master])
os.chdir(master_path)
os.system("start cmd /k pest_hp_mkl mls_all.pst /h :4004")
```

PEST Template files (.tpl)

Instruction files are necessary for PEST to alter the value of input parameters. Below is an example of an instruction file for the NAPL dissolution package of a single-cell SEAM3D model of Pool 2 in Chapter 4.

```
ptf #
      1       0       0       0       1       2
Solubility
237.000000
Molecular Weight
166.000000
99.0000000
Knapl Multipliers
1.000000
density
1630000
1000000
NAPL Parameters
1
      1       1       9 #  kn   #.002822651     1.00      1.0    # be #     1.000        0
```

Notice that at the beginning of the file the symbol # was used to denote the enclosure of a model parameter. In this example only the mass transfer coefficient k^N and the β parameter are being estimated. The number of digits that PEST uses to calculate finite-difference sensitivity matrices

includes the enclosing # symbols and any space and letter within. Consult the PEST User Manual Part I and the PEST_HP manual for more details on the importance and the limit of digits used for parameter values, including which symbols, such as #, are allowed. Note that for SEAM3D input files there are specific spacing requirements between parameter values on each line that must be respected. Other models are more flexible. Below is an example of a template file for the Borden model in Chapter 3.

ptf #

3 0 0 0 575 2

Solubility

#ISOL1 #

#ISOL2 #

#ISOL3 #

Molecular Weight

119.400000

131.400000

165.800000

99.0000000

Knapl Multipliers

1.00000000

#KMULT1#

#KMULT2#

Density (densities are not used in this model because β = 0)

1.

1.

1.

1.

NAPL Parameters

575 (This is the number of NAPL cells in the model. These are clipped for space in this example)

4 21 29 #KN4 # #CN4 # 0.0 0.0 0.00 #MF1# #MF2# #MF3# 0

4	21	30	#KN4	# #CN4	#	0.0	0.0	0.00	#MF1#	#MF2#	#MF3#	0
4	21	31	#KN4	# #CN4	#	0.0	0.0	0.00	#MF1#	#MF2#	#MF3#	0
4	21	32	#KN4	# #CN4	#	0.0	0.0	0.00	#MF1#	#MF2#	#MF3#	0
4	21	33	#KN4	# #CN4	#	0.0	0.0	0.00	#MF1#	#MF2#	#MF3#	0

PEST Instruction files (.ins)

Instruction files are necessary for PEST to retrieve simulated observations. There are multiple strategies to parse model output files using PEST conventions. Consult the PEST User Manual Part I for details. Below is an example of a simple instruction file to retrieve a few simulated mass discharge values produced by SEAM3D in a list format.

pif *

l3 !dum! !dum! !PCE_1! (The l3 instructs PEST to advance 3 lines including the very first line of the file)

l1 !dum! !dum! !PCE_2! (The !dum! variable instructs PEST to ignore any outputs separated by any number of spaces)

l1 !dum! !dum! !PCE_3! (The !PCE_3! variable instructs PEST where a specific observation is located, regardless of the number of digits)

l1 !dum! !dum! !PCE_4!

l1 !dum! !dum! !PCE_5!

l1 !dum! !dum! !PCE_6!

l1 !dum! !dum! !PCE_7!

l1 !dum! !dum! !PCE_8!

l1 !dum! !dum! !PCE_9!

l1 !dum! !dum! !PCE_10!

l1 !dum! !dum! !PCE_11!

l1 !dum! !dum! !PCE_12!

l1 !dum! !dum! !PCE_13!

l1 !dum! !dum! !PCE_14!

l1 !dum! !dum! !PCE_15!

Below is an example of an instruction file for the Borden model in Chapter 3 using keywords to parse the SEAM3D .OUT file. The line advance (la) command is also use for PEST to advance a given number of lines after encountering the keyword. Rather than using the !dum! variable, the specific number of spaces within a line in the output file enclosing the exact number of digits comprising the simulated output is used in this example. Because PEST needs to parse thousands of individual simulation outputs corresponding to specific ports and time steps, an example script to automate this process is also provided. Depending on the complexity of the modeling situation, consider defining observation cells in the SEAM3D basic transport package (BTN) to produce concentration outputs in a list format like the previous example.

pif * (the original file has 6065 lines and is truncated for space)

>FOR COMPONENT NO. 01<

CONCENTRATIONS IN LAYER 4 AT END OF TRANSPORT STEP 23

l69 (TCM704_11)85:94 (line advance l69: advance 69 lines after encountering the above keyword)

l25 (TCM604_11)85:94

l25 (TCM504_11)85:94

l25 (TCM404_11)85:94

l25 (TCM304_11)85:94

l25 (TCM204_11)85:94

CONCENTRATIONS IN LAYER 5 AT END OF TRANSPORT STEP 23

l69 (TCM705_11)85:94

l25 (TCM605_11)85:94

l25 (TCM505_11)85:94

l25 (TCM405_11)85:94

l25 (TCM305_11)85:94

l25 (TCM205_11)85:94

The example above requires creating unique observation names for almost 5000 observations. This can be achieved with Excel or more efficiently using a scripting programming language like Python to create unique names following some logical naming convention. The example also requires understanding how the SEAM3D .OUT file is structured to understand at which transport step, model layer, and line advance command a model output can be retrieved by PEST. The following picture shows a snippet of an excel file where such parsing variables have been prepared, followed by a Python script to automate writing of the instruction file example above.

	A	B	C	D	E	F	G	H	I	J	K
1	Observation	Transport Step	Layer	Line Advance							
2	TCM704_11	23	4	69							
3	TCM604_11	23	4	25							
4	TCM504_11	23	4	25							
5	TCM404_11	23	4	25							
6	TCM304_11	23	4	25							
7	TCM204_11	23	4	25							
8	TCM705_11	23	5	69							
9	TCM605_11	23	5	25							
10	TCM505_11	23	5	25							
11	TCM405_11	23	5	25							
12	TCM305_11	23	5	25							
13	TCM205_11	23	5	25							
14	TCM706_11	23	6	69							
15	TCM606_11	23	6	25							
16	TCM506_11	23	6	25							
17	TCM406_11	23	6	25							
18	TCM306_11	23	6	25							
19	TCM206_11	23	6	25							
20	TCM707_11	23	7	69							
21	TCM607_11	23	7	25							
22	TCM507_11	23	7	25							
23	TCM407_11	23	7	25							
24	TCM307_11	23	7	25							
25	TCM207_11	23	7	25							
26	TCM708_11	23	8	69							
27	TCM608_11	23	8	25							

mls_cells | obs_names | obs_order | obs_nan | obs_clean | time_steps | tpl_data | **tpl_build**

```
import pandas as pd

obs = pd.read_excel("instruction_structure_MLS_10cm-Z.xlsx", sheet_name="tpl_build", usecols="A:D")
```

```
# correct OUT: CONCENTRATIONS   IN LAYER 10 AT END OF TRANSPORT STEP  105 (>= 10 Layers)
# wrong OUT: CONCENTRATIONS   IN LAYER 10 AT END OF TRANSPORT STEP   105
# correct OUT: CONCENTRATIONS   IN LAYER  4 AT END OF TRANSPORT STEP   23 (<10 Layers)

with open("template.txt", "w") as tpl:
    for i in range(len(obs)):
        step = str(obs.values[i,1])
        layer = str(obs.values[i,2])
        advance = str(obs.values[i,3])
        if int(layer) < 10:
            if i == 0:
                if obs.values[i,0][0:3] == "TCM":
                    tpl.write("*>FOR COMPONENT NO. 01<*\n")
                elif obs.values[i,0][0:3] == "TCE":
                    tpl.write("*>FOR COMPONENT NO. 02<*\n")
                else:
                    tpl.write("*>FOR COMPONENT NO. 03<*\n")
                tpl.write("*CONCENTRATIONS    IN LAYER  " + layer + " AT END OF TRANSPORT STEP    " +
step + "*\n")
                tpl.write("l" + advance + " (" +  obs.values[i,0] + ")" + "85:94\n")
            elif int(step) < 100: # OUT file changes spacing starting trans. step 100
                if obs.values[i,0][0:3] == obs.values[i-1,0][0:3]: # skip if same component
                    if obs.values[i,2] == obs.values[i-1,2]: # skip if same layer
                        tpl.write("l" + advance + " (" +  obs.values[i,0] + ")" + "85:94\n") # only line advance
                    else:
                        tpl.write("*CONCENTRATIONS    IN LAYER  " + layer + " AT END OF TRANSPORT STEP
" + step + "*\n")
                        tpl.write("l" + advance + " (" +  obs.values[i,0] + ")" + "85:94\n")
```

```
            else:
                if obs.values[i,0][0:3] == "TCM":
                    tpl.write("*>FOR COMPONENT NO. 01<*\n")
                elif obs.values[i,0][0:3] == "TCE":
                    tpl.write("*>FOR COMPONENT NO. 02<*\n")
                else:
                    tpl.write("*>FOR COMPONENT NO. 03<*\n")
                tpl.write("*CONCENTRATIONS   IN LAYER  " + layer + " AT END OF TRANSPORT STEP   "
+ step + "*\n")
                tpl.write("l" + advance + " (" +  obs.values[i,0] + ")" + "85:94\n")
        else: # OUT file changes spacing starting trans. step 100
            if obs.values[i,0][0:3] == obs.values[i-1,0][0:3]: # skip if same component
                if obs.values[i,2] == obs.values[i-1,2]: # skip if same layer
                    tpl.write("l" + advance + " (" +  obs.values[i,0] + ")" + "85:94\n") # only line advance
                else:
                    tpl.write("*CONCENTRATIONS   IN LAYER  " + layer + " AT END OF TRANSPORT STEP
" + step + "*\n")
                    tpl.write("l" + advance + " (" +  obs.values[i,0] + ")" + "85:94\n")
            else:
                if obs.values[i,0][0:3] == "TCM":
                    tpl.write("*>FOR COMPONENT NO. 01<*\n")
                elif obs.values[i,0][0:3] == "TCE":
                    tpl.write("*>FOR COMPONENT NO. 02<*\n")
                else:
                    tpl.write("*>FOR COMPONENT NO. 03<*\n")
                tpl.write("*CONCENTRATIONS   IN LAYER  " + layer + " AT END OF TRANSPORT STEP  "
+ step + "*\n")
                tpl.write("l" + advance + " (" +  obs.values[i,0] + ")" + "85:94\n")
        else:
```

```
        if i == 0:
            if obs.values[i,0][0:3] == "TCM":
                tpl.write("*>FOR COMPONENT NO. 01<*\n")
            elif obs.values[i,0][0:3] == "TCE":
                tpl.write("*>FOR COMPONENT NO. 02<*\n")
            else:
                tpl.write("*>FOR COMPONENT NO. 03<*\n")
            tpl.write("*CONCENTRATIONS    IN LAYER " + layer + " AT END OF TRANSPORT STEP    " +
step + "*\n")
            tpl.write("l" + advance + " (" +  obs.values[i,0] + ")" + "85:94\n")
        elif int(step) < 100: # OUT file changes spacing startinng trans. step 100
            if obs.values[i,0][0:3] == obs.values[i-1,0][0:3]: # skip if same component
                if obs.values[i,2] == obs.values[i-1,2]: # skip if same layer
                    tpl.write("l" + advance + " (" +  obs.values[i,0] + ")" + "85:94\n") # only line advance
                else:
                    tpl.write("*CONCENTRATIONS    IN LAYER " + layer + " AT END OF TRANSPORT STEP
" + step + "*\n")
                    tpl.write("l" + advance + " (" +  obs.values[i,0] + ")" + "85:94\n")
            else:
                if obs.values[i,0][0:3] == "TCM":
                    tpl.write("*>FOR COMPONENT NO. 01<*\n")
                elif obs.values[i,0][0:3] == "TCE":
                    tpl.write("*>FOR COMPONENT NO. 02<*\n")
                else:
                    tpl.write("*>FOR COMPONENT NO. 03<*\n")
                tpl.write("*CONCENTRATIONS    IN LAYER " + layer + " AT END OF TRANSPORT STEP    "
+ step + "*\n")
                tpl.write("l" + advance + " (" +  obs.values[i,0] + ")" + "85:94\n")
        else: # OUT file changes spacing startinng trans. step 100
```

```
        if obs.values[i,0][0:3] == obs.values[i-1,0][0:3]: # skip if same component
            if obs.values[i,2] == obs.values[i-1,2]: # skip if same layer
                tpl.write("l" + advance + " (" +  obs.values[i,0] + ")" + "85:94\n") # only line advance
            else:
                tpl.write("*CONCENTRATIONS   IN LAYER " + layer + " AT END OF TRANSPORT STEP  "
+ step + "*\n")
                tpl.write("l" + advance + " (" +  obs.values[i,0] + ")" + "85:94\n")
        else:
            if obs.values[i,0][0:3] == "TCM":
                tpl.write("*>FOR COMPONENT NO. 01<*\n")
            elif obs.values[i,0][0:3] == "TCE":
                tpl.write("*>FOR COMPONENT NO. 02<*\n")
            else:
                tpl.write("*>FOR COMPONENT NO. 03<*\n")
            tpl.write("*CONCENTRATIONS   IN LAYER " + layer + " AT END OF TRANSPORT STEP  " +
step + "*\n")
            tpl.write("l" + advance + " (" +  obs.values[i,0] + ")" + "85:94\n")
```

Retrieving PEST results

After running PEST or PEST_HP inspect the REC (.rec) file to retrieve parameter optimization results and evaluate parameter upgrades after each iteration. PEST_HP also produces an OFR (.ofr) file which can be monitored during the calibration process to see how Φ is minimized, including the error contribution by individual observation groups after every iteration. Also, consider inspecting the SEN (.sen) file to evaluate composite parameter sensitivities to observation groups after each iteration.

References

Doherty, J. (2015). *Calibration and Uncertainty Analysis for Complex Environmental Models.* Brisbane, Australia: Watermark Numerical Computing.

Watermark Numerical Computing. (2018). *Model-Independent Parameter Estimation. User Manual Part II: PEST Utility Suport Software.* Retrieved from https://pesthomepage.org/documentation

Watermark Numerical Computing. (2018). *PEST. Model-Independent Parameter Estimation. User Manual Part I: PEST, SENSAN, and Global Optimisers.* Retrieved from pesthomepage: https://pesthomepage.org/documentation

Appendix D: History Matching and Nonlinear Uncertainty Analysis

History matching and nonlinear uncertainty analyses in this work were facilitated by the PESTPP-iES software. This iterative ensemble smoother (iES) is part of the PEST++ software suite, which can be downloaded at the USGS website, including updated user manuals and associated documentation. In addition, the GMDSI website (https://gmdsi.org/) provides webinars, worked examples, step-by-step tutorials, and roadmaps for understanding practical concepts and implementation details. As with PEST and PEST_HP, iES requires template and instruction files, and a control file where additional functionality can be implemented as shown in the example below.

Example: Volume-averaged (VA) model of heterogeneous source architecture in Chapter 2, including 4 distinct DNAPL accumulations.

This example demonstrates the usage of iES to approximate the probability density (PDF) of time of remediation (TOR) before (prior) and after (posterior) history matching of effluent concentration data. An arbitrary value of 6 mg/L was added as the standard deviation of measurement noise for iES to produce observation realizations, each of which is paired with a parameter realization before and during the history-matching process. Before model optimization, iES undertakes a prior Monte Carlo analysis to identify prior-data conflicts (PDCs) that may bias optimization results and model predictions unless the model is modified or observations are discarded (White, 2018; White et al. 2021). In the examples below, ignore and do not include the text in parenthesis. Except where indicated, the definition of all variables in the control, instruction, and template files is found in the PEST User Manual Part I with some definitions also provided in Appendix C.

Control file (.pst)

```
pcf
* control data
restart  estimation
29 65 8 0 2
```

1 2 single point 1 0 0

20.0-3.0 0.3 0.01 10

10.0 10.0 1.0e-3

0.1 3

12 1.0e-4 4 4 1.0e-4 4 (maximum of 12 optimization iterations with a tight termination criteria that may lead to overfitting. Consider the example below of tracking the evolution of the objective function Φ to avoid using overfit results for posterior uncertainty)

1 1 1 parsaveitn

* singular value decomposition

1

24 5.0e-7 (number of parameters)

1

* parameter groups

VREF relative 0.01 0.01 switch 2.0 parabolic

POR relative 0.01 0.01 switch 2.0 parabolic

FLOW relative 0.01 0.01 switch 2.0 parabolic

MASS relative 0.01 0.01 switch 2.0 parabolic

VA relative 0.01 0.01 switch 2.0 parabolic

DISP relative 0.01 0.0001 switch 2.0 parabolic

GAMMA relative 0.01 0.01 switch 2.0 parabolic

ZPOOL relative 0.001 0.0001 switch 2.0 parabolic

* parameter data (numbers in purple correspond to starting values followed by and upper/lower uncertainty bounds)

XSOURCE	fixed	relative	0.400000000000000	0.0100	1.0000	VREF	1	0	1
YSOURCE	fixed	relative	0.025400000000000	0.0050	0.0500	VREF	1	0	1
ZSOURCE	fixed	relative	0.190000000000000	0.0500	0.5000	VREF	1	0	1
PORM	fixed	relative	0.400000000000000	0.1000	0.8000	POR	1	0	1
DARCY	fixed	relative	0.993617903025280	0.1000	2.0000	FLOW	1	0	1
MASS1A	log	factor	5.256000000000000	2.000	20.000	MASS	1	0	1
XA01A	log	factor	0.070000000000000	0.0600	0.2000	VA	1	0	1
YA01A	log	factor	0.025400000000000	0.0200	0.0254	ZPOOL	1	0	1
ZA01A	log	factor	0.075000000000000	0.0500	0.1000	VA	1	0	1
DSP1A	log	factor	0.001000000000000	0.0005	0.002	DISP	1	0	1
GAM01A	log	factor	0.550000000000000	0.4000	0.7500	GAMMA	1	0	1
MASS1B	log	factor	7.738000000000000	2.000	8.000	MASS	1	0	1
XA01B	log	factor	0.030000000000000	0.0250	0.2000	VA	1	0	1

YA01B	log	factor	0.025400000000000	0.0210	0.0254	ZPOOL	1	0	1
ZA01B	log	factor	0.055000000000000	0.0450	0.1000	VA	1	0	1
DSP1B	log	factor	0.001000000000000	0.0005	0.002	DISP	1	0	1
GAM01B	log	factor	0.550000000000000	0.4000	0.7500	GAMMA	1	0	1
MASS2	log	factor	1.752000000000000	1.0000	4.000	MASS	1	0	1
XA02	log	factor	0.046000000000000	0.0300	0.2000	VA	1	0	1
YA02	log	factor	0.025400000000000	0.0200	0.0254	ZPOOL	1	0	1
ZA02	log	factor	0.035000000000000	0.0200	0.1000	ZPOOL	1	0	1
DSP2	log	factor	0.001000000000000	0.0005	0.002	DISP	1	0	1
GAM02	log	factor	0.550000000000000	0.4000	0.7500	GAMMA	1	0	1
MASS3	log	factor	5.694000000000000	2.000	6.000	MASS	1	0	1
XA03	log	factor	0.066000000000000	0.0640	0.2000	VA	1	0	1
YA03	log	factor	0.025400000000000	0.0240	0.0254	ZPOOL	1	0	1
ZA03	log	factor	0.013800000000000	0.0115	0.1000	ZPOOL	1	0	1
DSP3	none	relative	0.000000000000000	0.0000	0.002	DISP	1	0	1
GAM03	log	factor	0.550000000000000	0.4000	0.7500	GAMMA	1	0	1

* observation groups

tce

tor

* observation data external

observations.csv (iES allows to keep observations in an external .csv file. See below for an example)

* model command line

runSCARPE.bat

* model input/output

het4.tpl DissolveCalcSA.in (name of template and input file)

het4.ins DissolveCalc.out

het4_TOR.ins DissolveTOR.out

++ies_num_reals(240) (arbitrarily defined 240 parameter realization per iteration)

++ies_autoadaloc(true) (default, see PEST++ User Manual for details)

++ies_no_noise(false) (this example is using noise added to data. See details below)

++ies_drop_conflicts(false) (PDCs were not ignored in this case)

++ies_subset_size(24) (consult PEST++ manual. This is controlling the number of realizations for lambda testing during optimization iterations).

External observation file compatible with iES (named observations.csv)

OBSNME	OBSVAL	WEIGHT	OBGNME	STANDARD_DEVIATION
tce_1	0.525931	1	tce	6
tce_2	1.984361	1	tce	6
tce_3	256.5238	1	tce	6
tce_4	387.5502	1	tce	6
tce_5	363.7782	1	tce	6
tce_6	568.5467	1	tce	6
tce_7	496.7859	1	tce	6
tce_8	469.9312	1	tce	6
tce_9	390.3893	1	tce	6
tce_10	300.4889	1	tce	6
tce_11	417.9998	1	tce	6
tce_12	428.8807	1	tce	6
tce_13	388.8681	1	tce	6
tce_14	302.7279	1	tce	6
tce_15	343.9333	1	tce	6
tce_16	329.5689	1	tce	6
tce_17	257.6831	1	tce	6
tce_18	257.473	1	tce	6
tce_19	207.1933	1	tce	6
tce_20	195.3268	1	tce	6
tce_21	187.0205	1	tce	6
tce_22	208.7525	1	tce	6
tce_23	191.1321	1	tce	6
tce_24	189.9795	1	tce	6
tce_25	196.8372	1	tce	6
tce_26	119.1172	1	tce	6
tce_27	133.8866	1	tce	6
tce_28	160.2589	1	tce	6
tce_29	153.0789	1	tce	6
tce_30	139.6619	1	tce	6
tce_31	134.8258	1	tce	6
tce_32	130.8867	1	tce	6
tce_33	118.1036	1	tce	6
tce_34	108.4543	1	tce	6

tce_35	104.1202	1	tce	6
tce_36	91.18652	1	tce	6
tce_37	85.6095	1	tce	6
tce_38	72.19797	1	tce	6
tce_39	81.15626	1	tce	6
tce_40	64.81474	1	tce	6
tce_41	66.49049	1	tce	6
tce_42	74.92216	1	tce	6
tce_43	78.71621	1	tce	6
tce_44	83.57211	1	tce	6
tce_45	95.62099	1	tce	6
tce_46	94.74795	1	tce	6
tce_47	90.8543	1	tce	6
tce_48	95.0218	1	tce	6
tce_49	107.5516	1	tce	6
tce_50	95.78487	1	tce	6
tce_51	98.20531	1	tce	6
tce_52	88.30142	1	tce	6
tce_53	108.0154	1	tce	6
tce_54	89.31145	1	tce	6
tce_55	78.91129	1	tce	6
tce_56	84.52306	1	tce	6
tce_57	59.04638	1	tce	6
tce_58	33.31578	1	tce	6
tce_59	48.55496	1	tce	6
tce_60	20.8062	1	tce	6
tce_61	10.1722	1	tce	6
tce_62	8.685791	1	tce	6
tce_63	2.081367	1	tce	6
tce_64	0.937228	1	tce	6
tce_tor	28.57839	0	tor	2.4

Template file (het4.tpl)

```
ptf #

4
```

1

1

0

0

0

0

2

#XSOURCE #

#YSOURCE #

#ZSOURCE #

1

#PORM#

0.33

0

#DARCY #

0.15

3

0

160

0.01

0.00000001

0.000000001

1

5

0

0

0

0

1100

1460000

131

0.00006048

1

1

0

0

0.005

0

0

0

1

#MASS1A #

#XA01A #

#YA01A #

#ZA01A #

#DSP1A #

1

1

#GAM01A#

-1

0

#MASS1B #

#XA01B #

#YA01B #

#ZA01B #

#DSP1B #

1

1

#GAM01B#

-1

0

#MASS2 #

#XA02 #

#YA02 #

#ZA02 #

#DSP2 #

1

1

#GAM02#

0.55

1

#MASS3 #

#XA03 #

#YA03 #

#ZA03 #

#DSP3 #

1

3.46882217090069

#GAM03#

0.55

1

Instruction file (het4.ins)

pif *

l6 (tce_1)16:28 (including the very first line, l6 instructs PEST to advance 6 lines to retrieve the simulated value corresponding to tce_1 observation at the correct time step, with the observation name enclosed in parenthesis and the exact number of spaces at line 6 encompassing the target model output)

l1 (tce_2)16:28

l1 (tce_3)16:28

l2 (tce_4)16:28

l3 (tce_5)16:28

l5 (tce_6)16:28

l8 (tce_7)16:28

l3 (tce_8)16:28

l5 (tce_9)16:28

l44 (tce_10)16:28

l25 (tce_11)16:28

l51 (tce_12)16:28

l38 (tce_13)16:28

l57 (tce_14)16:28

l33 (tce_15)16:28

l50 (tce_16)16:28

l34 (tce_17)16:28

l61 (tce_18)16:28

l46 (tce_19)16:28

l63 (tce_20)16:28

l24 (tce_21)16:28

l66 (tce_22)16:28

l47 (tce_23)16:28

l49 (tce_24)16:28

l37 (tce_25)16:28

l56 (tce_26)16:28

l38 (tce_27)16:28

l70 (tce_28)16:28

l25 (tce_29)16:28

l77 (tce_30)16:28

l43 (tce_31)16:28

l54 (tce_32)16:28

l34 (tce_33)16:28

l66 (tce_34)16:28

l38 (tce_35)16:28

l47 (tce_36)16:28

l35 (tce_37)16:28

l57 (tce_38)16:28

l38 (tce_39)16:28

l72 (tce_40)16:28

l32 (tce_41)16:28

l68 (tce_42)16:28

l34 (tce_43)16:28

l24 (tce_44)16:28

l52 (tce_45)16:28

l131 (tce_46)16:28

l63 (tce_47)16:28

l44 (tce_48)16:28

l45 (tce_49)16:28

l39 (tce_50)16:28

l72 (tce_51)16:28

l21 (tce_52)16:28

```
l52 (tce_53)16:28
l50 (tce_54)16:28
l40 (tce_55)16:28
l26 (tce_56)16:28
l73 (tce_57)16:28
l112 (tce_58)16:28
l41 (tce_59)16:28
l59 (tce_60)16:28
l98 (tce_61)16:28
l32 (tce_62)16:28
l69 (tce_63)16:28
```

Instruction file (het4_TOR.ins)

```
pif *

l1 !tce_tor!
```

Windows batch file (runSCARPE.bat): model execution command for PEST

```
del *.out
DissolutionCalculatorV04a.exe
```

The following Python script reads the het4.0.obs.csv and het4.10.obs.cvs files, including TOR realizations generated by iES at iteration 0 (prior to history matching) and iteration 10 to produce approximate prior and posterior TOR PDFs. These file names are automatically created by iES using the name of the control file. The file used for the posterior PDF can be any file after iteration 1, depending on the desired level of data fit to quantify uncertainty.

```
prior = pd.read_csv('het4.0.obs.csv')
prior.drop(prior[prior.tce_tor ==-1].index, inplace=True)
prior = prior['tce_tor']

posterior = pd.read_csv('het4.10.obs.csv')
```

```
posterior.drop(posterior[posterior.tce_tor ==-1].index, inplace=True)
posterior = posterior['tce_tor']

sns.set_style(style='ticks')
colors = ['purple','blue']
sns.set_palette(sns.color_palette(colors))

fig, ax = plt.subplots()
for i in [prior, posterior]:
    ax = sns.kdeplot(i, shade=True, legend=False)

sns.distplot(ax=ax).set_xlabel('TOR (days)', fontsize=14, weight='bold')
sns.distplot(ax=ax).set_ylabel('Probability Density', fontsize=14, weight='bold')
ax.legend(['Prior TOR Uncertainty','Posterior TOR Uncertainty'], fontsize=12, loc='best')
ax.set_yticks(np.arange(0,0.5,0.1))
ax.tick_params(axis='both', labelsize=12)

plt.tight_layout()
```

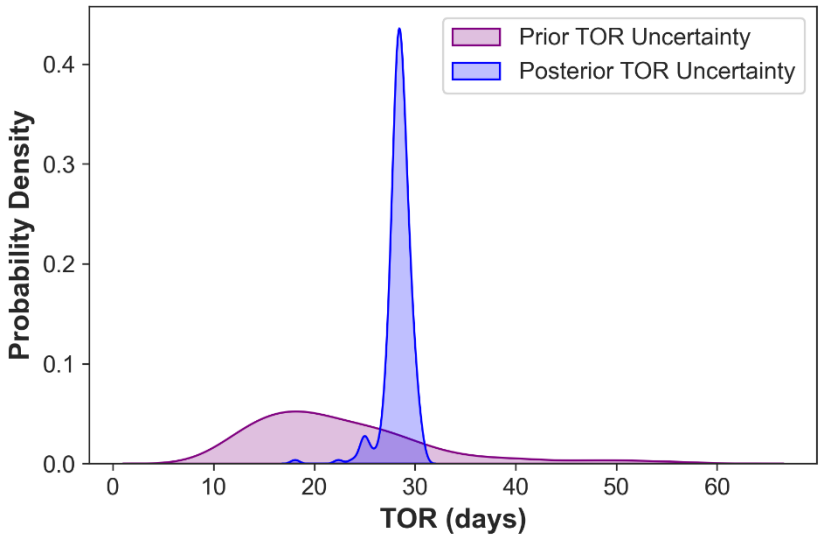

Figure D-1. Prior and Posterior TOR PDFs.

The following python script can be used to plot realizations of simulated discharge concentrations. The file data.xlsx contains two columns with time (days) and measured discharge concentrations.

```
import matplotlib.pyplot as plt
import pandas as pd
import numpy as np

results = pd.read_csv('het4.6.obs.csv')
data = pd.read_excel('data.xlsx')
time = data.iloc[:,0]
data = data.iloc[:,1]

# results.drop(results[results.tce_tor ==-1].index, inplace=True) # Removes all failed runs (TOR =-1)
results = results.iloc[: , :-1].transpose()
tce = results.iloc[1:]



fig, ax = plt.subplots(figsize = (12,8))
# fig, ax = plt.subplots()

plt.plot(time, tce[tce.columns], color='black', linewidth=0.2)

ax.plot(time, data, marker='D', markersize=6, color='red', linestyle='none',
      markerfacecolor='none', label='data')
ax.plot(time, tce[tce.columns[0]], color='black', linewidth=0.2,
      label='ensemble realizations')
ax.legend(fontsize=20)
ax.yaxis.set_tick_params(length=8)
ax.xaxis.set_tick_params(length=8)

# plt.xticks(phi[phi.columns[0]])
plt.tick_params(axis='both', which='major', labelsize=20)
plt.xlabel('Time (days)',fontsize=20, weight='bold')
plt.ylabel('TCE Effluent Concentrations (mg/L)',fontsize=20, weight='bold')
```

```
# plt.title('Prior TOR Uncertainty')
# plt.tight_layout()
plt.savefig('posterior-6.png', dpi=300)
```

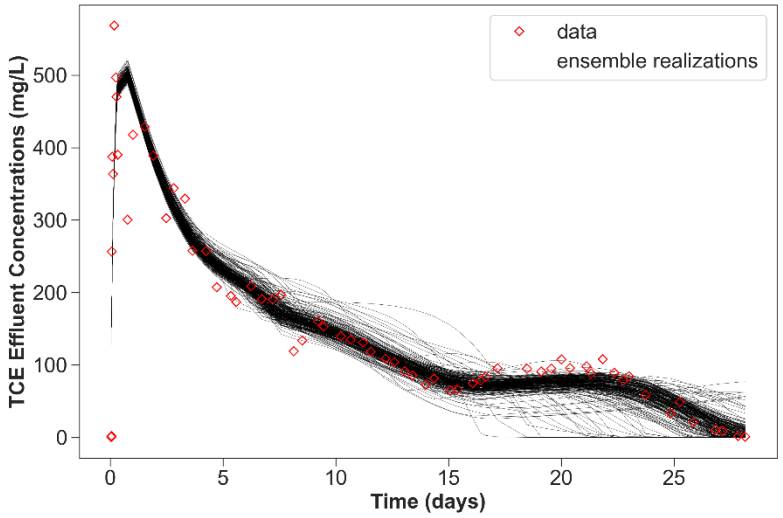

Figure D-2. Posterior realizations of simulated discharge concentrations obtained after 6 iES iterations.

Finally, consider reviewing the evolution of Φ to select observation ensembles representative of the posterior model uncertainty depending on the level of data fit (or misfit) that can be tolerated. The following script reads a file named het4.phi.actual.csv generated by iES including Φ iterations without noise added. The same script can be used to plot the het4.phi.meas.csv which includes observation noise.

```
import matplotlib.pyplot as plt
import pandas as pd
import numpy as np

phi = pd.read_csv('het4.phi.actual.csv')

# phi = phi[:6] #Keep only iterations 0:5
```

```
for col in phi.columns[6:]:
    phi[col] = np.log10(phi[col])

fig, ax = plt.subplots()

plt.plot(phi[phi.columns[0]], phi[phi.columns[6:]], color='black', linewidth=0.1)

ax.plot(phi[phi.columns[0]], phi[phi.columns[-1]], color='red', linewidth=0.8,
        label='base realization')
ax.plot(phi[phi.columns[0]], phi[phi.columns[6]], color='black', linewidth=0.1,
       label='ensemble realizations')
ax.legend()

plt.xticks(phi[phi.columns[0]])
plt.xlabel('iterations')
plt.ylabel('log '+r"$\phi$")
plt.title('Phi- actual (Obs in Control File)')
```

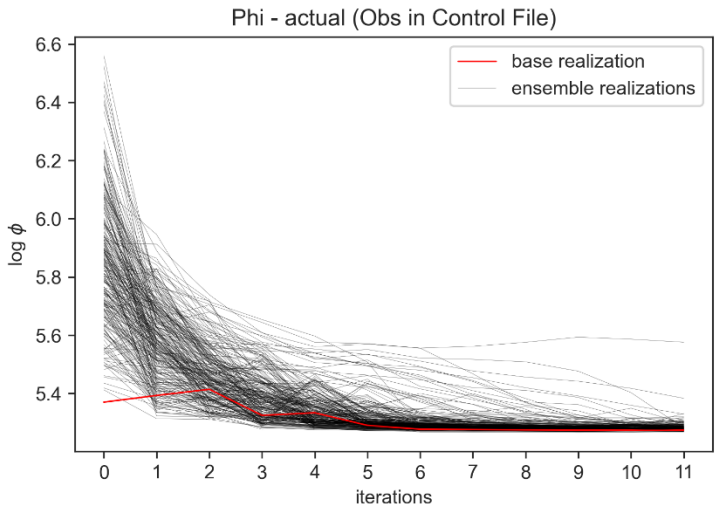

Figure D-3. Plot of log-transformed Φ realizations during history matching with iES. Iteration 6 was selected to produce Figure 2. Iteration 0 corresponds to the prior Monte Carlo analysis.

References

White, J. T. (2018). A model-independent iterative ensemble smoother for efficient history-matching and uncertainty quantification in very high dimensions. *Environmental Modelling & Software, 109,* 191-201. https://doi.org/doi.org/10.1016/j.envsoft.2018.06.009

White, J. T., Hemmings, B., Fienen, M. N., & Knowling, M. J. (2021). Towards improved environmental modeling outcomes: Enabling low-cost access to high-dimensional, geostatistical-based decision-support analyses. *Environmental Modelling and Software, 139*, 105022. https://doi.org/10.1016/j.envsoft.2021.105022

White, J., Hunt, R., Fienen, M., & Doherty, J. (2020). *Approaches to Highly Parameterized Inversion: PEST++ Version 5, a Software Suite for Parameter Estimation, Uncertainty Analysis, Management Optimization and Sensitivity Analysis.* Reston, VA: U.S. Geological Survey. https://doi.org/10.3133/tm7C26